UNIVERSITY OF SOUTHAMPTON

FACULTY OF ENGINEERING AND THE ENVIRONMENT

Astronautics Research Group

Correlation Aspects of Spacecraft and Multi-Physics Finite Element Models

by

Sairajan Kolasseri Kuttappan

Thesis for the degree of Doctor of Philosophy

July 2013

UNIVERSITY OF SOUTHAMPTON

ABSTRACT

FACULTY OF ENGINEERING AND THE ENVIRONMENT

Doctor of Philosophy

CORRELATION ASPECTS OF SPACECRAFT AND MULTI-PHYSICS FINITE ELEMENT MODELS

by Sairajan Kolasseri Kuttappan

Finite element analysis is widely used to predict the behaviour of complex structures such as spacecraft and/or multi-physics systems. The 'quality' of the Finite Element Model (FEM), defined as the capability of the model to simulate the behaviour of the real physical hardware, is assessed by comparing the analytical results with experimental data. In this thesis, Modal Assurance Criterion (MAC) and Normalised Cross Orthogonality (NCO) check are examined for their usefulness in the correlation of real spacecraft structures and then applied to multi-physics systems using the results of the 'true' FEM as the experimental or nominal data and those obtained from the erroneous FEM as analytical data. The NCO check requires a compatible mass matrix, which can be obtained from the global or complete FEM using the System Equivalent Reduction Expansion Process (SEREP). Here, a probabilistic approach is used to assess the robustness of a SEREP based test analysis model to inaccuracies by inputting a range of known errors into the modes of three spacecraft models. The effect of parameters used in the SEREP and the degree of inaccuracy tolerated in the modes before failing the NCO check were examined. The relationship between the capability of the FEM to predict some relevant responses and the quality of the model correlation determined using MAC and NCO check was also investigated. A method to optimise the choice of accelerometer locations to increase the robustness of the NCO check is proposed. In addition, the effectiveness of MAC and NCO criteria in the prediction of structural response under the base excitation was performed using three spacecraft models. It is observed that these criteria are not entirely satisfactory, particularly when the FEM is used to predict the forced response characteristics. A qualitative indicator termed the Base Force Assurance Criterion (BFAC) is then defined by comparing the nominal dynamic force at the base and the FEM predicted base force to predict the possible error in the peak acceleration and the dynamic displacement. The results show that the BFAC can better correlate the response than the conventional MAC or NCO check.

The correlation of the FEM of two types of multi-physics systems, namely viscoelastic damped systems and a piezoelectric system were also carried out. The usefulness of MAC and NCO check in the prediction of loss factor of the viscoelastic systems is assessed and it is noted that these correlation methods fail to represent the dynamic characteristics under base excitation and once again, the BFAC is found to be a better tool to correlate the viscoelastic systems. The effect of temperature as an uncertainty on the MAC and NCO check is also studied using the viscoelastic systems. The usefulness of the MAC for the correlation of the FEM of a shunted piezoelectric system is also analysed under the harmonic excitation. It is observed that the MAC has limited use in the correlation of such systems. Finally, a new correlation method based on electric current is defined and it is shown that this criterion correlates the dynamic characteristics of the piezoelectric system better than the MAC.

Contents

List of Tables

List of Figures

DECLARATION OF AUTHORSHIP

I, Sairajan Kolasseri Kuttappan

declare that the thesis entitled

Correlation Aspects of Spacecraft and Multi-Physics Finite Element Models

and the work presented in the thesis are both my own, and have been generated by me as the result of my own original research. I confirm that:

- this work was done wholly or mainly while in candidature for a research degree at this University;
- where any part of this thesis has previously been submitted for a degree or any other qualification at this University or any other institution, this has been clearly stated;
- where I have consulted the published work of others, this is always clearly attributed;
- where I have quoted from the work of others, the source is always given. With the exception of such quotations, this thesis is entirely my own work;
- I have acknowledged all main sources of help;
- where the thesis is based on work done by myself jointly with others, I have made clear exactly what was done by others and what I have contributed myself;
- parts of this work have been published as:

Journal Papers

- Sairajan, K. K., and Aglietti, G. S., "Robustness of System Equivalent Reduction Expansion Process on Spacecraft Structure

Model Validation", *AIAA Journal,* Vol. 50, No. 11, 2012, pp. 2376-2388.

- Sairajan, K. K., and Aglietti, G. S., "Study of the Correlation Criteria for Base Excitation of Spacecraft Structures", *Journal of Spacecraft and Rockets*.
  URL: http://arc.aiaa.org/doi/pdf/10.2514/1.A32457,
  doi: 10.2514/1.A32457

Conference Papers

- Sairajan, K. K., and Aglietti, G. S., "Validity of Model Correlation Methods in FEM Validation for Forced Vibration Analysis", *Proceedings of 12th European Conference on Spacecraft Structures, Materials and Environmental Testing*, ESA Communications, ESA-SP-691, Noordwijk, The Netherlands, July 2012.

- Sairajan, K. K., and Aglietti, G. S., "Standard FEM Validation Checks and Quality of Response Prediction", *63rd International Astronautical Congress*, IAC-12-C2.1.6, Naples, Italy, Oct. 2012.

- Sairajan, K. K., Aglietti, G. S., and Walker, S. J. I., "Correlation of Finite Element Model of a Piezoelectric System", Proceedings of *International Conference on Advances in Engineering and Technology*, Vol. 3, Kanthimathi Publications, Chennai, India, Apr. 2013, pp. 22-25.

Siged: .....

Date: 31/07/2013

Acknowledgements

I would like to express my sincere gratitude to my supervisor Prof. Guglielmo S Aglietti and my co-supervisor Dr. Scott J I Walker for their valuable guidance and continual encouragement though out this work. Their suggestions and critical comments helped me to refine the work reported here.

I am also grateful to G. Richardson, Surrey Satellite Technology Ltd, U.K., and A. Kiley, Astrium Ltd, U.K. for providing the spacecraft finite element models for this study. The author greatly acknowledges the Commonwealth Scholarship Commission, UK for their funding and the Ministry of Human Resource Development, New Delhi for my nomination to the Commonwealth Scholarship Commission. I am also thankful to my employer, the Indian Space Research Organisation for granting me the study leave, especially Dr. P.S. Nair for his support for me to take up this programme, and Prof. D. Chakraborty, Mr. K.M. Mani, and Mr. K.R. Rajappan for their help in securing the scholarship.

I would like to thank Dr. Steffano Redi for his help in Matlab; Mr. K.V. Muralidhar, Mr. Thomas K. Joseph, and Mrs. Lopamudra Mishra for their help in Nastran; Dr. T.K. Alex, Mr. R.K. Srinivasan, Dr. G. Raju, Dr. K. Renji, Mr. D. Poomani, Mr. K. Sreeshan and other colleagues and friends at ISRO for their various support to finish this work.

Special thanks to my family, colleagues at University of Southampton, and friends. Their continual support helped me significantly to finish this work. I dedicate this thesis to my parents.

Above all, the blessings of omnipresent GOD are greatly acknowledged.

Nomenclature

A	=	amplitude of modal displacement
a_{Nom}	=	absolute value of the peak nominal acceleration, g
a_{FEM}	=	absolute value of the peak FEM acceleration, g
C	=	capacitor
$\boldsymbol{C}$	=	elastic stiffness tensor
$\boldsymbol{CB}$	=	Craig – Bampton transformation matrix
$\boldsymbol{D}$	=	dielectric tensor
E	=	Young's modulus, N/m^2
$\boldsymbol{F}$	=	absolute values of the base forces/moments, N or Nm
$\boldsymbol{f}_B$	=	body force
$\boldsymbol{f}_L$	=	internal load, N or Nm
$\boldsymbol{f}_p$	=	point force
$\boldsymbol{f}_R$	=	boundary load, N or Nm
$\boldsymbol{f}_S$	=	surface force
g	=	acceleration due to gravity, m/s^2
$\boldsymbol{I}$	=	identity matrix
i	=	$\sqrt{-1}$
H	=	frequency response
$\boldsymbol{J}$	=	unit square matrix
$\boldsymbol{K}$	=	stiffness matrix
$\boldsymbol{K}_{BB}$	=	stiffness matrix reduced to the boundary
$\boldsymbol{K}_{mm}$	=	generalised stiffness matrix
$\boldsymbol{K}_{xv}$	=	piezoelectric stiffness matrix
$\boldsymbol{K}_{vv}$	=	dielectric stiffness matrix
L	=	inductor
$\boldsymbol{M}$	=	mass matrix
$\boldsymbol{M}_{BB}$	=	mass matrix reduced to the boundary
$\boldsymbol{M}_{mB}$	=	reduced couple mass matrix
$\boldsymbol{M}_{mm}$	=	generalised mass matrix
$\boldsymbol{M}_{LR}$	=	partitioned mass matrix – coupled terms (internal)
$\boldsymbol{M}_{RL}$	=	partitioned mass matrix – coupled terms (boundary)
m_i	=	generalised mass of mode *i*
$\boldsymbol{M}_{SEREP}$	=	SEREP reduced mass matrix

$\otimes$	=	element by element matrix multiplication operator
P	=	percentage of inaccuracy
$\boldsymbol{p}_{iR}$	=	modal participation factor, kg or kgm^2
$\boldsymbol{q}$	=	modal displacement
$\boldsymbol{q}_T$	=	total applied electric charge
$\boldsymbol{q}_B$	=	body charge
$\boldsymbol{q}_m$	=	modal coordinates used in the Craig – Bampton reduction
$\boldsymbol{q}_p$	=	point charge
$\boldsymbol{q}_S$	=	surface charge
$\dot{\boldsymbol{q}}$	=	modal velocity
$\ddot{\boldsymbol{q}}$	=	modal acceleration
$\boldsymbol{R}$	=	square array of uniformly distributed random numbers
R	=	Resistor
r	=	number of modes used for response analysis
U_R	=	amplitude of excitation
$\boldsymbol{v}$	=	electric potential
$\boldsymbol{x}$	=	physical displacement vector, m
$\ddot{x}$	=	acceleration vector, m/s^2
$\boldsymbol{x}_L$	=	displacement of the internal degrees of freedom, m
$\boldsymbol{x}_R$	=	displacement of the boundary, m
$\ddot{\boldsymbol{x}}_L$	=	acceleration of the internal degrees of freedom, g
$\ddot{\boldsymbol{x}}_R$	=	acceleration of the boundary degrees of freedom, g
$\boldsymbol{\varepsilon}$	=	mechanical strain
$\boldsymbol{\Phi}$	=	finite element modal matrix
$\boldsymbol{\Phi}^E$	=	inaccurate finite element modal matrix
$\boldsymbol{\phi}_L$	=	transformation matrix to relate $\boldsymbol{q}_m$ and $\boldsymbol{x}_L$
$\boldsymbol{\phi}_m$	=	mode shapes of the master degrees of freedom
$\boldsymbol{\phi}_R$	=	transformation matrix to relate the rigid body displacement at $\boldsymbol{x}_R$ and $\boldsymbol{x}_L$
$\boldsymbol{\eta}$	=	modal displacement vector
η^r	=	loss factor of the rth mode
Ω	=	forcing frequency, rad/s
ρ	=	material density, kg/m^3
$\boldsymbol{\sigma}$	=	stress tensor, N/m^2

ω	=	frequency of vibration, rad/s
$\boldsymbol{\psi}$	=	experimental or 'nominal' modal matrix
$\boldsymbol{\psi}^E$	=	inaccurate experimental madal matrix
ζ	=	modal damping coefficient

Subscripts

a	=	active degrees of freedom
B	=	boundary degrees of freedom after the Craig-Bampton reduction
d	=	deleted degrees of freedom
k	=	mode number
L	=	internal degrees of freedom
m	=	number of modes used in the reduction
n	=	total degrees of freedom
p	=	output location
q	=	input location
R	=	boundary degrees of freedom

Superscripts

E	=	erroneous parameter
†	=	generalised inverse
T	=	matrix transpose
-1	=	matrix inverse

Abbreviations

BFAC	=	Base Force Assurance Criterion
CAC	=	Current Assurance Criterion
CFRP	=	Carbon Fibre Reinforced Plastic
CLA	=	Coupled Load Analysis
COMAC	=	COordinate Modal Assurance Criterion
DOF(s)	=	Degree(s) Of Freedom
EFI	=	EFfective Independence
FDAC	=	Frequency Domain Assurance Criterion
FE	=	Finite Element

FEM(s)	=	Finite Element Model(s)
FRAC	=	Frequency Response Assurance Criterion
FRF	=	Frequency Response Function
IMAC	=	Improved Modal Assurance Criterion
IRS	=	Improved Reduced System
MAC	=	Modal Assurance Criterion
MFS	=	Multi-Functional Structure
MSE	=	Modal Strain Energy
MSF	=	Modal Scale Factor
NCO	=	Normalised Cross-Orthogonality
NMR	=	Number of Modes in the Reduction
NTM	=	Number of Target Modes
SEREP	=	System Equivalent Reduction Expansion Process
SMP	=	Shape Memory Polymer
TAM	=	Test-Analysis Model

Chapter 1.
Introduction

1.1 The Need for Model Correlation

Finite element analysis is typically used to predict the structural dynamic characteristics of spacecraft structures and to verify their design margins. The accuracy of the Finite Element Model (FEM) is crucial as these models are used to predict the load experienced by a spacecraft during the launch, using a Coupled Load Analysis (CLA) of the spacecraft and launch vehicle models [1]. Generally, the initial design of the spacecraft is conducted using the loads specified in the launcher manual. As both the spacecraft and the launch vehicles are flexible in nature and they form a coupled dynamic system, an accurate prediction of the loads exchanged can only be calculated when the dynamic characteristics of both of the individual systems are known [2]. When the FEM of the spacecraft is available after the initial design, the launch agency will perform the CLA using the coupled FEM of spacecraft and the launch vehicle and the results of this analysis produce a more accurate prediction of loads experienced by the spacecraft. Subsequently, these loads are used to verify the design margins of the structural elements [3].

Dynamic testing of the coupled system in practice is limited primarily due to the problems in representing the actual loading condition [4] and the large size of the launch vehicle, therefore final verification using analysis derived loads is the only option. Hence, inaccuracies in the FEM of the spacecraft may result in the inaccurate load predictions and ultimately catastrophic failures of the system. This issue is compounded by the fact that, the design margins of the space systems are generally less than those used in other areas (e.g. automotive) to enhance the structural efficiency. An accurate FEM also reduces the number of expensive tests. Hence, it is essential to have an accurate FEM

of both the launch vehicle and the spacecraft for a reliable prediction of the loads to achieve a robust design.

The verification of a FEM refers the process of checking whether some aspects of the model are correct or not. In contrast, validation is a checking process to assess the capability of an object such as a mathematical model or a measurement, to represent the behaviour of interest sufficiently well to be fit for the purpose [5]. Generally, the validation is conducted with the help of a correlation method. The correlation is the process of comparing physical model responses with mathematical model prediction to quantify the degree of similarity or dissimilarity between the two models. Typically, launch agencies give the minimum thresholds for the parameters of the correlation and a mathematical model that satisfies these requirements is deemed to be validated and assumed to give predictions that are sufficiently accurate and fit for purpose. If the FEM does not comply with the requirement, a model updating procedure is initiated to modify the FEM until it meets the requirement. This procedure can be quite time consuming and expensive. Hence, it is necessary to make sure that, the correlation method is meaningful for the required purpose; otherwise, model updating may improve the validation but produce an inferior FEM in terms of the capability to predict the important characteristics such as responses.

Traditionally in the field of spacecraft structures, we deal with purely mechanical systems/models. However, to control the dynamics of the structure using active/passive methods or for other purposes as in the case of multi-functional structures, the analysis of multi-physics models become necessary. A method to assess the accuracy of such models is vital to improve the analytical predictions and the wide spread use of the modelling techniques. However, specific correlation tools for multi-physics systems are not yet reported for practical applications.

This thesis describes the correlation of FEMs of both spacecraft structures and coupled FEMs of multi-physics subsystems. Although there are response correlation methods such as frequency response assurance criterion which directly compares the frequency responses (details are given in chapter 2); typically in the spacecraft industry, modal reductions and mode superposition

techniques are used in the analyses, therefore the quality of the FEM is generally verified using a modal approach. Modal Assurance Criteria (MAC) [6] and Normalised Cross Orthogonality (NCO) [5] check are the accepted criteria for this purpose in the space industry. Here, the emphasis is to predict the response of the structure under the base excitation as the design of the spacecraft components are based on these responses and base excitation is a commonly used experimental method to qualify the spacecraft structure.

1.2 Scope of the Work

MAC and NCO check are widely used to assess the correlations between the experimentally determined dynamic characteristics and the FEM predictions. These methods perform the correlation by essentially comparing mode shapes, compatibility between the test and the analytical Degree Of Freedom (DOF) needs to be maintained. Often, FEMs contain several hundred thousand or millions of DOFs, whereas during the dynamic tests only a few hundred DOFs are measured, and therefore the lengths of the vectors describing analytical modes and experimental modes are different.

The MAC can be performed without any compatibility issues. In fact, if a modal vector (experimental or analytical) contains some DOF which are not represented in the other vector, these DOFs can simply be discarded in order to obtain vectors of the same length, which can then be 'compared' using the MAC. However, the MAC can only check the match between the vectors obtained from the retained DOFs [1], and here, all the DOFs have the same 'importance' whereas, in reality it is known that some DOFs are more representative than others. Hence, the NCO check utilises the mass matrix as a form of weighing matrix and in this case, the vectors that are compared, must have the same size as that of the mass matrix. This means that if the experimental and analytical vectors have different lengths, a reduction or expansion of DOFs becomes necessary calling for a Test Analysis Model (TAM). In this study, a probabilistic approach will be used to assess the robustness of the System Equivalent Reduction Expansion Process (SEREP) [7, 8] based TAM, when experimental and analytical modes contain different levels of inaccuracy.

The approach is applied to three very different spacecraft models, and Monte Carlo simulations are used to determine the sensitivity of the NCO check to the parameters utilised to produce the SEREP reduced matrix. This is graphically represented in Fig. 1.1. The relation between capability of the finite element models to predict the frequency-response function and the quality of the model correlation determined using NCO check is also investigated. In addition, this study shows a method to optimally choose the sensor locations using the SEREP reduced mass matrix such that the probability to pass the NCO check is increased.

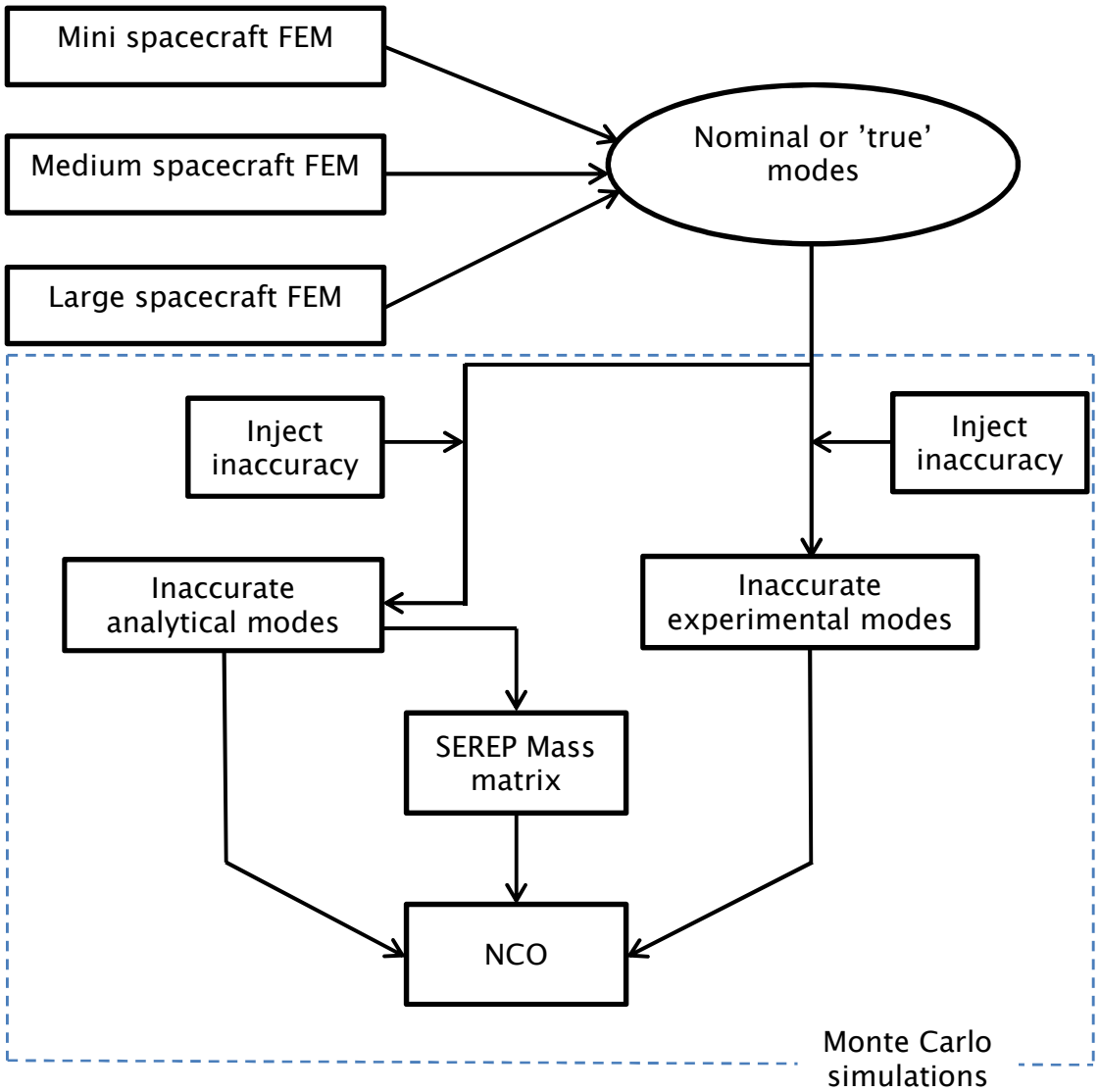

Fig. 1.1 Diagram of sensitivity analysis.

Although MAC and NCO check are the widely accepted correlation tools for space application [9, 10], the effectiveness of these criteria on the base excitation response of spacecraft structure is unknown. To study the effectiveness, the dynamic characteristics obtained from a nominal FEM are considered as the 'true' characteristics and those obtained from the model produced by introducing uncertainty or inaccuracy in the nominal model are considered as the analytically predicted characteristics throughout this study. The correlation is performed using both MAC and NCO check and is observed that, these criteria are not always suitable when the model is used to predict forced response characteristics such as the force transmitted to the base, peak acceleration response, and dynamic displacement in the spacecraft. Thus, a qualitative indicator named as Base Force Assurance Criterion (BFAC) is introduced by comparing the 'true' dynamic force at the base and the finite element predicted force such that the criterion can state the possible error in the peak acceleration and the dynamic displacement under base excitation. The method is applied to assess the performance of three spacecraft structures under base excitation.

To meet the specific mission requirements, such as vibration attenuation and frequency tuning of the spacecraft subsystems, the multi-physics or multifunctional system is developed. In this study, plate-like structures are considered, as they are typical elements utilised in spacecraft structures. The damped sandwich plate can be used in the spacecraft design for the mounting of sensitive electronic modules with the minimum structural vibrations. Sandwich panels are conventionally used for constructing the solar panels and the support deck for the heavier electronics equipment and batteries. The two viscoelastic systems considered for vibration attenuation are a sandwich plate and a honeycomb sandwich panel assembly. In the sandwich plate, viscoelastic layers are constrained between two thin plates of aluminium whereas in the sandwich panel assembly, viscoelastic layers are embedded between two sub panels, each sub panel consists of face sheets and honeycomb core.

The usefulness of conventional MAC and NCO check for the correlation of FEM of a viscoelastic damped sandwich plate and sandwich panels when subjected to harmonic excitation are conducted. The MAC is also computed using the complex eigenvalues to estimate the effect of damping on the correlation. In

addition, the effectiveness of base force assurance criterion to represent the dynamic characteristics of the viscoelastic-damped systems under the base excitation is analysed. The effect of temperature on the MAC and NCO check are studied using the temperature dependent material properties of the viscoelastic systems to determine whether these correlation checks need to be performed at various operating temperature for qualifying the model.

The FEM, which consists of structural and non-structural DOF (coupled FEM) has been effectively used for the analysis of piezoelectric systems. The usefulness of MAC for the correlation of FEM of a piezoelectric system connected with a shunt electric circuit is also analysed when subjected to harmonic excitation. The resonance frequency of this type of system can be easily varied as per the requirement by varying the electric circuit parameters. A new correlation method named as Current Assurance Criterion (CAC) is defined based on the frequency dependant current in the electric circuit.

1.2.1 Objectives of the Current Work

The objectives of this study are summarised as follows.

- To assess the robustness of a SEREP based TAM when experimental and analytical modes of real spacecraft contain different levels of inaccuracy and determine the various parameters that affect the SEREP.
- Analyse the effectiveness of NCO check in predicting the receptance and check whether the current practice to qualify the FEM is sufficient to meet the structural requirements.
- Identify a method to improve the NCO correlation by a suitable selection of sensor locations.
- Assess the usefulness of MAC and NCO check to predict the FEM capability to represent the dynamic response under base excitation. This has led to the introduction of a novel correlation method to qualify the spacecraft FEM for response analysis.
- Analyse the usefulness of standard correlation methods (MAC and NCO) to qualify the FEM of multi-physics systems and possibly develop a specific correlation method for the multi-physics systems.

1.3 Thesis Structure

The works reported in this thesis are structured as follows. In Chapter 2, reviews of various technologies for the validation of FEM of conventional structures are presented. This Chapter 2 also covers the recent developments in the field of multi-physics or multifunctional structures. Chapter 3 presents the effect of inaccuracies on the SEREP, which is widely used for the model reduction method in the correlation study and the parameters that affect the NCO correlation are described. A general conclusion on the SEREP is discerned using three different spacecraft finite element models. Effectiveness of MAC and NCO check on the prediction of forced response characteristics during the base excitation of spacecraft structures are discussed in Chapter 4. A newly introduced base force assurance criterion is also presented and a comparison between the synthetic modes and the physically altered FEM modes are also discussed. Chapter 5 and Chapter 6, describe the correlation aspects of two multi-physics systems - viscoelastic damped system and shunted piezoelectric system - which can be used for the aerospace applications. The effect of temperature on standard correlation methods and MAC using the complex modes are also described in Chapter 5. A correlation tool for the shunted piezoelectric system is introduced in Chapter 6. The final chapter summarise the overall conclusions, contributions made in this work and some suggestions for the further research.

Chapter 2.
Developments in Model Validation and Multi-Physics Systems

The first part of this chapter summarises the well-known methods for model correlation/validation whereas the second part presents the current state of art of multi-functional or multi-physics systems for aerospace application with an emphasis on spacecraft related technology. Details of additional relevant literature are included in the appropriate chapters.

2.1 Finite Element Model Validation

2.1.1 Model Reduction

Generally, a FEM of a spacecraft contains several hundred thousand DOFs. However, the dynamic test is conducted with a few hundred accelerometers (i.e., a few hundred DOFs) due to the complexity of the measurement system and sufficiency of few important modes, termed target modes, to represent the spacecraft dynamics to meet the required accuracy. This leads to a disparity in the DOFs during the correlation process such as NCO. Hence, either the test results need to be expanded or the Finite Element (FE) modes be reduced to the test locations [11, 12]. The first approach requires an algorithm, which utilises the FE modes to expand the test data, and because the accuracy of the FEM has not been proved yet, the expanded modes could be distorted by the errors in the FEM [7]. Normally it is considered that, the experimental results obtained from a well-planned and careful dynamic test along with a suitable modal extraction are more accurate than the analytical results, primarily attributed to the advances in instrumentation and measurement techniques[5, 13]. Hence, in the second popular approach, a reduced test-analysis model is

generated by using the unaltered experimental data and reducing the analytical data to the test locations. It is important to capture the vital dynamics of the system using the available sensors or accelerometers. To aid this, Kammer and Tinker [14] used an effective independence based method and Papadimitriou [15] proposed a genetic algorithm to select the optimum locations of the sensors in the vibration test. To reduce the analytical results to these test locations, different model reduction techniques are used and these are summarised in the following section.

2.1.1.1 Static Reduction

Various reduction methods have been developed for generating the TAM. The most widely used reduction method is static reduction [16] proposed by Guyan, where the reduction matrix is generated purely from the stiffness matrix. The undamped equation that governs the dynamics of the system can be expressed using mass matrix, $\boldsymbol{M}$ and stiffness matrix, $\boldsymbol{K}$ as:

$$\boldsymbol{M}\ddot{\boldsymbol{x}} + \boldsymbol{K}\boldsymbol{x} = \boldsymbol{f} \tag{2.1}$$

where $\boldsymbol{x}$ and $\ddot{\boldsymbol{x}}$ are the vectors containing the displacement and acceleration respectively and $\boldsymbol{f}$ is the applied force vector**.** This equation can be partitioned as:

$$\begin{bmatrix} \boldsymbol{M}_{mm} & \boldsymbol{M}_{ms} \\ \boldsymbol{M}_{sm} & \boldsymbol{M}_{ss} \end{bmatrix} \begin{Bmatrix} \ddot{\boldsymbol{x}}_m \\ \ddot{\boldsymbol{x}}_s \end{Bmatrix} + \begin{bmatrix} \boldsymbol{K}_{mm} & \boldsymbol{K}_{ms} \\ \boldsymbol{K}_{sm} & \boldsymbol{K}_{ss} \end{bmatrix} \begin{Bmatrix} \boldsymbol{x}_m \\ \boldsymbol{x}_s \end{Bmatrix} = \begin{Bmatrix} \boldsymbol{f}_m \\ 0 \end{Bmatrix} \tag{2.2}$$

where the subscript *m* represents the DOFs that need to be retained (master DOF) whereas the subscript *s* represents DOFs that have to be eliminated or reduced. If the partition is performed in such a way that all the DOFs with applied forces, large mass and inertia are collected in master or retained DOFs *m,* then the mass and inertia of the eliminated DOFs can be neglected. Hence, the second part of the Eq. (2.2) gives,

$$\boldsymbol{x}_s = -\boldsymbol{K}_{ss}^{-1}\boldsymbol{K}_{sm}\boldsymbol{x}_m \,. \tag{2.3}$$

The total displacement can be written in terms of the retained DOFs as:

$$\boldsymbol{x} = \begin{Bmatrix} \boldsymbol{x}_m \\ \boldsymbol{x}_s \end{Bmatrix} = \begin{bmatrix} \boldsymbol{I} \\ -\boldsymbol{K}_{ss}^{-1}\boldsymbol{K}_{sm} \end{bmatrix} \boldsymbol{x}_m = \boldsymbol{T}_{Stat}\boldsymbol{x}_m . \tag{2.4}$$

Using the static reduction matrix, $\boldsymbol{T}_{Stat}$, the total kinetic energy of the dynamic system, *T* and the potential energy *V* can be calculated as:

$$T = \frac{1}{2}\dot{\boldsymbol{x}}_m^T \boldsymbol{T}_{Stat}^T \boldsymbol{M}\boldsymbol{T}_{Stat}\dot{\boldsymbol{x}}_m \tag{2.5}$$

$$V = \frac{1}{2}\boldsymbol{x}_m^T \boldsymbol{T}_{Stat}^T \boldsymbol{K}\boldsymbol{T}_{Stat}\boldsymbol{x}_m \tag{2.6}$$

where $\dot{\boldsymbol{x}}$ is the velocity and superscript *T* represent the transpose. Then the reduced mass matrix, $\boldsymbol{M}_{Stat}$ which can be used for the TAM becomes,

$$\boldsymbol{M}_{Stat} = \boldsymbol{T}_{Stat}^T \boldsymbol{M}\boldsymbol{T}_{Stat} . \tag{2.7}$$

Similarly, static reduced stiffness matrix, $\boldsymbol{K}_{Stat}$ is given by:

$$\boldsymbol{K}_{Stat} = \boldsymbol{T}_{Stat}^T \boldsymbol{K}\boldsymbol{T}_{Stat} . \tag{2.8}$$

The eigenvalues of the reduced system can be obtained using the $\boldsymbol{M}_{Stat}$ and $\boldsymbol{K}_{Stat}$ as:

$$(\boldsymbol{K}_{Stat} - \boldsymbol{\omega}^2 \boldsymbol{M}_{Stat})\boldsymbol{\Phi}_m = \boldsymbol{0} \tag{2.9}$$

where ω^2 is the eigenvalue and $\boldsymbol{\phi}_m$ is the mode shape. This procedure gives an exact reduction for a static problem, but often fails to represent a dynamic system accurately. This is because the inertia terms of the reduced DOFs are ignored in the formulation of the transformation matrix. Irons [17] also suggested a similar modal reduction by eliminating the DOFs with negligible inertia forces. Shah and Raymund [18] introduced an algorithm to choose the master DOFs to enhance the accuracy of this reduction method. Kidder [19] incorporated the inertia terms ignored in the static reduction and improved the ability of the reduced system to represent the dynamic characteristics of the original system. This method is described in the following section.

2.1.1.2 Dynamic Reduction

Consider the eigenvalue problem of the undamped structural system shown in Eq. (2.2). For each mode, $\boldsymbol{\phi}$ the equation can be written as:

$$\left(\begin{bmatrix} \boldsymbol{K}_{mm} & \boldsymbol{K}_{ms} \\ \boldsymbol{K}_{sm} & \boldsymbol{K}_{ss} \end{bmatrix} - \omega^2 \begin{bmatrix} \boldsymbol{M}_{mm} & \boldsymbol{M}_{ms} \\ \boldsymbol{M}_{sm} & \boldsymbol{M}_{ss} \end{bmatrix}\right) \begin{Bmatrix} \boldsymbol{\phi}_m \\ \boldsymbol{\phi}_s \end{Bmatrix} = \mathbf{0} \tag{2.10}$$

where ω is the circular frequencies of the system. If the solution is required to be obtained in terms of the master DOF, *m*, then the dynamic reduction [19, 20] can be employed. Using the second part of the Eq. (2.10), the unwanted DOFs can be eliminated as:

$$\boldsymbol{\phi}_s = -\left(\boldsymbol{K}_{ss} - \omega^2 \boldsymbol{M}_{ss}\right)^{-1} \left(\boldsymbol{K}_{sm} - \omega^2 \boldsymbol{M}_{sm}\right) \boldsymbol{\phi}_m = \boldsymbol{T}_{Dyn} \boldsymbol{\phi}_m \tag{2.11}$$

Substitution, Eq. (2.11) in Eq. (2.10) yields the eigenvalue problem in the reduced DOFs as:

$$\left(\left(\boldsymbol{K}_{mm} - \boldsymbol{K}_{ms}\boldsymbol{T}_{Dyn}\right) - \omega^2 \left(\boldsymbol{M}_{mm} - \boldsymbol{M}_{ms}\boldsymbol{T}_{Dyn}\right)\right) \boldsymbol{\phi}_m = \mathbf{0} \tag{2.12}$$

However, it should be noted that, the eigenvalue is required for the computation of $\boldsymbol{T}_{Dyn}$ which is not yet known. As a starting point, the eigenvalue can be taken to be zero [21]or the eigenvalue obtained from a static reduced system. Then, solve the reduced dynamic equation and recalculate the $\boldsymbol{T}_{Dyn}$ with the updated eigenvalue and continue the process until convergence is reached. The inertia effect of reduced DOFs, which are completely ignored in the static reduction, is accommodated here, but the reduction is exact only at a particular reference frequency and the accuracy of the dynamic characteristics will deteriorate as we move away from the reference frequency. The reduced mass and stiffness matrix for the TAM can be calculated as:

$$\boldsymbol{M}_{Dyn} = \boldsymbol{T}_{Dyn}^T \boldsymbol{M} \boldsymbol{T}_{Dyn} \tag{2.13}$$

and

$$\boldsymbol{K}_{Dyn} = \boldsymbol{T}_{Dyn}^T \boldsymbol{K} \boldsymbol{T}_{Dyn} \tag{2.14}$$

respectively.

2.1.1.3 Improved Reduced System

O'Callahan [22] developed an approximate reduction technique called Improved Reduced System (IRS) by the force adjustment in the static reduction. This force adjustment will account for the distributed inertia forces associated with the reduced DOFs. In the absence of external and damping forces, the inertia forces are in equilibrium with the elastic forces. Hence, the Eq. (2.1) can be expressed for a harmonic displacement, $\boldsymbol{x}(\omega)e^{i\omega t}$ as:

$$\boldsymbol{K}\boldsymbol{x}(\omega) = \omega^2 \boldsymbol{M}\boldsymbol{x}(\omega)\,. \tag{2.15}$$

Using the static reduction, the displacement can be expressed in terms of the master DOF, $\boldsymbol{x}_m(\omega)$ as:

$$\boldsymbol{x}(\omega) = \boldsymbol{T}_{Stat}\boldsymbol{x}_m(\omega)\,. \tag{2.16}$$

Inserting this into Eq. (2.15) leads to the approximated equation:

$$\boldsymbol{K}\boldsymbol{T}_{Stat}\boldsymbol{x}_m(\omega) = \omega^2 \boldsymbol{M}\boldsymbol{T}_{Stat}\boldsymbol{x}_m(\omega)\,. \tag{2.17}$$

Pre-multiply this equation with $\boldsymbol{T}_{Stat}^T$ and using the definition of static TAM, gives:

$$\omega^2 \boldsymbol{x}_m(\omega) = \boldsymbol{M}_{Stat}^{-1}\boldsymbol{K}_{Stat}\boldsymbol{x}_m(\omega)\,. \tag{2.18}$$

Segregating the DOFs of the stiffness matrix and substituting Eq. (2.18) in Eq. (2.15) yields:

$$\begin{bmatrix} \boldsymbol{K}_{mm} & \boldsymbol{K}_{ms} \\ \boldsymbol{K}_{sm} & \boldsymbol{K}_{ss} \end{bmatrix} \begin{Bmatrix} \boldsymbol{x}_m(\omega) \\ \boldsymbol{x}_s(\omega) \end{Bmatrix} = \boldsymbol{M}\boldsymbol{T}_{Stat}\boldsymbol{M}_{Stat}^{-1}\boldsymbol{K}_{Stat}\boldsymbol{x}_m(\omega)\,. \tag{2.19}$$

The full displacement can be expressed in terms of $\boldsymbol{x}_m(\omega)$ as:

$$\boldsymbol{x}(\omega) = \begin{Bmatrix} \boldsymbol{x}_m(\omega) \\ \boldsymbol{x}_s(\omega) \end{Bmatrix} = \boldsymbol{T}_{IRS}\boldsymbol{x}_m(\omega) \tag{2.20}$$

where,

$$\boldsymbol{T}_{IRS} = \left[\boldsymbol{T}_{Stat} + \begin{bmatrix} \boldsymbol{0} & \boldsymbol{0} \\ \boldsymbol{0} & \boldsymbol{K}_{ss}^{-1} \end{bmatrix} \boldsymbol{M}\boldsymbol{T}_{Stat} \boldsymbol{M}_{Stat}^{-1} \boldsymbol{K}_{Stat} \right]. \tag{2.21}$$

Then the reduced mass and stiffness matrix using the IRS method can be calculated as:

$$\boldsymbol{M}_{IRS} = \boldsymbol{T}_{IRS}^{T} \boldsymbol{M}\boldsymbol{T}_{IRS} \tag{2.22}$$

and

$$\boldsymbol{K}_{IRS} = \boldsymbol{T}_{IRS}^{T} \boldsymbol{K}\boldsymbol{T}_{IRS} \tag{2.23}$$

respectively. It can be observed that, the method does not require a solution of the full system eigenvalues but can reduce the system with better accuracy to predict the dynamics than static reduction. However, the reduced system can give only approximate dynamic characteristics. Friswell *et al.* [23] extended the IRS method by using the dynamic reduction as the basic transformation instead of static reduction.

2.1.1.4 Other Reduction Methods

Kammer [7] developed a reduction technique using FEM normal modes. This method is the most suitable for the test-analysis correlation because it does not require a re-computation of TAM for each frequency as in the case of the dynamic reduction. This method is commonly known as the SEREP after O'Callahan *et al.* [8] termed the procedure. The reduction can exactly predict the FE modes and the frequencies of the actual system even after the reduction. The procedure uses the normal modes for the TAM generation and yields a very small matrix that enables an easy inversion as shown in the following chapter. To predict the residual dynamic effects in a more accurate way, Kammer [24] introduced a hybrid TAM by combining the ability of the modal TAM [7] to accurately represent the FEM target modes with the static TAM representation for the residual modes. Sastry *et al.* [25] proposed an interactive SEREP procedure to extract the high frequency response from a reduced FEM.

In order to avoid the modal based correlation matrix in the mid frequency range test analysis verification, a frequency response based reduction technique was presented in Ref. [26]. The principal directions were extracted directly from the analytical frequency response and used to derive the transformation matrix to reduce the impedance matrix [27] to the sensor locations. This reduction technique is particularly suitable for systems with high modal density in the frequency range of interest and avoids the difficult task of selecting the dynamically important target modes. However, the accuracy of the technique is dependent on the number of principal directions used in the model reduction.

2.1.2 Model Correlation Methods

The experimentally determined modal parameters such as natural frequency, mode shapes and Frequency Response Function (FRF) are often needed a comparison for the corresponding analytical or predicted values. Hasselman *et al.* [4] has been performed a survey on the correlation methods used in the aerospace industries. The comparison of natural frequencies is straight forward, but mode shape and FRF comparisons are usually performed using a correlation method. Some available correlation methods are described below.

2.1.2.1 Modal Scale Factor

For mode shape comparison, the slope between an experimental mode, $\boldsymbol{\psi}$ and an analytical mode, $\boldsymbol{\phi}$ can be computed. This is knows as Modal Scale Factor (MSF) [5] and can be calculated using either the analytical or the experimental mode as the reference. If the analytical mode shape is required to be the reference, then the MSF can be calculated by the equation:

$$MSF_{\psi\phi} = \frac{\sum_{j=1}^{a} \boldsymbol{\psi}_j \boldsymbol{\phi}_j^*}{\sum_{j=1}^{a} \boldsymbol{\phi}_j \boldsymbol{\phi}_j^*} \tag{2.24}$$

where *a* is the number DOFs for which both experimental and analytical mode shapes are available, and the superscript * indicates the complex conjugate when mode shape is complex. Similarly, MSF with the experimental mode as reference is given by:

$$MSF_{\phi\psi} = \frac{\sum_{j=1}^{a} \boldsymbol{\phi}_j \boldsymbol{\psi}_j^*}{\sum_{j=1}^{a} \boldsymbol{\psi}_j \boldsymbol{\psi}_j^*}. \tag{2.25}$$

The MSF do not give any indication of the quality of fit of the DOFs to the straight line but only the slope of the best straight line.

2.1.2.2 Modal Assurance Criterion

The modal assurance criterion can quantitatively give the measure of the least square deviation of modes from the straight line [5, 6]. The MAC can be computed using the equation:

$$\boldsymbol{MAC} = \frac{\left|\boldsymbol{\psi}^T \boldsymbol{\phi}\right|^2}{(\boldsymbol{\psi}^T \boldsymbol{\psi})(\boldsymbol{\phi}^T \boldsymbol{\phi})} \tag{2.26}$$

where $\boldsymbol{\psi}$ is the experimental mode shape and, $\boldsymbol{\phi}$ is the corresponding mode shape from the analytical model. It should be noted that, the MAC value ranges from 0.0 – 1.0 with 1.0 defining two identical modes, and 0.0 for two non-identical modes. For the practical applications, a value above 0.9 is considered as well-correlated mode pairs and a value less than 0.1 is taken as an uncorrelated modes [5, 9, 10]. As in the case of MSF, MAC also fails to identify modes are scattered or the existence of any systematic deviations in the mode pairs.

2.1.2.3 Normalised Cross Orthogonality

If a weighting matrix is include in the MAC, - then the correlation procedure is known as normalised cross orthogonality. Generally, a mass weighting matrix is used in the NCO check, then the equation for NCO check is given by:

$$NCO = \frac{\left|\boldsymbol{\psi}^T \boldsymbol{M}_{TAM} \boldsymbol{\phi}\right|^2}{(\boldsymbol{\psi}^T \boldsymbol{M}_{TAM} \boldsymbol{\psi})(\boldsymbol{\phi}^T \boldsymbol{M}_{TAM} \boldsymbol{\phi})} \tag{2.27}$$

To overcome the DOF disparity between the analytical and experimental data, the analytical mass matrix (often available to all the DOFs) needs to be reduced to the DOFs for which experimental data is available. This can be accomplished by using methods such as static reduction or SEREP. However, SEREP is the widely used practical approach, in which a pseudo mass matrix of the required dimension can be computed from the mode shapes [5]. If the experimental and analytical modes are identical then the NCO will be an identity matrix as mode shapes are orthogonal to the mass matrix. In practice, these two set of vectors are different and the correlation using the NCO check is considered to be successful by different space agencies [9, 10] if the diagonal values of NCO matrix are greater than 0.9 and all other terms in the NCO matrix are less than 0.1.

2.1.2.4 Improved MAC

In certain situations, the computed value of MAC belies the expected level of correlation obtained from the visual inspection of the actual mode shapes. The problem can be primarily attributed to the selection of DOFs and hence the largest amplitude of the mode may not be captured. Correlation can further reduce, if the selected DOFs are greatly affected by measurement noise. Hence, in the Improved MAC (IMAC) calculation, some DOF are selectively eliminated which cause a maximum reduction in the MAC [5]. However, precaution should be taken to eliminate only the inaccurate data rather than all those DOFs reducing the MAC, which actually indicate the lack of correlation.

2.1.2.5 Coordinate MAC

The contribution of individual DOFs in the MAC is not explicitly known as a summation is made over all the DOFs in the mode pairs. The correlation as a function of individual DOFs can be carried out using Coordinate MAC or COMAC [28]. The COMAC for an individual DOF, i is given by:

$$COMAC_i = \frac{\left(\sum_{l=1}^{L} |\psi_{il}\phi_{il}|\right)^2}{\sum_{l=1}^{L}\psi_{il}^2 \sum_{l=1}^{L}\phi_{il}^2} \tag{2.28}$$

where l, represents an individual mode pair and L is the total number of modes considered in the correlation. It should be noted that the DOF at which the COMAC value is low, is not necessarily the location of the discrepancy between the mode pairs, but is the location where it is felt.

2.1.2.6 Frequency Domain Assurance Criterion

Using the MAC approach to the measured FRF ($\boldsymbol{H}_X$) and analytical FRF($\boldsymbol{H}_A$), these two vectors can be correlated. The procedure is known as Frequency Domain Assurance Criterion (FDAC) [29] and is given by the equation:

$$\boldsymbol{FDAC}(\omega_A, \omega_X, \boldsymbol{j}) = \frac{\left|\{\boldsymbol{H}_A(\omega_A)\}_j^T \{\boldsymbol{H}_X(\omega_X)\}_j\right|^2}{\left(\{\boldsymbol{H}_A(\omega_A)\}_j^T \{\boldsymbol{H}_A(\omega_A)\}_j\right)\left(\{\boldsymbol{H}_X(\omega_X)\}_j^T \{\boldsymbol{H}_X(\omega_X)\}_j\right)} \tag{2.29}$$

where j corresponds to the particular columns of $\boldsymbol{H}$, ω_A and ω_X correspond to the frequency at which $\{\boldsymbol{H}_A\}_j$ and $\{\boldsymbol{H}_X\}_j$ respectively were determined. The FDAC equation indicates that, its value can vary from 0.0 to 1.0. A value of 1.0 indicates a perfect correlation between the two FRFs and 0.0 indicates fully uncorrelated FRF pair.

2.1.2.7 Frequency Response Assurance Criterion

The DOF based FRF correlation can be performed using the Frequency Response Assurance Criterion (FRAC) [5, 30]. This is equivalent to the COMAC for the mode shapes given in Eq. (2.28). The direct comparison of FRFs using either FDAC or FRAC is problematic, when there is a shift in the resonance frequencies of analytical and experimental FRFs, which is very common in the complex structures such as spacecraft. In addition, correlating the FRFs of different locations of a complex structure in the required frequency band is a tedious task.

2.1.3 Model Update

When the results of the correlation exercise carried out using the methods described in the previous section show a poor level of agreement between the experimental and analytical results, it is standard practice to update the FEM to improve the correlation. This can be a very lengthy process, as some agencies impose that the model update must be done by physically justified modifications, rather than mathematically justified arbitrary modifications of stiffness or mass matrix. Some model update techniques are summarised below.

Using the experimentally determined natural frequencies and mode shapes, Collins *et al.* [31] developed a general statistical approach to update the stiffness and mass matrices of a FEM, which has the capability of providing modal characteristics which are consistent with the experimental data. The method does not require measurement at all the analytical DOFs. Lin *et al*. [13] improved this method by incorporating both analytical and experimental modal data to estimate the eigensensitivity. Berman and Nagy [32] also used the measured real normal modes and natural frequencies to improve the analytically determined mass and stiffness matrices of a linear system. This procedure is known as analytical model improvement and can yield a system whose modes precisely match with those obtained in testing. However, the procedure failed to retain the physical properties of the stiffness matrix. To overcome this difficulty, experimentally determined mode data and structural connectivity information obtained from the analytical method were used to optimally improve the deficient analytical stiffness matrix [33]. This procedure is known as stiffness matrix adjustment and optimisation is achieved by minimizing the percentage change to each stiffness coefficient subjected to symmetry constraints, connectivity constraints and constraints based on force equilibrium. The obtained stiffness matrix can retain the physical configuration of the analytical model and exactly reproduces the modes used in the procedure.

Butland and Avitabile [34] used the modal parameters obtained from the test to update the reduced order finite element models of two subsystems and then combined using component mode synthesis to generate a test updated system

level model. The inverse technique has been applied to update the damping and stiffness matrices of the finite element models by Starek and Inman [35]. The main advantage of this method is that, it can also be used for updating the models, which exhibit rigid body modes. Mottershead and Friswell [36] presented a survey on the different model updating techniques. Lin and Zhu [37] used the measured response function under base excitation to identify the mass and stiffness matrix modelling errors and directly used them to update the mathematical model. They applied the method to identify the modelling errors in a practical structure and also demonstrated that the method can give reasonable results even with 3% measurement noise in the response function.

2.1.4 Other Developments in Model Correlation

Bergman *et al*. [38] used a probabilistic investigation to quantify the effect of errors in the experimental modes on the test-analysis orthogonality. They analysed a typical spacecraft structure using static, modal, and IRS reduction methods and observed that test-analysis orthogonality is highly sensitive to the experimental errors. A fixed percentage of experimental error was simulated using a simple equation and Monte Carlo simulations were employed to estimate the probability of meeting the orthogonality criteria. Aglietti *et al*. [39, 40] also used a probabilistic approach to assess the effect of inaccuracies in the mode shape on the SEREP TAM using a spacecraft model. They also showed that sensor locations can be optimally chosen to increase the probability to pass the NCO check by using the effective independence criterion. Avitabile [41] described the various considerations to be taken to avoid the pitfalls in the test analysis correlation process.

2.2 Multi-Physics/ Multi-Functional Systems

The integration of multi-physics systems within the spacecraft structure to modify dynamic characteristics, or multifunctional structures to improve the overall spacecraft mass efficiency is an area of growing interest, which in turn creates the need for appropriate criteria to correlate the mathematical models of structures integrating these systems. Current development in the multi-

physics or Multi-Functional Systems (MFS) for spacecraft applications were reviewed by Aglietti *et al*. [42] and Gibson [43]. Noor *et al*. [44] reported the advancement in the materials and structures for the design of multi-functional aerospace systems. The MFS technologies can be grouped into various categories, namely:

- Smart Materials and Structures,
- Thermal Control Systems,
- Multi-functional Power Structures,
- Integrated Electronics,
- Harness Technology,
- Other Developments.

2.2.1 Smart Materials and Structures

The developments of structural systems that can change shape and size on the application of external stimuli or control signals have wide applications in spacecraft design. It can also respond to internal changes such as stress or shape and these characteristics can be used for the vibration control and the health monitoring of the system. Chopra [45] presented an extensive review of available smart structures technologies. The electrostatic vibration analysis using the piezoelectric material has been performed by Eernisse[46] and Allik and Hughes[47]. Aglietti *et. al* [48] used different modelling techniques to analyse the piezoelectric actuated panels and the results were compared with the experimentally determined parameters. Wang *et. al* [49] introduced a mixed piezo-thermo-elastic model to analyse thermal deformation in a pre-stressed piezoelectric actuator. The piezoelectric systems have been used by many researchers for the vibration control [50-54]. The base excitation analysis of a magnetic seismic mass moving past the coil to generate the power from the vibration has been performed by Stephen [55].

Acrylic based electro-elastomers exhibit considerable strains under the application of voltage. In Ref. [56] such a material system has been developed and the strain obtained far exceeds the performance of piezoelectric or shape memory materials. This multi-functional electro-elastomer consists of polymer

sheets and suitable flexible electrodes and the system can extend to 10 percentage of its original length. Another important feature is that, when compressed, it can generate an electric field. This can act as an actuator for space telescopes and trusses for morphing structures. Torquato *et al*. [57] demonstrated the optimisation procedure to maximise the microstructure of composite materials for simultaneous transport of heat and electricity. The sum of the effective thermal and electrical conductivities was optimised using linear programming techniques. The optimal composite was found to be a bi-continuous structure. Minimisation of the sum of the electrical and thermal conductivities results in a three dimensional checkerboard microstructure [58]. A shape reversing structural sandwich panel was developed using shape memory alloy face sheets and a truss core by Elzey *et al.* [59]. It was observed that, alternative heating of top and bottom face sheets, forces the sandwich panel to a fully reversible deformation.

Shape Memory Polymer (SMP) materials were used to fabricate inflatable antenna truss and space reflectors by Lin *et al*. [60]. These materials are initially flexible to facilitate packaging and deployment. SMP based inflatable structures have high compaction along with high strength and avoid the need of constant pressurised gas for maintaining the inflation by making use of heat energy for enhancing the rigidity of the polymer and the properties of SMP laminates can also be tailored to achieve very low coefficients of thermal expansion.

2.2.2 Thermal Control Systems

Different active and passive thermal control systems are utilised for spacecraft thermal management. A heat pipe embedded sandwich panel is an example of a MFS. The thermal management of multi-functional support structures was carried out using pitch based high conductive high modulus Carbon Fibre Reinforced Plastic (CFRP) prepreg face sheets and aluminium honeycomb core is reported in [61]. Thermal conductivity in the longitudinal and transverse direction was observed to be 420 W/mK and 1.2 W/mK respectively for a prepreg with 0.53 fibre volume fraction. Through the thickness thermal conductivity is found to be approaximately 1.0 W/mK. By adopting a specific

face sheet layup, it is possible to achieve in-plane conductivity of approaximately 200 W/mK. This is within the range of thermal conductivity of aluminium.

Using analysis of variance, the thermal design variables of the spacecraft structure having encapsulated electronics was carried out by Jang *et al*. [62]. It was observed that the conductivity of the interface layer between the electronic module and the structure panel is an important parameter for high heat dissipation. Thermally conductive and electrically insulated urethane film adhesive was used for this purpose. The effect of conductivity changes of the prepreg fibres used for the face sheets was nominal due to the small cross-sectional area. Baturkin [63] surveyed various technologies used currently for thermal control of micro satellites (10-100 kg). It was observed that passive means to regulate structure temperature level are very common, whereas passive, semi-passive and active means are used to regulate equipment temperature.

An advanced breadboard sandwich panel was constructed of carbon fabric (fibre YS-15, resin RS-11) honeycomb core and carbon fabric (fibre XN-25, resin RS-11) face skins to obtain exceptionally good through the thickness thermal conductivity and low Coefficient of Thermal Expansion (CTE) compared to the conventional sandwich structures was reported in Ref. [64]. Density of the developed honeycomb core was 72.1 kg/m^3. A light-weight support structure for a spacecraft was designed using metal and laminated composites in Ref. [65]. The structure showed that the CTE was an order of magnitude less and there was a 35% reduction in mass over the metallic counterpart. This was achieved without deteriorating the dynamic characteristics.

2.2.3 Multi-Functional Power Structures

Spacecraft mass and volume reductions are paramount to improve the spacecraft performance and to reduce the cost. Widely used spacecraft batteries and solar arrays are not conducive to reducing the mass and volume due to its design limitations. An innovative power generation, management and storage using layup construction of flexible copper-indium-gallium-selenium photovoltaic, thin film copper polyimide printed circuit and flexible

solid state thin Li film battery was reported [66]. Pereira *et al*. [67] embedded solid state thin film lithium ion battery into a CFRP laminate and studied its performance under uniaxial loading. The embedded cell did not significantly alter the uniaxial mechanical properties of the CFRP laminate. The performance of thin film batteries under flexure and pressure loadings showed that, thin film batteries can withstand the composite laminate manufacturing environment without degrading electrical performance significantly [68].

Composite prepegs are extensively used in aerospace structures. In order to tap their non-structural aspects such as large surface area, rechargeable thin film solid state batteries were built around a variety of different fibre substrates and formed two types of batteries [69]. In order to utilise the structural properties of the battery and to reduce the mass and the volume, Metzger *et al*. [70] developed positive and negative electrodes using nickel form substrates. These electrodes were bonded together and then configured into a diamond shape honeycomb structure termed the 'PowerCore' [71]. The honeycomb was encased between 0.8 mm aluminium sheets and tested for its load carrying capacity. The core shear modulus obtained was lower than the aluminium honeycomb due to the large cell size of 32.0 mm. Another disadvantage of the new system was the limited battery life of less than 10 cycles although this NiH2 chemistry battery has effective energy density of 100 Wh/kg.

Schwingshackl et. al [72] analysed ten different multi-functional power structure configurations using a structural battery (bicell) and aluminium corrugations to reduce the mass and the volume of an on board power storage system. The dynamic test showed that the chosen system had comparable dynamic characteristics of conventional honeycomb sandwich structure in addition to the energy density of 71.3 Wh/kg [73]. The parasitic volume requirement of the battery is eliminated in this MFS design. Roberts and Aglietti [74] assessed the amount mass that can be saved by incorporating polymer lithium ion batteries into the sandwich panels. The MFS saves the volume requirement of the battery and reduces the total mass by removing the parasitic mass. It was revealed that small spacecraft with high power requirements would benefit the most by adopting this type of MFS.

2.2.4 Integrated Electronics

Conventional spacecraft consist of bulky electronic subsystems assembled in aluminium boxes and mechanically attached to the spacecraft structure. The electronic circuits are realised using printed circuit boards and the electrical connections between the subsystems are achieved using insulated harnesses. To minimise the mass and volume requirement of the electronic systems, spacecraft GPS receiver and telemetry acquisition units were miniaturised and enclosed in a composite enclosure and embedded in a honeycomb sandwich panel [62]. This enclosure bears the mechanical loads and provides thermal conduction and radiation shielding to the electronics. Shatzel *et al*. [75] utilised the structural potential of printed circuit boards to construct a box beam structure.

Rawal et. al [76] developed multi-chip modules, that can be directly bonded to honeycomb sandwich panels, to replace the traditional boards and boxes of electronic packages. Barnett and Rawal [77] developed copper-polyimide flex interconnectors to avoid the bulky and heavy harness connectors and this MFS design have been validated by the Deep Space 1 mission. It was observed that the data collected are within normal limits, indicating the good stability of interconnection system. The fatigue failure mechanisms of 0.127 mm copper strip embedded into a highly loaded dielectric glass epoxy laminate were studied by Hyonny *et al*. [78]. Static and Fatigue testing were performed using the test specimens and the voltage level was continuously monitored to check whether the copper strip had been broken. Strain amplitudes were monitored during the fatigue test and observed that electrical failures occurred for fatigue loading levels below 75% of the ultimate tensile strength.

Data transmission or reception, electric power generation and heat generation for the thermal control of spacecraft were merged into a single piece of hardware termed the Power Antenna by Chmielewski *et al*. [79]. The inflatable large parabolic antenna made of the low mass material Mylar, increases the power generation capacity of the spacecraft. The antenna also converges solar and RF signals. Near the focal plane of the antenna, the concentrated solar energy and RF signal are separated using a low mesh reflector.

2.2.5 Electrical Harness

Redesign of the heavy and voluminous electrical harness and conventional connectors are inevitable to meet the stringent mass, volume and cost requirements of advanced spacecraft. Miniaturization of electronic circuits together with developments in connectors, cables, chassis and structural support for avionics are required as these systems occupy a significant percentage of spacecraft mass. Flexible copper polyimide circuitry was used to interconnect MCM of electronic units by Barnett and Rawal [80]. These flexible electronic units were bonded onto the structural composite panel using adhesives. This MFS design approach maximizes the volume ratio of functional electronics to total electronic packaging. Fosness *et al*. [81] reported that the flexible circuitry can reduce the 65% of volume and 85% of mass of the conventional round wire harness.

Inkjet print electrodes using copper nano ink were used by Kim *et al*. [82] for interconnection of thin film solar cells and thin film batteries. These subsystems and passive electronic components were co-cured with the graphite/epoxy laminate to produce a power laminate. Mechanical loading of the inkjet print electrodes showed a 10% increase in resistance at 1% strain irrespective of the electrode width.

2.2.6 Other Developments

The vibration attenuation at a single frequency or over a range of frequencies can be achieved using viscoelastic materials [83, 84]. It has been proposed that modal loss factor can be used as an index to design such systems [85] and Johnson [83] demonstrated that the loss factor can be easily determined using a commercial finite element program. To protect the electronic module embedded in the sandwich panel from on orbit radiation, Jang et. al [62] used 0.1 mm tungsten layer between the 1 mm CRFP casings. This composite laminate is comparable to 2 mm aluminium sheet in proton shielding capability and also reduce the CTE mismatch.

Marcos *et al*. [86] reported that low energy electron penetration can be avoided by using wolfram with surrounding CFRP. Grasmeyer and Keennon [87] used a genetic algorithm based multi-disciplinary optimisation to integrate the subsystem into a micro air vehicle for the maximum endurance. Lithium ion batteries were used for energy storage in this micro air vehicle due to its high energy density, reliability, and low cost. Ashby [88] reported a method to improve the performance of a system with multi-functionalities based on material performance. The author demonstrated how the method can be applied to reduce mass and cost simultaneously of a structural panel with specified stiffness.

2.3 Summary

This chapter reviewed the currently used FEM validation methods and different multi-functional or multi-physics systems, which can be integrated in spacecraft structures. It has been observed that, although many correlation methods are available for different parameters, the MAC and NCO check using the mode shapes are the widely accepted correlation criteria for the FEM validation of space systems. The NCO check requires a model reduction or expansion to match the incompatibility between the analytical and experimental DOFs and model reduction is preferred due to its higher accuracy. Compared to other reduction techniques, SEREP is a widely used method, and that can be adopted to create the weighting mass matrix of the correct size in the NCO calculation.

The literature review also revealed that very limited work has been done to link the effect of inaccuracies on the mode shape and the model correlation. Robustness of the reduction technique to the noise in the modal parameters is important, as there is a certain level of inaccuracy in both the analytical and experimentally determined modal quantities. Another gap in the state of the art is that despite the base shake dynamic test being the common practice to qualify the spacecraft structures, there is not yet an efficient correlation method which can predict the possible error in the forced response characteristics. Developments in the multi-functional/multi-physics technology are progressing quickly and an increasing number of structural

components can be replaced with these new systems to enhance the overall system performance. However, no specific correlation methods for the multi-functional /multi-physics systems have been reported and it can be seen that a correlation method for these types of systems can enhance the developments in this area.

In the next chapter, the robustness of SEREP to the various inaccuracies will be analysed using a statistical approach. The ability of NCO check to predict the receptance FRF and a method to optimally choose the sensor location for an increased probability to pass the NCO check will also be discussed.

Chapter 3.
Robustness of the System Equivalent Reduction Expansion Process on Spacecraft Structure Model Correlation

3.1 Introduction

The system equivalent reduction expansion process [8] can exactly reproduce the dynamic characteristics of the original system and has been found to be very useful in the normalised cross orthogonality check between analytical and experimental mode shapes. Compared to other reduction techniques, SEREP has advantages such as the reduction can be performed using an arbitrary selection of modes and the reduced system preserves the frequency and mode shapes of the original system for selected modes of interest. Aglietti *et al*. [40] analysed the various available techniques to generate a TAM and identified that SEREP is the most suitable method for the generation of a spacecraft TAM. They also investigated the effect of inaccuracies (implemented as noise) in the mode shape of a spacecraft structure on the SEREP and NCO check. It has been observed that, by maintaining the same number of target modes for the correlation, as the number of modes used in the reduction process increases results in a decrease in the probability of meeting the NCO check. It was also shown that optimality criteria based on the EFfective Independence (EFI) matrix can be utilised to improve the probability of meeting the NCO check. In [39], a probabilistic approach was used to assess the robustness of the MAC and NCO check in the validation of the FEM of a spacecraft and it was shown that when the modes are corrupted by noise, meeting the typical MAC requirement is much easier than meeting the NCO requirement specified by the aerospace agencies[9, 10].

In practice, inaccuracies are not only present in the FE estimation of modal parameters but also in the experimental results [89] and therefore, it is important to assess the effect of both these inaccuracies on the TAM and NCO. The present work extends the preliminary findings reported in [39, 40] and in this work three cases are considered: (a) inaccuracies in the experimental modes, (b) inaccuracies in the analytical mode shapes, (c) inaccuracies in both the experimental and the analytical modes. SEREP based TAMs are generated for three different spacecraft structures and for a set of synthetic random modes to derive general conclusions on the robustness of SEREP based TAM when different percentage of inaccuracies are present in the modes. The inaccuracies are simulated using a simple error model and Monte Carlo simulations were used to quantify the sensitivity of the quality check to the SEREP based TAM. The effects of parameters such as the number of modes used in the SEREP reduction, number of target modes, and the independence between the targets modes on the NCO check are evaluated for different classes of spacecraft FEMs. The capability of spacecraft FEMs to predict the displacement based frequency response function (receptance) when the FEM possess different levels of probabilities to pass the NCO check were also assessed. Finally, a simple optimisation procedure to increase the probability of success in the NCO check using a SEREP-based TAM is described.

3.2 System Equivalent Reduction Expansion Process

In order to present the results of the study, the fundamental theoretical approach used for the model reduction needs to be explained. The Craig-Bampton [90] method is commonly used for the dynamic reduction of spacecraft FEMs. However, Craig-Bampton reduced FEMs contain both physical and modal coordinates and hence cannot be used for the direct comparison with the test results, which are in physical coordinates. A modal reduction followed by an expansion using a suitable output projection matrix is used in SEREP [7, 8, 91]. This method can be used for test analysis correlation studies.

The equation of motion for an n DOF undamped system can be written as:

$$\boldsymbol{M}_{n,n}\ddot{x}_n + \boldsymbol{K}_{n,n}x_n = f \tag{3.1}$$

where $\boldsymbol{M}_{n,n}$, $\boldsymbol{K}_{n,n}$, $\boldsymbol{x}_n$, $\ddot{\boldsymbol{x}}_n$, and $\boldsymbol{f}$ are mass matrix, stiffness matrix, displacement vector, acceleration vector, and the applied force vector respectively. The subscripts denote the dimension of the arrays. The eigensolution of this system can be approximated using *m* modal vectors (*m*<*n*). Then $\boldsymbol{x}_n$ can be obtained as:

$$\boldsymbol{x}_n = \boldsymbol{\Phi}_{n,m}\boldsymbol{\eta}_m \tag{3.2}$$

where $\boldsymbol{\Phi}_{n,m}$ is the modal matrix and $\boldsymbol{\eta}_m$ is the displacement vector in modal coordinates. The vector $\boldsymbol{x}_n$ can be partitioned as measured or active DOFs, $\boldsymbol{x}_a$ and deleted DOFs, $\boldsymbol{x}_d$. Hence,

$$\boldsymbol{x}_a = \boldsymbol{\Phi}_{a,m}\boldsymbol{\eta}_m \tag{3.3}$$

where $\boldsymbol{\Phi}_{a,m}$ is the reduced modal matrix in terms of active DOF and generally, the matrix is not square. If the number of modal coordinates *m* is equal to the number of active DOF *a* (such a condition is known as SEREPa [92]), then the reduced modal matrix becomes square and can be inverted to obtain:

$$\boldsymbol{\eta}_a = \boldsymbol{\Phi}_{a,a}^{-1}\boldsymbol{x}_a\,. \tag{3.4}$$

Generally, the number of active DOF in a spacecraft FEM will be much higher than the number of target modes ($a > m$). Hence, $\boldsymbol{\Phi}_{a,m}$ will be a rectangular matrix and a generalised inverse [93] is required to determine the $\boldsymbol{\eta}_m$. The generalised inverse can be generated by pre-multiplying both sides of Eq. (3.3) by $\boldsymbol{\Phi}_{a,m}^T$, in order to generate a square matrix on the right hand side of the equation; which can then be inverted and used to obtain the equation for $\boldsymbol{\eta}_m$ as:

$$\boldsymbol{\eta}_m = (\boldsymbol{\Phi}_{a,m}^T\boldsymbol{\Phi}_{a,m})^{-1}\boldsymbol{\Phi}_{a,m}^T\boldsymbol{x}_a = \boldsymbol{\Phi}_{a,m}^{\dagger}\boldsymbol{x}_a \tag{3.5}$$

where $\boldsymbol{\Phi}_{a,m}^{\dagger}$ is the generalised inverse of the modal matrix $\boldsymbol{\Phi}_{a,m}$. Hence, the displacement of the full system in terms of the reduced displacement can be determined using Eqs. (3.2), (3.3), and (3.5) as:

$$\boldsymbol{x}_n = \boldsymbol{\Phi}_{n,m}\boldsymbol{\Phi}_{a,m}^{\dagger}\boldsymbol{x}_a . \tag{3.6}$$

Substituting Eq. (3.6) into Eq. (3.1) and pre-multiplying by the transpose of the modal matrix and the transpose of generalised inverse of the modal matrix gives:

$$(\boldsymbol{\Phi}_{a,m}^{\dagger})^T\boldsymbol{\Phi}_{n,m}^T\boldsymbol{M}_{n,n}\boldsymbol{\Phi}_{n,m}\boldsymbol{\Phi}_{a,m}^{\dagger}\ddot{\boldsymbol{x}}_a + (\boldsymbol{\Phi}_{a,m}^{\dagger})^T\boldsymbol{\Phi}_{n,m}^T\boldsymbol{K}_{n,n}\boldsymbol{\Phi}_{n,m}\boldsymbol{\Phi}_{a,m}^{\dagger}\boldsymbol{x}_a = (\boldsymbol{\Phi}_{a,m}^{\dagger})^T\boldsymbol{\Phi}_{n,m}^T\boldsymbol{f} . \tag{3.7}$$

If the mass normalised modes are used, then SEREP reduced TAM mass matrix is given by:

$$\boldsymbol{M}_{a,a}^{TAM} = (\boldsymbol{\Phi}_{a,m}^{\dagger})^T\boldsymbol{\Phi}_{a,m}^{\dagger} . \tag{3.8}$$

3.3 Sensitivity of the Test Analysis Model

3.3.1 Finite Element Model

FEMs of three different spacecraft were considered for the test analysis correlations. The surface models of these spacecraft are shown in Fig. 3.1. The first FEM consists of 7153 nodes and 6962 elements and represents the structural model of a mini spacecraft having a mass of 75.7 kg. The modal analysis, performed using NASTRAN [94] showed sixteen normal modes below 150 Hz in the base fixed boundary condition simulating the launch configuration. Surrey Satellite Technology Limited (SSTL), UK, developed the second spacecraft model. It consists of 121285 nodes and 81795 elements with a mass of 300 kg. There were 24 normal modes in the base fixed condition with frequencies less than 150 Hz. The third spacecraft model was developed by EADS Astrium Limited, UK for their AEOLUS spacecraft. This model consists of 95980 nodes and 109295 elements. The normal mode analysis in the base fixed boundary condition showed that there were 295 modes having frequencies less than 150 Hz. The spacecraft has a total mass of 1800 kg. The number of nodes and elements in each FEM depend on the type of elements used in that model. These FEMs are chosen in such a way that

different classes of spacecraft are covered in this study. Figure 3.1 also shows the relative sizes of different spacecraft considered here.

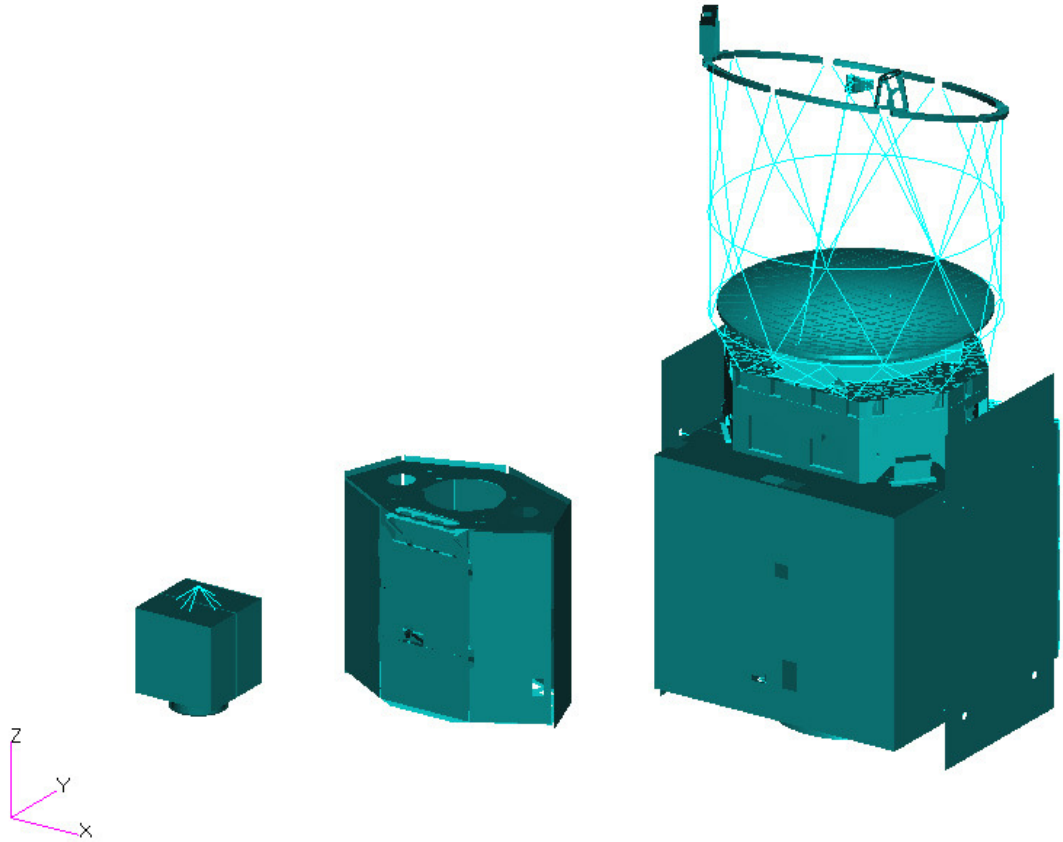

a) Mini spacecraft **b) Medium size spacecraft (SSTL, UK)** **c) Large spacecraft (EADS Astrium Limited)**

Fig. 3.1 Three spacecraft structure models.

3.3.2 Target Mode Selection

The common target modes selection criteria were applied to all of the spacecraft. The target modes for the correlation studies were chosen based on the effective mass of the modes, modal kinetic energy and modal strain energy [95]. For the test analysis correlation, modes up to 150 Hz were considered in this study. All the modes with an effective mass greater than or equal to 2% of the total mass of the spacecraft and fall within the specified frequency were chosen as target modes. In addition, modes with 50% or more modal strain energy or modal kinetic energy of the total system and within a frequency of 150 Hz were also selected as target modes. This ensures that the local modes,

which give peak responses in the subsystems, are also included in the correlation process.

3.3.3 Monte Carlo Simulation

The accuracy of the modal parameters extracted from the dynamic test depends on several factors such as the amount of noise in the measurements, accuracy of the instruments and the test set up etc. This leads to some inaccuracy in the estimation of the modal parameters and the nature of these inaccuracies are complicated. FEM results also contain some inaccuracies compared to the actual system performance mainly due to the assumptions in the idealization of the structure and limitation in the simulation of the real loading conditions. Simplified methods were used to simulate these inaccuracies and to generate the synthetic test data by different researchers [26, 40]. In this work, a simplified multiplicative error model is used to represent the experimental and FE inaccuracies. It is defined by the equation:

$$\boldsymbol{E} = \left(\boldsymbol{J} + \frac{P}{100}(-\boldsymbol{J} + 2\boldsymbol{R}) \right) \tag{3.9}$$

where $\boldsymbol{J}$ is a unit square matrix with dimension equal to the number of DOF, P is the percentage of inaccuracy, $\boldsymbol{R}$ is a square array of uniformly distributed random numbers on the open interval (0, 1) with the same dimensions as $\boldsymbol{J}$. Each column of $\boldsymbol{E}$ gives a random vector and the arithmetic mean of each element in the vector computed using a large number (e.g. 1000) of such vectors would be very close to 1.0.

This error model ensures that mode shapes are altered in both the directions and permits the accurate control of inaccuracy in the model than the Gaussian distribution. Although this model is simplified, it is sufficient for the Monte Carlo simulation to assess the sensitivity of the modal reduction method to the different case of inaccuracies and have good similarity with the mode shapes obtained from the erroneous FEMs described in Chapter 4. The modes obtained from the FEM, $\boldsymbol{\Phi}$, are used to generate the synthetic experimental modes, $\boldsymbol{\psi}^E$ [39, 40]. These synthetic modes are obtained by the Hadamard

product (element-by-element matrix multiplication) of $\boldsymbol{\Phi}$ and inaccuracy, $\boldsymbol{E}_1$ as:

$$\boldsymbol{\Psi}^E = \boldsymbol{\Phi} \otimes \boldsymbol{E}_1 . \tag{3.10}$$

Here, $\boldsymbol{E}_1$ was calculated using Eq. (3.9). Similarly, the noise affected FE modes, $\boldsymbol{\Phi}^E$ were computed using $\boldsymbol{\Phi}$ and inaccuracy, $\boldsymbol{E}_2$(generated using different random numbers), is given by:

$$\boldsymbol{\Phi}^E = \boldsymbol{\Phi} \otimes \boldsymbol{E}_2 . \tag{3.11}$$

The first mode shape of Spacecraft 3 obtained from the FE analysis is shown in Fig. 3.2. This is a lateral mode in the *X* direction. The dotted lines in this figure show the un-deformed structure. This analytical mode shape is determined using 33 tri- axial accelerometers and hence each mode shape will have only 99 components or DOF. These 33 sensor locations on Spacecraft 3 are shown in Fig. 3.3 using two different views of the structure for the clarity of representation. The first nominal mode of Spacecraft 3 and the corresponding distorted mode shape with 25% of inaccuracy are illustrated in Fig 3.4. It can be observed that, this mode is predominant in the *X* direction and hence the amplitude is predominant for the degrees of freedom corresponding to 1, 4, 7, …, 97. The SEREP mass matrix calculated using these types of modes would have 99 rows and columns irrespective of the number of modes used.

The NCO check [91] (also known as weighted MAC [1]) is then performed using the equation as:

$$\boldsymbol{NCO} = \frac{\left|\boldsymbol{\Psi}^T \boldsymbol{M}_{SEREP} \boldsymbol{\Phi}\right|^2}{(\boldsymbol{\Psi}^T \boldsymbol{M}_{SEREP} \boldsymbol{\Psi})(\boldsymbol{\Phi}^T \boldsymbol{M}_{SEREP} \boldsymbol{\Phi})} \ . \tag{3.12}$$

Here, different levels of inaccuracies were considered in $\boldsymbol{\Phi}$ and $\boldsymbol{\psi}$ either together or independently, depending on the assumption of error, for the computation of the NCO. The NCO measures the correlation between the analytically predicted mode shapes and the mode shapes determined from the dynamic test. This enhanced version of MAC uses a mass weighting matrix and hence includes the mass distribution in the correlation process in order to give

more weighting to the DOFs with more mass associated with them [1]. The off diagonal terms in the NCO matrix helps to identify whether the comparison is between the same or different mode pairs. Agencies such as the National Aeronautics and Space Administration (NASA) [20] and the European Space Agency (ESA) [21] specify the test analysis correlation requirements. For example, the correlation is considered to be successful if all the diagonal terms in the cross orthogonality matrix are greater than 0.9 and all other values in the matrix are less than 0.1.

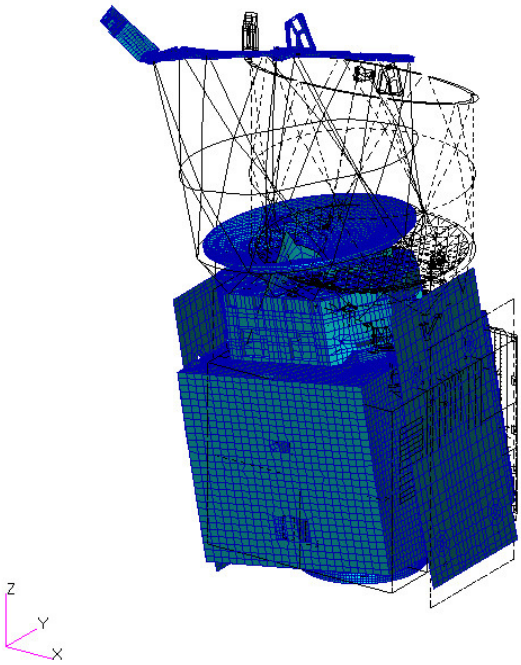

Fig. 3.2 The first mode shape of Spacecraft 3 at 15.96 Hz.

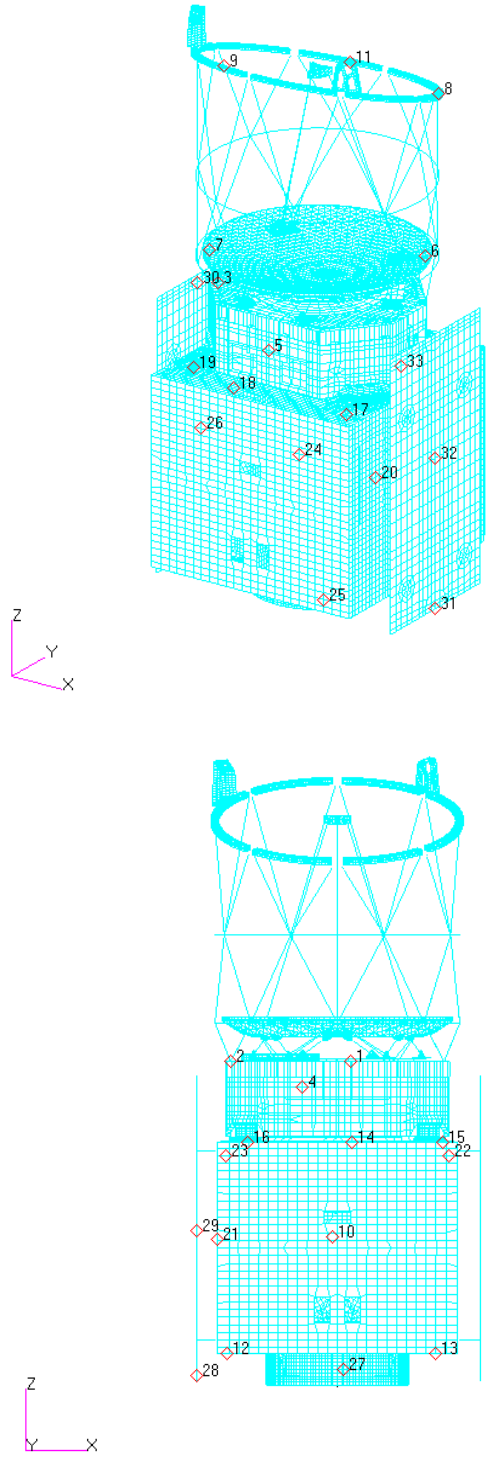

Fig. 3.3 Sensor locations on Spacecraft 3.

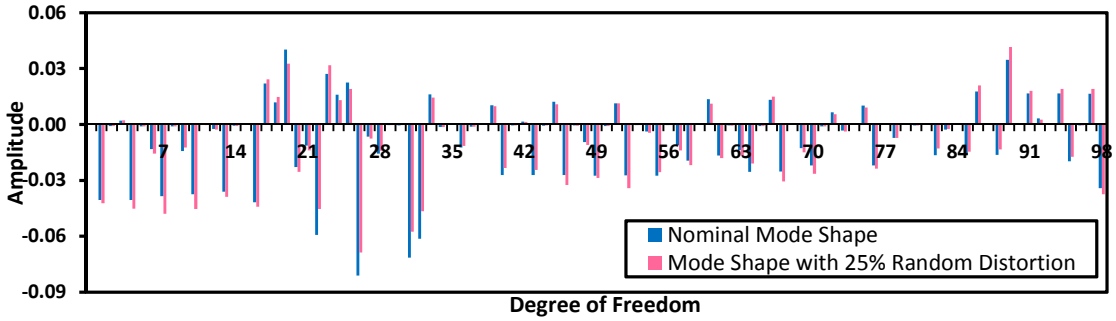

Fig. 3.4 Coefficients of nominal and erroneous mode shapes determined using 33 tri-axial sensors.

3.4 Results and Discussion

3.4.1 The Effect of the Number of Modes in SEREP on the Normalised Cross Orthogonality Check

In this study, the NCO check was performed using the SEREP reduced model of different spacecraft structures to assess the robustness of SEREP based TAM on the different type of inaccuracies. Three cases were considered for each spacecraft model. In the first case, only experimental modes were assumed to be inaccurate, whereas in the second case FE modes were considered as inaccurate. In the third case, both experimental and FE modes were simulated with same percentage of inaccuracies although different random vectors were used for the generation of error. The percentage of inaccuracy was varied from 0.01 to 25% for each case and Monte Carlo simulations were used to compute the probability of meeting the NCO criterion based on 1000 computational results per each level of inaccuracy. Here consistently with NASA or ESA requirements, the correlation is considered to be successful if all the diagonal terms in the cross orthogonality matrix are greater than 0.9 and all other values in the matrix are less than 0.1. Based on this criterion, the probability to meet the NCO check for different spacecraft is shown in Tables 3.1- 3.3.

The target modes for each spacecraft were chosen based on the method described as in the section 3.3.2. As per this criterion, the Number of Target Modes (NTM) were found to be 11 for Spacecraft 1 and 12 for Spacecraft 2 and

3. To correlate these target modes, 99 DOF that correspond to the sensor locations in vibration test were selected [39, 40]. Although Spacecraft 1 has only 11 target modes, the same number of sensor locations (99 DOF) is used for the comparison. From the results in the Tables 3.1– 3.3, it can be observed that for all the spacecraft models, as the Number of Modes in the Reduction (NMR) increase from the minimum required number, the probability of success of NCO check reduces. As the reduced modal matrix must contain the target mode shapes, the minimum number of modes to be used in SEREP is the number of target modes. However, it is possible to include further mode shapes as in the case of SEREPa. Here, the dimensions of the different parameters used for the computation of SEREP mass matrix are:

$$\boldsymbol{M}_{SEREP} = \left[[\boldsymbol{\Phi}_{DOF,NMR}^{T} \boldsymbol{\Phi}_{DOF,NMR}]^{-1} \boldsymbol{\Phi}_{DOF,NMR}^{T} \right]^{T} \left[[\boldsymbol{\Phi}_{DOF,NMR}^{T} \boldsymbol{\Phi}_{DOF,NMR}]^{-1} \boldsymbol{\Phi}_{DOF,NMR}^{T} \right]. \quad (3.13)$$

Table 3.1 Probability of NCO diagonal terms > 0.9 and off diagonal terms <0.1 for Spacecraft 1

NMR	Percentage of inaccuracy								Case (NTM=11)
	25	10	7.5	5	2.5	1	0.1	0.01	
11	67.5	100	→						Error in experimental modes
12	58.9	100	→						
20	0	25.7	60.4	94.7	100	→			
50			←	0	3.6	96.8	100	→	
99						←	0	90.6	
11	20.9	100	→						Error in FE modes
12	12.0	100	→						
20	0	2.6	34.3	92.1	100	→			
50			←	0	0.5	96.4	100	→	
99					←	0	0.4	91.1	
11	6.8	98.3	100	→					Error in both FE and experimental modes
12	2.1	98.3	100	→					
20	0	0.6	9.3	56.5	99.9	→			
50				←	0	66.8	100	→	
99						←	0	72.7	

As per this definition, $\boldsymbol{M}_{SEREP}$ is a square matrix irrespective of the number of modes used in the reduction and its dimension is always equal to the DOF or sensor locations. For the calculation of $\boldsymbol{M}_{SEREP}$ for Case 1 in Table 3.1, nominal or 'true' FE modes ($\boldsymbol{\Phi}$) were used while noise affected FE modes, $\boldsymbol{\Phi}^{E}$ were used for the estimation of $\boldsymbol{M}_{SEREP}$ for Cases 2 and 3. When the NMR is greater than the NTM, more modes are used for the computation of the $\boldsymbol{M}_{SEREP}$ than the minimum requirement. Such cases lead to a reduction in the probability of passing the NCO check performed by using the reduced mass matrix due to the decrease in the diagonal values and increase in the off diagonal values of the cross orthogonality matrix. The minimum number of modes required to be incorporated in the reduction are the target modes whereas the maximum number of modes considered here is equal to the number of DOFs.

Table 3.2 Probability of NCO diagonal terms > 0.9 and off diagonal terms <0.1 for Spacecraft 2

NMR	Percentage of inaccuracy								Case (NTM=12)
	25	10	7.5	5	2.5	1	0.1	0.01	
12	0.6	83.7	99.2	100	→				Error in experimental modes
20	0	0.4	3.7	34.2	96.6	100	→		
50					←	0	100	→	
99							←	0	
12	0	23.4	76.8	99.6	100	→			Error in FE modes
20		←	0	0.4	22.9	100	→		
50					←	0	91.4	100	
99							←	0	
12	0	9.0	44.4	96.2	100	→			Error in both FE and experimental modes
20		←	0	0.1	18.1	99.9	100	→	
50					←	0	74.2	100	
99							←	0	

Tables 3.1– 3.3, also show that the inaccuracies in the FE modes have more probability of failing the NCO check than the inaccuracies in the experimental

modes alone. Referring to Eq. (3.13), the TAM mass matrix is calculated using the FE mode shapes and hence error in the FE modes will reflect in $\boldsymbol{M}_{SEREP}$ but it will be nominal when inaccuracy is present only in the experimental modes. When FE modes are corrupted, NCO check is calculated by replacing $\boldsymbol{\Phi}$ with $\boldsymbol{\Phi}^{E}$ in the Eq. (3.12). The combined effect of $\boldsymbol{M}_{SEREP}$ and $\boldsymbol{\Phi}^{E}$ which are inaccurate due to uncorrelated and different random numbers, result in a decrease in the probability to meet the correlation criterion. When both the FE and the experimental modes contain inaccuracies, the probability to pass NCO check will be further reduced due to the error in all the terms in the right hand side of Eq. (3.12). This is shown in Fig. 3.5 by extracting the required results (NMR = 12, 20, 50, and 99) from Tables 3.1– 3.3 for a better representation of the results.

Table 3.3 Probability of NCO diagonal terms > 0.9 and off diagonal terms <0.1 for Spacecraft 3

NMR	Percentage of inaccuracy								Case (NTM=12)
	25	10	7.5	5	2.5	1	0.1	0.01	
12	0	9.4	34.7	84.7	100	→			Error in experimental modes
20					←	0	39.9	100	
50						←	0	0.2	
99							←	0	
12	0	2.5	21.7	71.7	100	→			Error in FE modes
20					←	0	38.7	100	
50						←	0	0.1	
99							←	0	
12	0	3.1	11.8	42.6	96.0	100	→		Error in both FE and experimental modes
20					←	0	3.6	100	
50							←	0	
99							←	0	

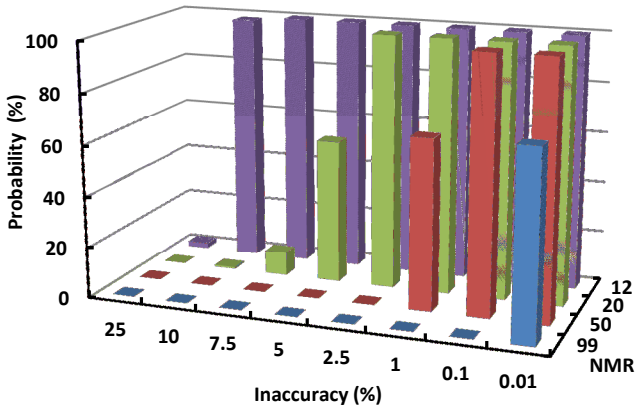

a) Spacecraft 1

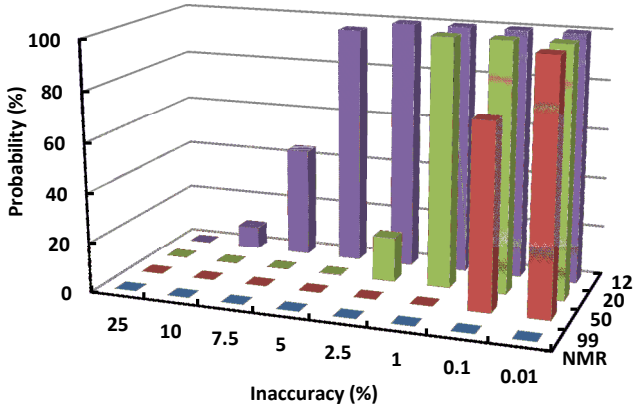

b) Spacecraft 2

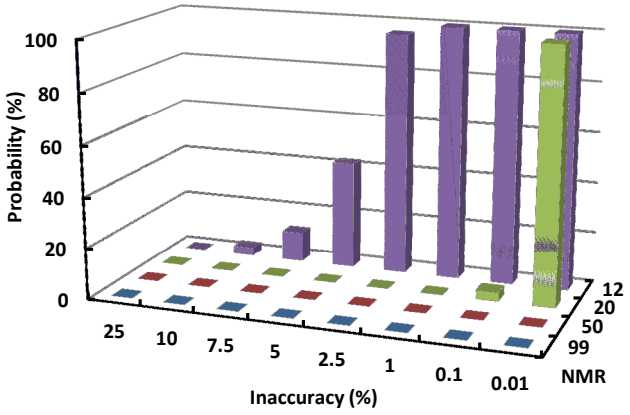

c) Spacecraft 3

Fig. 3.5 Probability of NCO check success when inaccuracies are present in both FE and experimental modes.

When the number of modes used in the reduction is equal to the number of sensor locations, even a very low percentage (0.1) of error leads to failure in the NCO. This is unreasonable, as in practice for such small differences between test and analysis modes one would expect to pass the NCO. This type of reduction known as SEREPa and its probability to meet the NCO check is shown in the last row of each case in the Tables 3.1- 3.3. The SEREPa reduction is computationally efficient as it can avoid a pseudo inverse due to its inherent square matrix property. However, its high sensitivity to inaccuracies prevents its practical use. Apart from the general features of the SEREP reduced model in the NCO, it can also be observed that Spacecraft 3 is the most vulnerable to any kind of inaccuracy while Spacecraft 1 is the least affected for this correlation criteria. The results also show that for all three spacecraft, the SEREP should be carried out with the minimum number of modes, as increasing the number of modes sharply reduces the probability of passing the NCO check even for small percentages of inaccuracy.

3.4.2 The Effect of the Number of Target Modes on the Normalised Cross Orthogonality Check

Table 3.4 shows the probability of meeting the NCO check when the number of target modes increased from 12 to 20 for Spacecraft 3. These results are reasonably obvious but presented here for completeness. As expected, in all the cases as the NTM increases, the probability of successfully meeting the NCO reduces compared to the fewer target modes case, due to the increased requirement of modes in the reduction and hence, more target modes need to be incorporated in the cross correlation. Here a minimum of 20 target modes are required to be incorporated in the reduction and these modes are required again in the NCO check, hence the probability of success is less than the values shown in Table 3.3. Similar results were obtained for the other spacecraft models, and hence their numerical values are not reported here.

Table 3.4 Probability of NCO diagonal terms > 0.9 and off diagonal terms <0.1 for Spacecraft 3 with NTM=20

NMR	Percentage of inaccuracy								Case
	25	10	7.5	5	2.5	1	0.1	0.01	
20					←	0	8.4	100	Error in experimental modes
50						←	0	0.2	
99							←	0	
20					←	0	8.1	100	Error in FE modes
50						←	0	0.1	
99							←	0	
20					←	0	0.4	100	Error in both FE and experimental modes
50							←	0	
99							←	0	

3.4.3 The Effect of Independence between the Target Modes

For all the spacecraft considered in these correlation studies, irrespective of percentage of inaccuracies in the mode shapes, NTM and NMR play a significant role in the NCO check. It is evident that if NTM=NMR then this results in the highest probability to pass the NCO. Once the target modes are selected based on the specified criteria, apart from the number of target modes and NMR, it was observed that independence between the target modes affect the correlation process. The effective independence matrix between the targets modes was computed for all the inaccuracy levels using the equation [96]:

$$\boldsymbol{EFI}_{DOF,DOF} = \boldsymbol{\Phi}\left[\boldsymbol{\Phi}^T\boldsymbol{\Phi}\right]^{-1}\boldsymbol{\Phi}^T . \tag{3.14}$$

Each term in the diagonal of this matrix indicates the fractional contribution of each sensor location to the independence of the target modes. The smallest value in the diagonal of the EFI matrix corresponds to the most dependent DOF. To compare the target modes of different spacecraft, the standard deviations of the corresponding diagonal values of EFI matrix were computed.

Table 3.5 shows the characteristics of different spacecraft based on the EFI of their target modes. The table also includes the characteristics of a synthetic modal matrix generated using random numbers in order to obtain highly uncorrelated modes. This synthetic modal matrix contained 99 modes and 99 DOF. It indicates that target modes of Spacecraft 3 have the highest variation in the fractional components of modes compared to the other spacecraft models. The results shown in Tables 3.1– 3.3 prove that, Spacecraft 3 has the least probability to succeed the NCO check, while Spacecraft 1 has the highest probability for a particular percentage of error. Hence, it can be inferred that, as the standard deviation of the diagonal terms of the EFI matrix increases, there will be less probability of passing the NCO check. This is also valid in the case of synthetic modes. Table 3.6 shows the NCO check results for the synthetic modes and highlights that even with 25% error in mode shapes the NCO check can be passed for NMR=12. Here, the number of target mode was taken as 12. These synthetic modes have a much higher probability of success than any other spacecraft structures. It can also be noted that, standard deviation of the diagonal terms of the EFI matrix generated using 12 synthetic target modes is lower than any other spacecraft structure due to the uncorrelated synthetic modes.

Table 3.5 Standard deviation of the EFI of the target modes

Structure	Standard deviation
Synthetic	0.04
Spacecraft 1	0.13
Spacecraft 2	0.14
Spacecraft 3	0.16

Table 3.6 Probability of NCO diagonal terms > 0.9 and off diagonal terms <0.1 for synthetic modes

NMR	Percentage of inaccuracy								Case (NTM=12)
	25	10	7.5	5	2.5	1	0.1	0.01	
12	100	→							Error in experimental modes
20	100	→							
50	100	→							
99				←	0	1.1	100	→	
12	100	→							Error in FE modes
20	100	→							
50	100	→							
99				←	0	2.7	100	→	
12	100	→							Error in both FE and experimental modes
20	100	→							
50	99.4	100	→						
99				←	0	0.1	100	→	

3.4.4 The Effect of Inaccuracy in Modal Parameters on the Frequency Response Function

The validation of FEMs is conducted by comparing/correlating some model parameters such as resonance frequencies and mode shapes with the experimentally retrieved parameters. This correlation exercise can be relatively sophisticated and requires a TAM, which can be obtained as previously described. However, what is ultimately important is the capability of the FEM to predict the dynamic response of the structure, e.g. the frequency response functions describing the loads in structural elements where the margins are particularly low. Hence, an accurate prediction of the frequency response using FEM is necessary for the design of the spacecraft structure. In this section, the inaccuracies in the frequency response functions of the different spacecraft are considered to investigate the relationship between achieving success in the NCO check and the capability to predict the dynamic response accurately.

Referring to Tables 3.1- 3.2, Spacecraft 1 can easily pass the NCO check compared to Spacecraft 2. In the case of Spacecraft 1, even with an inaccuracy of 10% in both FE and experimental modes, there is a probability of 98.3 % to pass the NCO check whereas Spacecraft 2 has only a 9.0 % probability to clear the check when the NMR=NTM. These two spacecraft models were used to analyse their displacement frequency response functions when modal parameters are corrupted with inaccuracies.

Mode shapes can be used to compute the displacement based frequency response function or receptance using the equation [97],

$$\boldsymbol{H}_{pq}(\Omega)=\sum_{k=1}^{r}\frac{\boldsymbol{\Phi}_{kp}\boldsymbol{\Phi}_{kq}}{\omega_k^2 - \Omega^2 + 2i\Omega\zeta_k\omega_k} \tag{3.15}$$

where $\boldsymbol{\Phi}_{kp}$ is the value of the *k*th mode at the *p*th output location, $\boldsymbol{\Phi}_{kq}$ is the value of the *k*th mode at the *q*th input location, ω_k is the undamped natural frequency of the *k*th mode in rad/sec, $i=\sqrt{-1}$, Ω is the excitation frequency in rad/sec, ζ_k is the modal damping coefficient, and *r* is the number of modes used for the response computation. To maintain the accuracy of the FRF, all modes in the required frequency band and sufficient modes in the lower and upper bands need to be included in the computation of $H_{pq}(\Omega)$ [26]. In this study, all the modes from 0-300 Hz were included to calculate the FRF in the frequency band of 5-150 Hz using a Matlab [98] program and obtained a very good comparison with MSC Nastran [94] results.

Modal based displacement frequency responses at five different locations of Spacecraft 1 and 2 for a unit excitation force in *Z* direction were computed using Eq. (3.15). Figure 3.6 shows the response and input locations in both the spacecraft models. It was assumed that frequency and mode shape were corrupted with 5% inaccuracies and a modal damping of 2%. Maximum and minimum responses for each frequency step of 0.1 Hz were computed for the required frequency band of 5.0-150.0 Hz. The average values of maximum (Max) and minimum (Min) response were computed based on 1000 analyses for each frequency step to get a statistical representation of the actual process. The real part of the frequency response function, Real (H) for the different locations of Spacecraft 1 along with the nominal modal displacement response

function is shown in Fig. 3.7. The nominal responses are calculated using the uncorrupted modal parameters along with 2% modal damping. Figure 3.8 shows the frequency response function of Spacecraft 2 for five different locations for a unit force at the input location. Modal damping and error considered in modal parameters were same as in the case of Spacecraft 1.

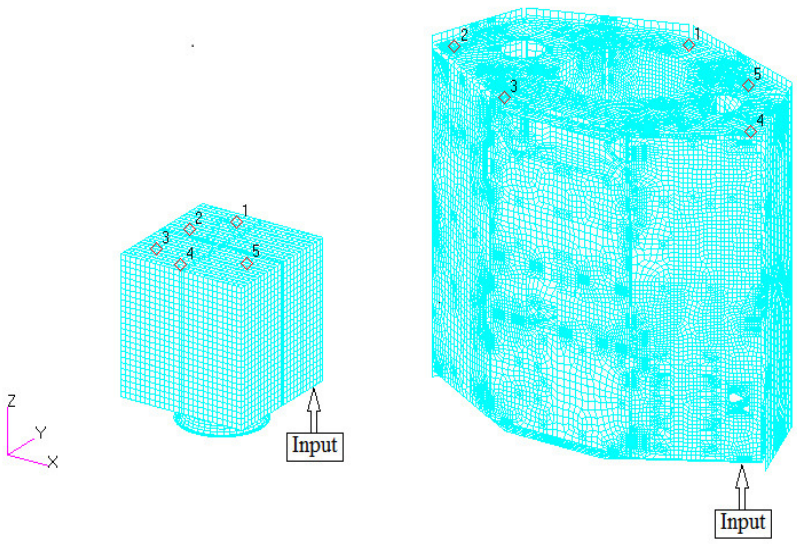

a) Spacecraft 1 **b) Spacecraft 2**

Fig. 3.6 Input and the response locations.

Tables 3.7-3.8 show the maximum and minimum responses in the frequency band (5-150 Hz) based on an average result of 1000 analysis observed at five different locations of two spacecraft calculated using clean and the noisy modal parameters. Spacecraft 1 has considerably larger deviation in peak response. There is a maximum of 51.06% deviation in peak response when the modal parameters are corrupted with 5% error in comparison with nominal response.

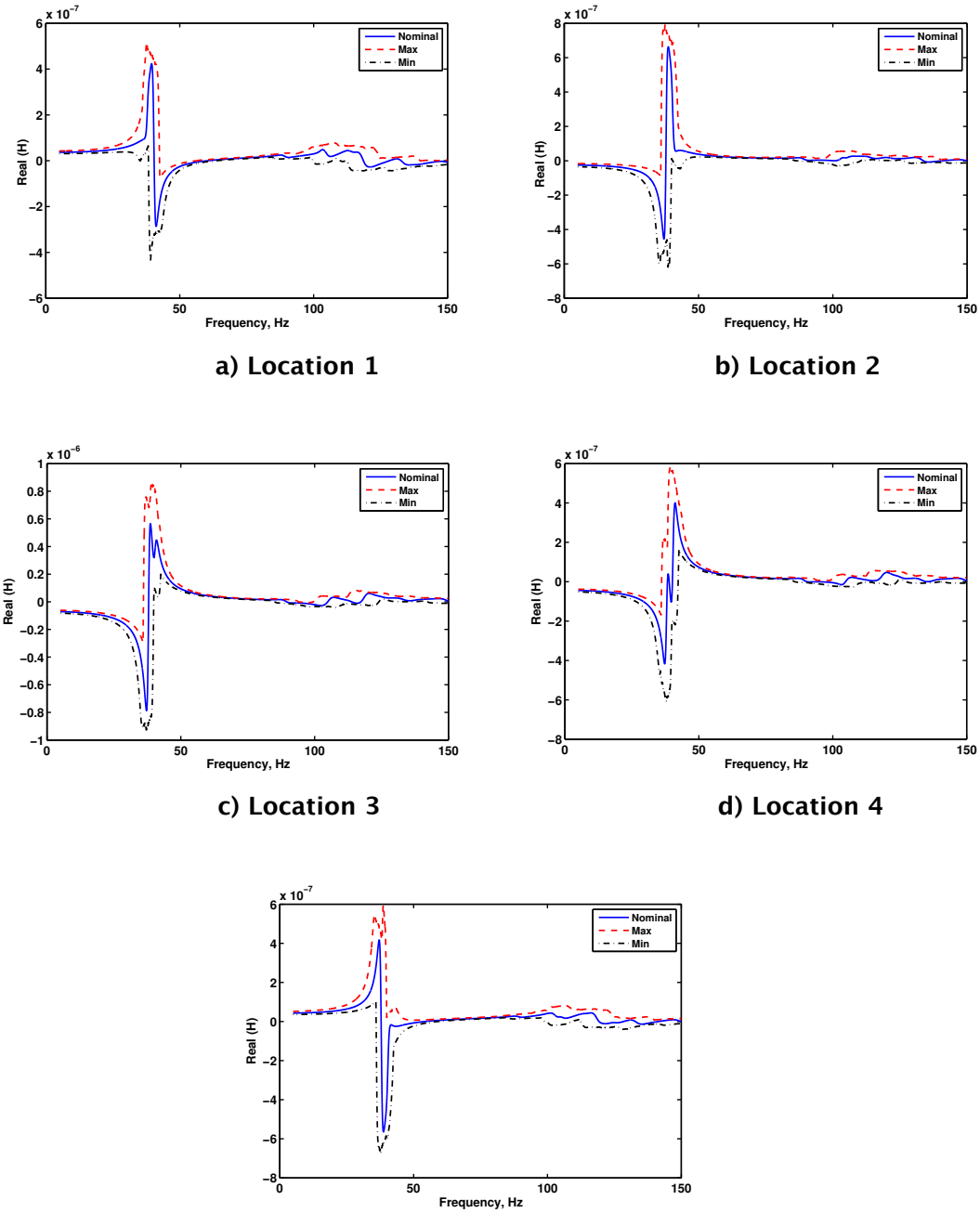

a) Location 1 **b) Location 2**

c) Location 3 **d) Location 4**

e) Location 5

Fig. 3.7 Frequency responses of Spacecraft 1.

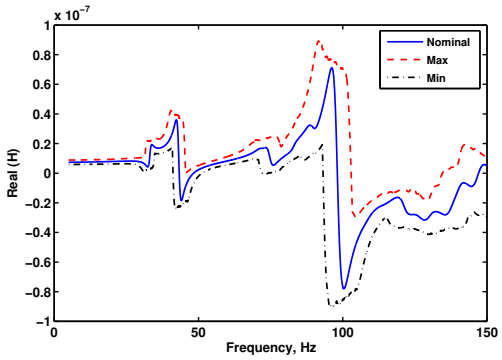

a) Location 1

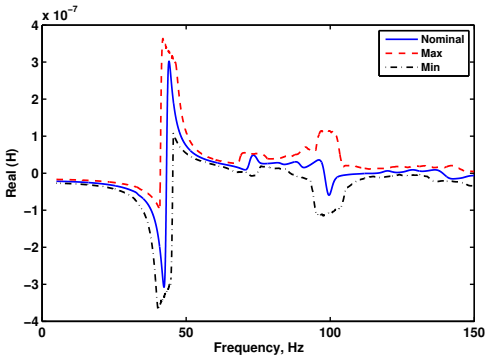

b) Location 2

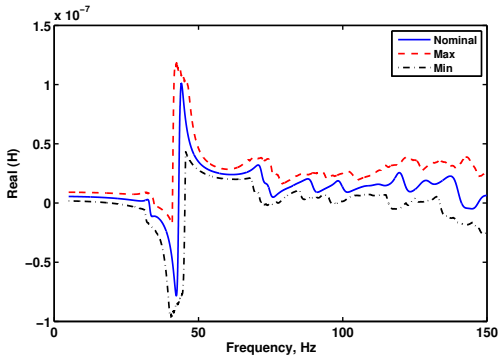

c) Location 3

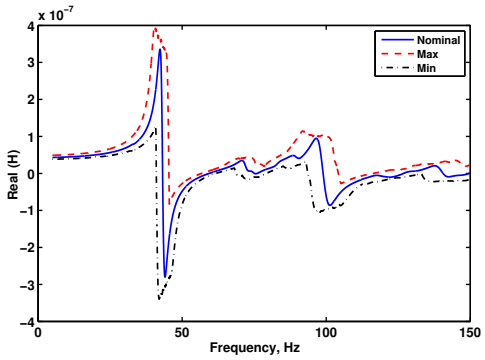

d) Location 4

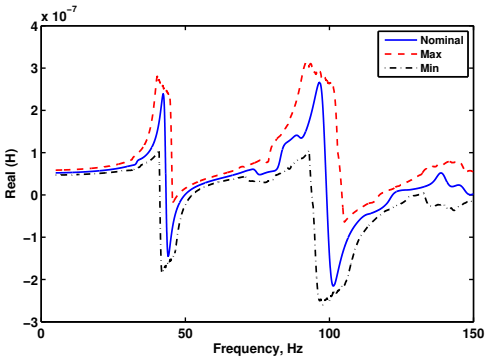

e) Location 5

Fig. 3.8 Frequency responses of Spacecraft 2.

The estimation of the minimum response also shows a change up to 51.4%. Spacecraft 2 shows a maximum deviation of only 25.42% in the peak frequency response and the maximum of 23.05% deviation in the minimum response. The average change in peak response for Spacecraft 1 is 36.25% whereas Spacecraft 2 has an average deviation of only 19.79%. The average change in the minimum response for Spacecraft 1 is 33.87% but spacecraft-2 has an average change of only 20.25%. The previous results show that Spacecraft 2 is more vulnerable to inaccuracies. The results also found that spacecraft-2 had more difficulty in passing the NCO check compared to Spacecraft 1, but it is more robust in the prediction of frequency response when frequency and mode shapes were contaminated with random inaccuracies. Hence, the ability to pass the NCO check does not necessarily imply an accurate capability to predict the response.

Table 3.7 The maximum frequency response

Structure	Location	Peak response in the frequency range, Real (H)			
		Nominal modes	Inaccurate frequency and modes	Change (%)	Average change (%)
Spacecraft 1	1	4.24×10^{-7}	5.17×10^{-7}	21.93	36.25
	2	6.63×10^{-7}	7.95×10^{-7}	19.91	
	3	5.66×10^{-7}	8.55×10^{-7}	51.06	
	4	4.00×10^{-7}	5.84×10^{-7}	46.00	
	5	4.18×10^{-7}	5.95×10^{-7}	42.34	
Spacecraft 2	1	7.12×10^{-8}	8.93×10^{-8}	25.42	19.79
	2	3.02×10^{-7}	3.64×10^{-7}	20.53	
	3	1.01×10^{-7}	1.18×10^{-7}	16.83	
	4	3.36×10^{-7}	3.97×10^{-7}	18.15	
	5	2.66×10^{-7}	3.14×10^{-7}	18.04	

Table 3.8 The minimum frequency response

Structure	Location	Minimum response in the frequency range, Real (H)			
		Nominal modes	Inaccurate frequency and modes	Change (%)	Average change (%)
Spacecraft 1	1	-2.86×10^{-7}	-4.33×10^{-7}	51.40	33.87
	2	-4.56×10^{-7}	-6.19×10^{-7}	35.75	
	3	-7.86×10^{-7}	-9.28×10^{-7}	18.07	
	4	-4.17×10^{-7}	-6.06×10^{-7}	45.32	
	5	-5.64×10^{-7}	-6.70×10^{-7}	18.79	
Spacecraft 2	1	-7.79×10^{-8}	-9.11×10^{-8}	16.94	20.25
	2	-3.08×10^{-7}	-3.69×10^{-7}	19.80	
	3	-7.85×10^{-8}	-9.66×10^{-8}	23.05	
	4	-2.80×10^{-7}	-3.39×10^{-7}	21.07	
	5	-2.16×10^{-7}	-2.60×10^{-7}	20.37	

3.4.5 Selection of Optimum Sensor Locations Using SEREP

The selection of sensor locations from the available locations or DOFs can help to meet quality criteria such as the NCO [40]. Effective Independence matrix is a proven technique to select the optimum sensor locations. This is carried out by calculating the EFI of the modes using Eq. (3.14) and eliminating the sensor locations corresponding to the least element in the diagonal of the EFI-matrix. After eliminating the particular DOF, EFI have to be re-computed and the procedure continued until the required number of sensor locations are obtained [39]. As per Eq. (3.13), the SEREP reduced mass matrix, $\boldsymbol{M}_{SEREP}$ has a significant role in meeting the NCO criteria and in turn, is calculated using the mode shapes obtained from different sensor locations. Hence, $\boldsymbol{M}_{SEREP}$ is dependent on the sensor locations. Using this property, the SEREP mass matrix is employed to determine the optimum sensor locations as in the case of the EFI. The sensor location is iteratively removed for the location that corresponds

to the least value in the diagonal of the $\boldsymbol{M}_{SEREP}$ matrix. Then the $\boldsymbol{M}_{SEREP}$ matrix is re-computed using the new sensor locations and the procedure is continued until the required number of sensor locations is reached as illustrated in Fig. 3.9.

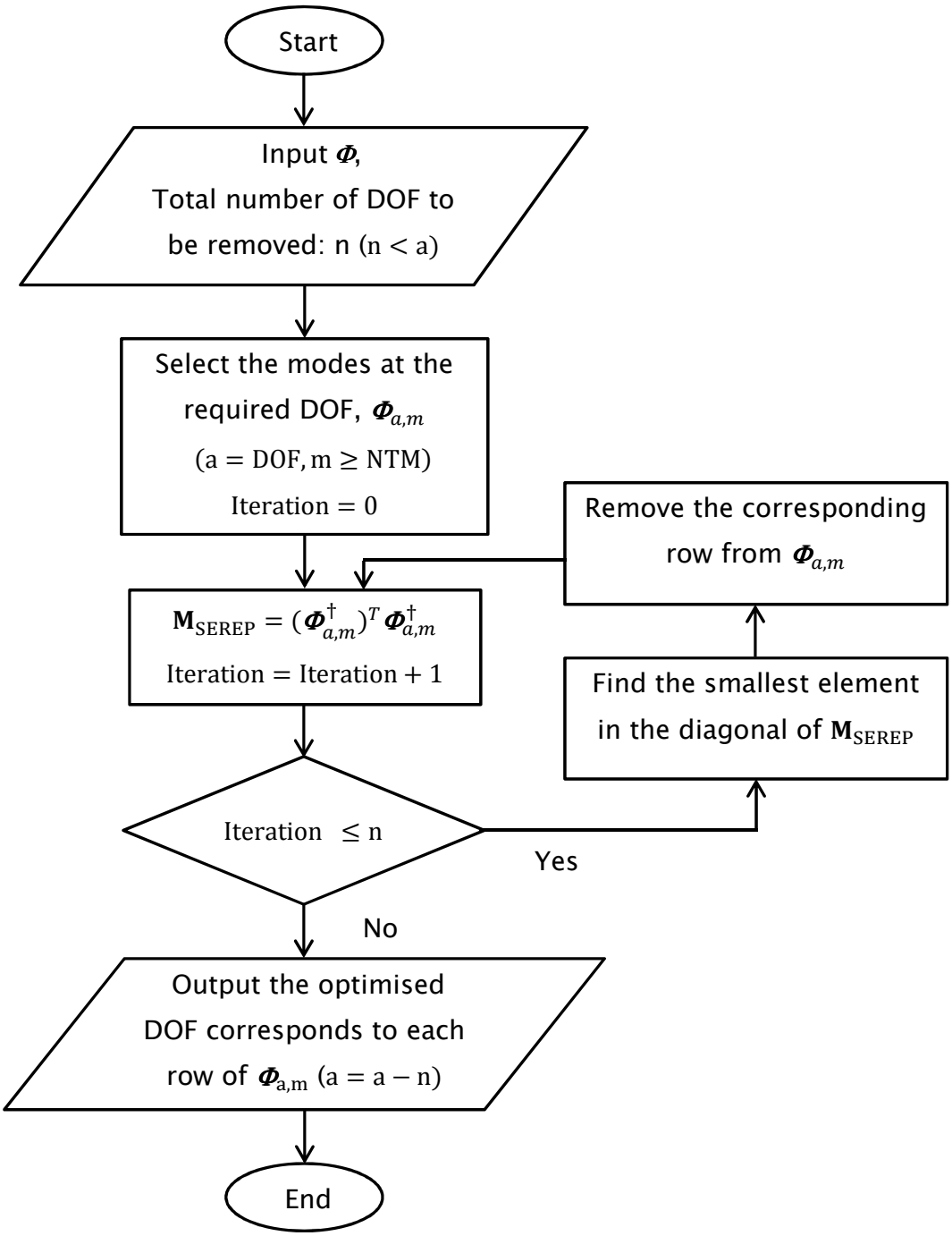

Fig. 3.9 Flowchart for sensor location optimisation.

A similar flowchart as shown in Fig. 3.9, can also be used for the EFI based optimisation by calculating the EFI matrix instead of $\boldsymbol{M}_{SEREP}$. The method is applied to optimise the sensor locations of a cantilever and a spacecraft model as explained in the following section. A cantilever model is chosen due to its simplicity and to show that optimised locations are practically feasible. In the second example, using Spacecraft 2 FEM it is shown that by using Monte Carlo simulations, the SEREP based procedure yields better result than the EFI based optimisation.

3.4.5.1 Sensor Optimisation of the Cantilever Structure

The cantilever model considered in this study is shown in Fig. 3.10. It is assumed that there are 20 uni-axial accelerometer locations available to identify the first two modes in the *Y* direction. The structure considered has a rectangular cross section having 15×10^{-3} m width in *Z* direction and 2×10^{-3} m thickness in *Y* direction along with 0.3 m length. The aluminium material properties (Young's modulus = 68.9 G Pa, Poisons ratio=0.3, and density 2740.0 kg/m^3) [83] were used to generate the FEM. The first and the second modes have a natural frequency of 17.98 Hz and 112.34 Hz respectively. The closely spaced accelerometer locations are chosen to show that, the SEREP based optimisation avoids the nodal points of the modes considered in the SEREP. In this case, the second node of mode 2 is in between 15 and 16th accelerometer locations.

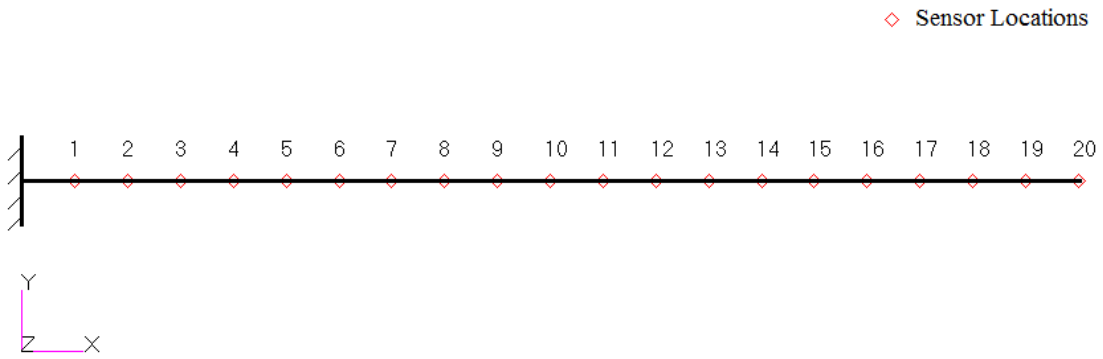

Fig. 3.10 Sensor locations on the cantilever.

To choose the 10 optimum sensor locations out of the 20 available sensors, an optimisation is performed using the SEREP mass matrix. Here, only the target modes were used in the computation of $\boldsymbol{M}_{SEREP}$. The diagonal terms in the SEREP mass matrix, when 5% inaccuracies are present in both the experimental and FE modes, are shown in the Table 3.9.

Table 3.9 Diagonal values of SEREP matrix

Sensor location	Diagonal value of $\boldsymbol{M}_{SEREP}$ (x10^{-3})
1	0.0001
2	0.0020
3	0.0075
4	0.0198
5	0.0407
6	0.0676
7	0.0876
8	0.1173
9	0.1431
10	0.1405
11	0.1502
12	0.1391
13	0.1213
14	0.1089
15	0.1083
16	0.1059
17	0.1299
18	0.1643
19	0.2442
20	0.3565

It can be noticed that, the least value of the SEREP diagonal values exist near the fixed end of the cantilever (sensor location 1), and the maximum is at the free end (sensor location 20). Hence, as per the optimisation procedure, the location 1 will remove first and $\boldsymbol{M}_{SEREP}$ will be re-computed after eliminating the corresponding row from both the nominal and FE modal matrices. It is worth mentioning that near the second node point of mode 2 (location 15 and 16), compared to the nearby locations, the value of SEREP diagonal is lower. The 10 sensor locations obtained after the optimisation procedure is shown in the Fig. 3.11. The result clearly shows that the nodes of vibration of the first two modes considered are automatically removed in the procedure and the optimised locations are practically feasible.

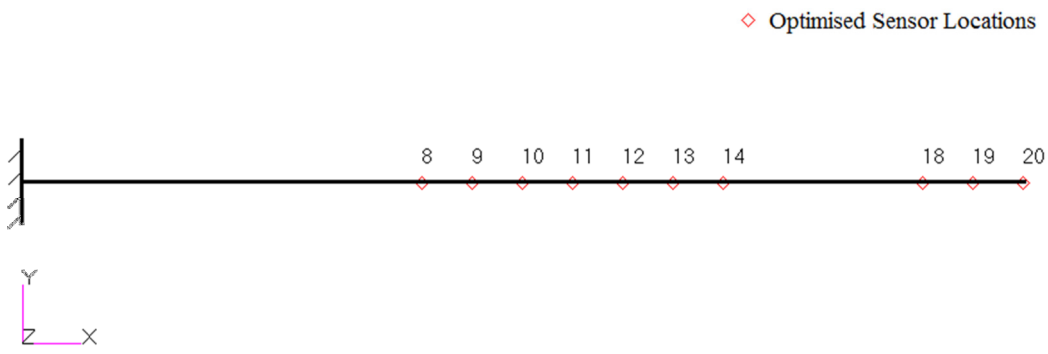

Fig. 3.11 Optimised sensor locations.

3.4.5.2 Sensor Optimisation of the Spacecraft Structure

In the previous analysis of Spacecraft 2, there were 99 DOF used for the determination of 12 target modes. To select the 50 optimum sensor locations from the available 99 DOF for the determination 12 target modes, the selection of the sensor location was performed for different cases using three different methods and the obtained results are shown in Table 3.10. In the first method, 50 sensor locations were randomly selected from 99 locations whereas the second and third methods utilise the procedure illustrated in the flowchart (Fig. 3.9) with the EFI and the $\boldsymbol{M}_{SEREP}$ matrices respectively. There were 12 modes used in the computation of $\boldsymbol{M}_{SEREP}$. The probability of meeting the NCO

for different percentages of inaccuracy was computed after the selection of the optimum sensor locations achieved by performing 1000 trials of Monte Carlo simulation for each inaccuracy level. The optimisation was performed for three cases by considering different levels of inaccuracies in the experimental modes, FE modes, and in both the experimental and FE modes.

When sensor locations are randomly selected, even a 10% error in the experimental modes leads to a very low percentage (6.5) of passing the NCO criterion as shown in Table 3.10. If an optimisation algorithm is used to choose the location, it can boost the success percentage to 66% and 75.3% for EFI and SEREP based optimisation respectively. When the inaccuracy is present in the experimental mode shapes, both the optimisation procedures can give better result compared to the case when inaccuracy is present only in the FE modes since the FE error directly affects the computation of the EFI and $\boldsymbol{M}_{SEREP}$ matrices. Nevertheless, for all the cases of inaccuracies, both EFI and SEREP based sensor location optimisation leads to higher probability of meeting the NCO criteria but the SEREP based optimisation always yields better results than the EFI based optimisation. The sensor location optimisation for the other spacecraft models also indicated that the SEREP based optimisation is superior to the EFI based optimisation for meeting the NCO criteria.

Table 3.10 Optimisation of sensor location for Spacecraft 2

DOF selection	Percentage of inaccuracy								Case (NTM=12)
	25	10	7.5	5	2.5	1	0.1	0.01	
Random	0	6.5	29.1	72.5	100	→			Error in experimental modes
EFI	0	66.0	94.6	100	→				
SEREP	0.2	75.3	97.9	100	→				
Random	0	6.1	31.4	75.3	100	→			Error in FE modes
EFI	0	11.0	59.1	98.6	100	→			
SEREP	0	25.3	81.4	100	→				
Random	0	0.4	4.8	37.5	96.4	100	→		Error in both FE and experimental modes
EFI	0	3.4	30.4	86.2	100	→			
SEREP	0	9.1	42.5	94.2	100	→			

3.5 Summary

The robustness of SEREP based TAMs with respect to inaccuracies in experimental and analytical mode shapes has been investigated with the help of real spacecraft structure FEMs. As expected, it has been observed that as the number of modes used in reduction to calculate the TAM matrix increases, the probability of success of the NCO check decreases. The analyses of three different spacecraft structures show that for practical purposes the modes used in the SEREP reduction process should be only the target modes. The computational efficiency of SEREPa deteriorates the test analysis correlation to the extent that it leads to an unreasonable low probability of success even when a very low level of inaccuracy (0.1 %) is present. The probability of success of the NCO check depends not only on the amount of inaccuracy in the modes but also on the relationship between the target modes. As the standard deviation of the diagonal terms of the EFI matrix generated using the target modes increases, the probability of passing the NCO check reduces. It has been observed that highly uncorrelated synthetic target modes generated using the random numbers have the highest probability of meeting the normalised cross orthogonality requirement and their EFI-matrix diagonal has the least standard deviation compared to other spacecraft modes.

It was also shown with the help of real spacecraft FEMs that, although a spacecraft FEM may fail in the NCO check, it could still predict the displacement based FRF (which are proportional to stress and loads in structural members) with higher accuracy than the FEM that passes the NCO check. Hence, this type of modal verification criterion does not assure a certain level of capability of the FEM to predict the frequency response function. In addition, a SEREP based sensor location optimisation is proposed to identify the optimal sensor locations and it is found that the optimisation yields a better probability of passing the NCO check than the EFI based optimisation.

It is shown that, even if FEM fails in the NCO check, it is sometimes able to represent the displacement based FRF better than a model that passes the NCO. These analyses were performed using synthetic modal parameters. In the

next chapter, the dynamic characteristics under the base excitation of real spacecraft models, and the corresponding MAC and NCO will be evaluated to find the usefulness of these criteria under the base excitation using the nominal and intentionally erroneous FEMs.

Chapter 4.
Study of the Correlation Criteria for Base Excitation of Spacecraft Structures

4.1 Introduction

The normal mode and the base excitation analysis of spacecraft structures are generally carried out using a finite element model. In practice, the analytical predictions of the structural responses and natural frequencies of the spacecraft are experimentally verified by fixing the base of the structure to a shaker or slip table whilst dynamically exciting its base. A sine sweep input at the base is standard practice to test the structure. The base input can be a random or a transient input depending upon the type of load under which the response has to be evaluated. The structural responses and the resonance frequencies are measured using accelerometers mounted at several critical locations on the structure.

Analysis of base excitation problems can be effectively performed using the Craig-Bampton method [90] as it explicitly defines the boundary and some of the internal degrees of freedoms. The problem can be analysed using a FEM by applying a known acceleration to the boundary and calculating the responses at the desired locations in the structure. In the case of spacecraft structures, the boundary can be represented using a single location or a number of rigidly connected locations leading to a statically determinate system. The base motion of the spacecraft is decided based on the input derived from the couple load analysis performed using both the launch vehicle and the spacecraft models. The base excitation analysis can be performed for various inputs at the spacecraft interface with the launch vehicle to determine the dynamic response of the spacecraft and the force transmitted to the launch vehicle

(base force). The base shake analysis response data can also be directly used for updating the mass and the stiffness matrices of the FEM [37].

The experimentally determined natural frequencies of the structure can be directly compared with the analytical values of the modal frequencies. However, a mode shape comparison requires a correlation method such as a modal assurance criterion [6, 99], coordinate modal assurance criterion [28] or a NCO check [5] to assess the quality of the analytical mode shapes in comparison with the experimentally determined modes. The NCO correlation requires the reduction of the mass matrix to the measurement location using a technique such as Guyan reduction [16], Improved Reduced System [22], modal test analysis model [7], system equivalent reduction expansion process [8] or hybrid reduction [24]. Model reduction can also be performed using the frequency response which is particularly suitable when modal coupling and noise in the test data are a concern [26, 100].

Structural model correlation can also be performed by comparing the frequency response functions. The frequency response assurance criterion compares the frequency response function at each frequency determined from the spectral analysis with the corresponding analytical FRF at the same frequency [30]. The frequency domain assurance criterion [29], utilises the MAC approach to the FRF correlation and compares the two vectors, one from the experimental data and other from a corresponding analytical model. However, these direct comparisons of FRF fail to give a good correlation when there is a shift in the location of resonance frequencies between the experimentally determined and the analytically predicted frequencies, which are very common in complex structures such as a spacecraft. Hence, FRAC or FDAC have limited use without a proper FRF adjustment procedure such as stretching and/or shifting. In addition, it is often required to measure the frequency response at multiple locations on the spacecraft to verify the design margins and to assess the acceleration levels experienced on the payloads and the subsystems. Hence, comparing the frequency response at different locations to verify the finite element model is a daunting task. In most practical cases, the experimental data will be measured using a few hundred sensors

whereas the analytical model can easily have hundreds of thousands of degrees of freedom and hence call for a model reduction or expansion of experimental data to the analytical DOFs for the comparison [101]. This could also introduce additional errors in the correlation method.

It has been observed that the commonly employed FEM validation methods, MAC and NCO, fail to predict whether the analytical model can successfully model the frequency response or the force transmitted to the base within an acceptable margin [102]. Using a Monte Carlo simulation it was shown in the previous chapter that a model having higher NCO values does not always guaranty that its ability to compute the receptance FRF is better than a model with lower values of NCO [103]. In this chapter, a quantitative assessment of the effectiveness of the most commonly employed mode shape correlation methods (MAC and NCO) in the force response characteristics under base excitation of real spacecraft structure is performed. An analysis was carried out to compare the forced response characteristics under base excitation using different FEMs of the same spacecraft to understand the ability of the model to predict the response in relation to the corresponding correlation values calculated using MAC or NCO. In addition, the possibility of using these vector correlation methods as an indicator to represent the possible level of error in the forced response characteristics is studied. A relatively simple correlation method is introduced by computing the correlation between the nominal forces transmitted to the base with an analytically calculated base force. The effectiveness of this new criterion is validated using three spacecraft structural FEMs. In this study, it is assumed that, the modal characteristics of the spacecraft determined from the original/nominal finite element models were considered as the experimental or 'true' parameters.

4.2 Base Shake Analysis

Details of the base shake analysis are presented in the reference [104]. Young [105] explained in detail the base shake analysis using the Craig-Bampton method. A brief summary of the analysis is presented in this section. The undamped equation of motion in terms of the boundary degrees of freedom, *R* and internal degrees of freedom, *L* can be written as:

$$\begin{bmatrix} \boldsymbol{M}_{RR} & \boldsymbol{M}_{RL} \\ \boldsymbol{M}_{LR} & \boldsymbol{M}_{LL} \end{bmatrix} \begin{Bmatrix} \ddot{\boldsymbol{x}}_R \\ \ddot{\boldsymbol{x}}_L \end{Bmatrix} + \begin{bmatrix} \boldsymbol{K}_{RR} & \boldsymbol{K}_{RL} \\ \boldsymbol{K}_{LR} & \boldsymbol{K}_{LL} \end{bmatrix} \begin{Bmatrix} \boldsymbol{x}_R \\ \boldsymbol{x}_L \end{Bmatrix} = \begin{Bmatrix} \boldsymbol{f}_R \\ \boldsymbol{f}_L \end{Bmatrix} \tag{4.1}$$

where $\boldsymbol{M}, \boldsymbol{K}, \boldsymbol{x}, \ddot{\boldsymbol{x}},$ and $\boldsymbol{f}$ represent the mass, stiffness, displacement, acceleration and the force respectively. All of the quantities are partitioned either to the boundary or to the interior DOF based on their locations. The Craig-Bampton reduction [90], transform the physical co-ordinates to a set of physical DOFs at the boundary and modal coordinates at the non-boundary. Therefore,

$$\begin{Bmatrix} \boldsymbol{x}_R \\ \boldsymbol{x}_L \end{Bmatrix} = \begin{bmatrix} \boldsymbol{I} & \boldsymbol{0} \\ \boldsymbol{\Phi}_R & \boldsymbol{\Phi}_L \end{bmatrix} \begin{Bmatrix} \boldsymbol{x}_R \\ \boldsymbol{q}_m \end{Bmatrix} = \boldsymbol{CB} \begin{Bmatrix} \boldsymbol{x}_R \\ \boldsymbol{q}_m \end{Bmatrix}. \tag{4.2}$$

Here, $\boldsymbol{I}$ is the identity matrix and $\boldsymbol{\Phi}_R$ is a transformation matrix to relate the rigid body physical displacements at the boundary to the physical displacement of the elastic degrees of freedom, $\boldsymbol{x}_L$ and the transformation matrix is given by:

$$\boldsymbol{\Phi}_R = -\boldsymbol{K}_{LL}^{-1} \boldsymbol{K}_{LR}. \tag{4.3}$$

The $\boldsymbol{\Phi}_L$ is a transformation matrix that relates $\boldsymbol{q}_m$ to the elastic displacements of the physical degrees of freedom, $\boldsymbol{x}_L$. This is determined from the lower part of Eq. (4.1) with $\ddot{\boldsymbol{x}}_R = \boldsymbol{x}_R = \boldsymbol{f}_L = \boldsymbol{0}$ and $\boldsymbol{q}_m$ is the corresponding column vector of generalised or modal displacements. Usually, $\boldsymbol{q}_m$ is approximated using *m* (*m* << *L*) lower frequency modes. Here, the Craig-Bampton transformation matrix is represented as $\boldsymbol{CB}$. Using Eq. (4.2) and pre-multiply Eq. (4.1) by transpose of $\boldsymbol{CB}$ yields:

$$\begin{bmatrix} \boldsymbol{M}_{BB} & \boldsymbol{M}_{Bm} \\ \boldsymbol{M}_{mB} & \boldsymbol{M}_{mm} \end{bmatrix} \begin{Bmatrix} \ddot{\boldsymbol{x}}_R \\ \ddot{\boldsymbol{q}}_m \end{Bmatrix} + \begin{bmatrix} \boldsymbol{K}_{BB} & \boldsymbol{0} \\ \boldsymbol{0} & \boldsymbol{K}_{mm} \end{bmatrix} \begin{Bmatrix} \boldsymbol{x}_R \\ \boldsymbol{q}_m \end{Bmatrix} = \begin{Bmatrix} \boldsymbol{f}_R + \boldsymbol{\Phi}_R^T \boldsymbol{f}_L \\ \boldsymbol{\Phi}_L^T \boldsymbol{f}_L \end{Bmatrix}. \tag{4.4}$$

Equation (4.4) represents the general Craig-Bampton equation of motion. The subscript *B* denotes the boundary degrees of freedom of the reduced system and *m* denote the number of modes used in the reduction. The details of the individual terms are given in Appendix 1. In the base shake problem, a known acceleration $\ddot{\boldsymbol{x}}_R$ is applied to the boundary in order to determine the response

of the full structure. For a typical base shake analysis, there will not be any external force applied to the internal DOFs and the motion is applied to a single point or a number of rigidly connected boundary points. Hence, $\boldsymbol{f}_L$ and $\boldsymbol{K}_{BB}$ reduces to zero. Then, the lower part of Eq. (4.4) reduces to the uncoupled equation for the generalised response as:

$$\boldsymbol{M}_{mm}\ddot{\boldsymbol{q}}_m + \boldsymbol{K}_{mm}\boldsymbol{q}_m = -\boldsymbol{M}_{mB}\ddot{\boldsymbol{x}}_R \,. \tag{4.5}$$

Making use of the diagonal properties of generalised mass and stiffness matrices, the uncoupled modal equation for individual mode *i* with damping ratio $\boldsymbol{\zeta}_i$ can be written as:

$$\ddot{\boldsymbol{q}}_i + 2\boldsymbol{\zeta}_i\boldsymbol{\omega}_i\dot{\boldsymbol{q}}_i + \boldsymbol{\omega}_i^2\boldsymbol{q}_i = -\boldsymbol{p}_{iR}\ddot{\boldsymbol{x}}_R \tag{4.6}$$

where $\dot{\boldsymbol{q}}_i$ represents the modal velocity, ω_i^2 is the eigenvalue and $\boldsymbol{p}_{iR}$ is the modal participation factor. The modal participation factor can be calculated for each mode *i* using Eq. (A1.2) as:

$$\boldsymbol{p}_{iR} = \frac{(\boldsymbol{M}_{mB})_i}{m_i} = \frac{\boldsymbol{\Phi}_{iL}^T\left[\boldsymbol{M}_{LR} + \boldsymbol{M}_{LL}\boldsymbol{\Phi}_R\right]}{m_i} \,. \tag{4.7}$$

Each row of $\boldsymbol{p}_{iR}$ contains as many DOFs as defined in the restrained *R*–set and each column contains the contribution of all the modes and m_i represent the generalised mass of mode *i*. The modal participation factor helps to identify the important global modes of the structure, which give the maximum contribution to the frequency response, and also determines the force transmitted to the base. If the mode shapes are mass normalised, the generalised mass matrix becomes an identity matrix, then,

$$\boldsymbol{p}_{iR} = \boldsymbol{\Phi}_{iL}^T\left[\boldsymbol{M}_{LR} + \boldsymbol{M}_{LL}\boldsymbol{\Phi}_R\right] . \tag{4.8}$$

Here, a diagonal damping matrix, $\boldsymbol{C}_{mm}$ is assumed and it is defined for each mode *i* as [91]:

$$\boldsymbol{C}_{ii} = 2\boldsymbol{\zeta}_i m_i \boldsymbol{\omega}_i \,. \tag{4.9}$$

Equation (4.6) is in the standard form of the dynamic equation of motion and can be solved by assuming a steady state sinusoidal input at the restrained R-set with a forcing frequency of Ω_j, and amplitude U_R. Then,

$$\ddot{\boldsymbol{x}}_R = -\Omega_j^2 U_R e^{i\Omega_j t}. \tag{4.10}$$

Assuming that, modal displacement is given by:

$$\boldsymbol{q}_i = A e^{i\Omega_j t}. \tag{4.11}$$

Substituting Eqs. (4.10) and (4.11) in Eq. (4.6) gives the value of A as:

$$A = \frac{\Omega_j^2 U_R \boldsymbol{p}_{iR}}{(\omega_i^2 - \Omega_j^2 + 2i\zeta_i \omega_i \Omega_j)}. \tag{4.12}$$

Using the value of A together with Eqs. (4.10) and (4.11) gives the modal acceleration as:

$$\ddot{\boldsymbol{q}}_i = \frac{\boldsymbol{p}_{iR}\ddot{\boldsymbol{x}}_R \left(\frac{\Omega_j}{\omega_i}\right)^2}{1 - \left(\frac{\Omega_j}{\omega_i}\right)^2 + 2i\zeta_i \left(\frac{\Omega_j}{\omega_i}\right)}. \tag{4.13}$$

The physical acceleration response can be computed using the Craig-Bampton transformation and the modal acceleration as:

$$\begin{Bmatrix} \ddot{\boldsymbol{x}}_R \\ \ddot{\boldsymbol{x}}_L \end{Bmatrix} = \begin{bmatrix} \boldsymbol{I} & \boldsymbol{0} \\ \boldsymbol{\Phi}_R & \boldsymbol{\Phi}_L \end{bmatrix} \begin{Bmatrix} \ddot{\boldsymbol{x}}_R \\ \ddot{\boldsymbol{q}}_m \end{Bmatrix} \tag{4.14}$$

where $\ddot{\boldsymbol{x}}_R$ and $\ddot{\boldsymbol{x}}_L$ are the boundary and non-boundary accelerations respectively. The dynamic displacement can also be determined in a similar way. The boundary reaction, $\boldsymbol{f}_R$ for the typical base shake analysis can be obtained from Eq. (4.4) as:

$$\boldsymbol{f}_R = \boldsymbol{M}_{BB}\ddot{\boldsymbol{x}}_R + \boldsymbol{M}_{Bm}\ddot{\boldsymbol{q}}_m. \tag{4.15}$$

Neglecting the component due to the shaker and the rigid body motion, the constraint force or the force transmitted to the base can be expressed as follows:

$$\boldsymbol{F} = (\boldsymbol{M}_{Bm}\ddot{\boldsymbol{q}}_m)^T . \tag{4.16}$$

As in the case of acceleration, this base force can be computed for the required frequency band of interest during the base excitation analysis and the values corresponding to each frequency are stored in the separate rows of $\boldsymbol{F}$ for the subsequent analysis. Each row of $\boldsymbol{F}$ contains as many terms as the number of DOFs in the boundary set *B*. If the *B* set contains only a single location (i.e, 6 DOFs), then the first three columns of $\boldsymbol{F}$ correspond to the force transmitted to the base in three mutually perpendicular directions and the remaining three columns represent the corresponding moments about the axes at a particular frequency. These values are complex in nature and their absolute values are considered in this study.

4.3 Base Force Assurance Criterion

From Eq. (4.16), it can be seen that the value of the force and the moment transmitted to the base are proportional to the modal acceleration. The acceleration responses of the structure in physical coordinates are also computed using the modal acceleration. Hence, a quality measure of the transmitted force to the base seems an appropriate tool to access the capability of the analytical model to represents the forced response characteristics. Moreover, it is possible to measure the base force using a force measurement device during the dynamic test and this can be compared with the values obtained from the finite element analysis.

Let $\boldsymbol{P}$ be the absolute values of the transmitted forces to the base measured during the dynamic test in all the directions (note that $\boldsymbol{P}$ is also a function of frequency, ω). The corresponding absolute analytical values obtained from the each column of $\boldsymbol{F}$ (i.e. a set of values corresponds to each frequency in the entire frequency domain of interest) is a vector which can be correlated with

the measured value and the resulting matrix for all the forces is termed as the base force assurance criterion. It is defined as:

$$\boldsymbol{BFAC} = \frac{\left(\boldsymbol{P}^T\boldsymbol{F}\right)^2}{\left(\boldsymbol{P}^T\boldsymbol{P}\right)\left(\boldsymbol{F}^T\boldsymbol{F}\right)}. \tag{4.17}$$

Equation (4.17) is defined in a similar way as the MAC between the mode shapes. For the typical base shake problem with a statically determinate boundary (as considered in this work), BFAC is a square matrix of size 6. Each diagonal term in the BFAC corresponds to the respective DOF in the boundary set. It can be observed that the diagonal values vary between 0.0 and 1.0. If the diagonal value is 1.0, then it indicates a perfect correlation between the experimentally determined and the analytically predicted transmitted force to the base in the corresponding direction. In this computation, all the absolute values of $\boldsymbol{P}$ and $\boldsymbol{F}$ in the required frequency range are considered. Generally, spacecraft base shake test and analysis are performed in all the three translations and hence BFAC can be computed independently for all the directions of base excitation. It can be observed that, unlike SEREP, BFAC does not call for an analytical model reduction to the test location and hence both the analytical and the experimental values can be directly compared.

4.4 Results and Discussion

4.4.1 Spacecraft Models

Numerical examples are presented to illustrate that MAC and NCO check are not always able to correlate the quality of the FEM to the forced response characteristics. The examples also show that BFAC has a good correlation with the acceleration response and the dynamic displacements under the base excitation. The analyses are performed using three different sizes spacecraft structures where the base shake analysis and dynamic test are widely employed to qualify the structure before the launch. The finite element models of these spacecraft are shown in Fig. 4.1. This figure also shows the axes

system, relative size of the structures and the seven response locations chosen on each spacecraft for this study.

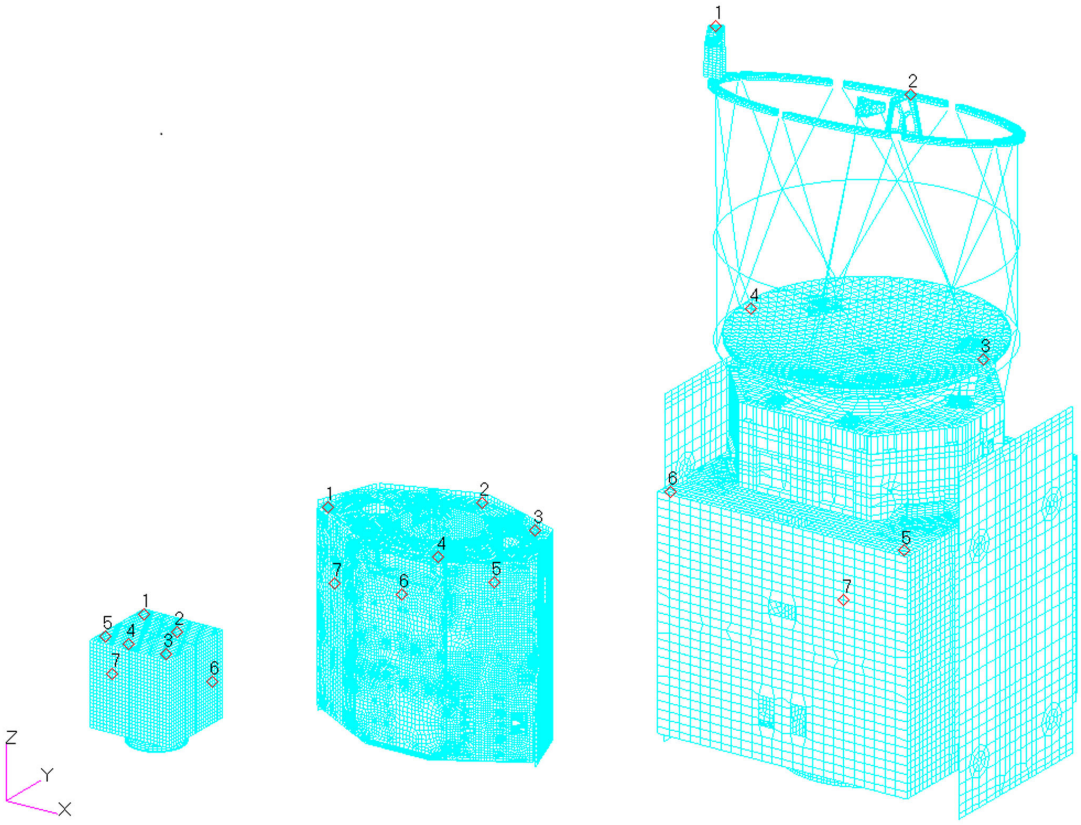

a) Mini Spacecraft **b) Medium spacecraft (SSTL, UK)** **c) Large spacecraft (EADS Astrium Limited)**

Fig. 4.1 Finite element models of the spacecraft and the response locations.

The dynamic characteristics such as the lowest five natural frequencies and the corresponding effective masses are shown in Table 4.1 to show the nature of these structures under the free vibration. It can be seen that, in the case of Spacecraft 2, the first mode has the highest effective mass (translation) in the *Y* direction and the second mode has the highest effective mass in the *X* direction. In the case of Spacecraft 1 and 3, the first mode has the highest effective mass in the *X* direction, whereas the second mode has the highest effective mass in the *Y* direction for the translation motion. Hence, a base excitation in the *Y* direction will result in the highest transmitted force in the direction of excitation due to the second mode of Spacecraft 1 and 3, but the first mode of Spacecraft 2 will give the highest transmitted force during the *Y* excitation.

Table 4.1 Dynamic characteristics of the spacecraft structures

Mode Num-ber	Frequency Hz	Effective Mass						Total Mass kg	Structure
		Translation, kg			Rotation, kgm^2				
		X	Y	Z	Rx	Ry	Rz		
1	38.0	49.7	2.7	0.1	0.6	8.2	1.7		
2	40.4	3.6	48.2	0	8.7	0.5	4.9		
3	58.0	0.3	0.1	0	0	0	2.3	75.7	Spacecraft 1
4	89.3	1.5	1.6	15.5	0.9	0.9	0		
5	103.0	1.3	0.8	0.7	0	0.1	0.2		
1	33.1	0	191.9	0	216.8	0	0		
2	43.2	175.3	0	0.1	0	229.6	0.4		
3	72.0	0.2	0	0.3	0	1.2	18.0	299.8	Spacecraft 2
4	74.7	0	5.6	67.9	0.1	0	0		
5	83.1	0.2	0	0.2	0	0.9	15.8		
1	16.0	762.0	0.3	0.1	1.4	4150.2	0.1		
2	16.6	0.3	815.4	0	4076.5	1.8	0		
3	16.9	0	0.1	0	0.4	0.1	0	1799.5	Spacecraft 3
4	20.1	0.1	0.2	0	0.9	0.4	0		
5	20.2	0.2	0.2	0	0.6	0.9	0		

4.4.2 Base Force Error

The MAC and NCO check are commonly employed to assess the quality of a finite element models in comparison with the experimental results. The MAC or NCO requirement of the FEM are specified by various organisations [9, 10] and those models clearing the criteria are used for the further analysis. However, it is interesting to evaluate MAC and NCO values of the spacecraft structures and the capability of the corresponding FEM to predict the dynamic characteristics of these structures under base excitation. In practice, FEM and experimental results contain inaccuracies and here, it is assumed that the experimental results are accurate ('true'). The FEM errors can be attributed to the human error, inaccuracies associated in the actual representation of the real system or

due to the lack of information available at the time of model generation, etc. It is obvious that, if there were no inaccuracies in the FEM, MAC and NCO would give a perfect correlation, however complete elimination of incorrectness is practically impossible. Here, these common modelling inaccuracies were simulated by creating a number of intentionally erroneous FEMs from the nominal FEM by altering the latter. Alterations were introduced in the load path by changing the number of joints or the stiffness of the structural elements, but the total mass of the structure was maintained as that of the nominal model because it is unlikely to have an error in the total mass of the structure. Generally, the mass of the full structure can be easily verified from the model.

Twelve different FEMs of each spacecraft were generated and the corresponding MAC and NCO values were calculated. The natural frequency of the first mode in the lateral *Y* direction (i.e. second mode in Table 4.1) and the corresponding effective mass for different FEMs of Spacecraft 1 are shown in Fig. 4.2a. The first natural frequency and the effective mass for each of these 12 FEMs that corresponds to Spacecraft 2 are shown in Fig. 4.2b. The natural frequency of the first mode in *Y* direction and the corresponding effective mass for different FEMs of Spacecraft 3 are shown in Fig. 4.2c. It shows that the maximum absolute change in effective mass and frequency among the Spacecraft 1 model are 10.0 % and 14.4 % respectively in comparison with its corresponding nominal values. It is observed in the first model of Spacecraft 1. The maximum change in the effective mass and frequencies for the Spacecraft 2 models are 27.7 % and 5.7 % respectively which corresponds to model 12. Among the Spacecraft 3 models, model 1 has the maximum absolute change in effective mass of 14.1% and frequency change of 15.1%.

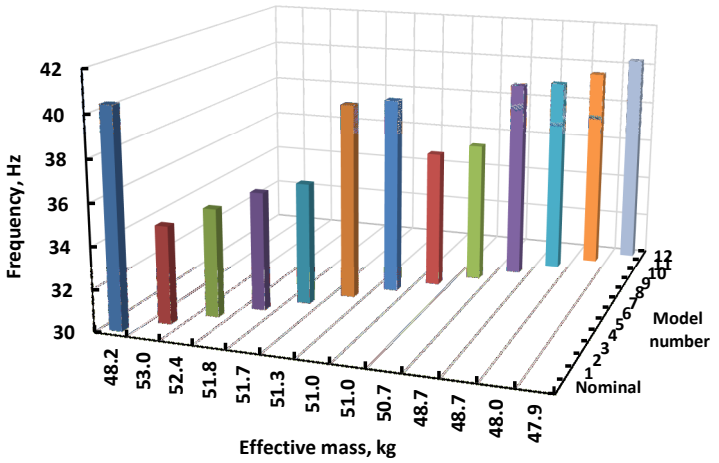

a) Spacecraft 1

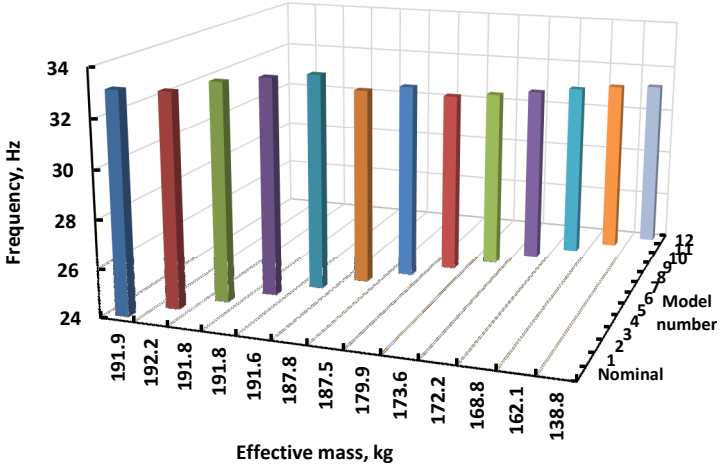

b) Spacecraft 2

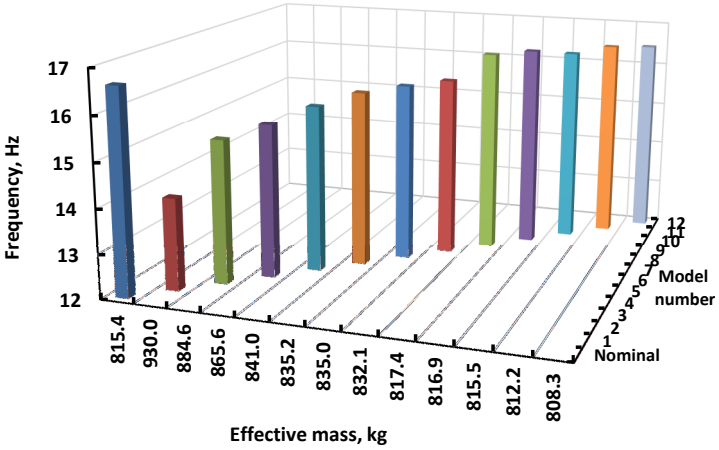

c) Spacecraft 3

Fig. 4.2 Natural frequency and modal effective mass of different FEMs.

To calculate the MAC and NCO, the target modes in the frequency range of 0.0 – 100.0 Hz were selected based on the modal effective mass, modal kinetic energy and modal strain energy as suggested by Chung and Sernaker [95]. It was observed from the corresponding nominal FEMs, that Spacecraft 1 and 2 have three and seven target modes respectively whereas Spacecraft 3 has 12 target modes in the 0.0 – 100.0 Hz frequency band. These target modes were considered for the correlation checks. The MAC and the NCO matrix were calculated using the equations:

$$\boldsymbol{MAC} = \frac{\left|\boldsymbol{\psi}^T \boldsymbol{\phi}\right|^2}{(\boldsymbol{\psi}^T \boldsymbol{\psi})(\boldsymbol{\phi}^T \boldsymbol{\phi})} \tag{4.18}$$

$$\boldsymbol{NCO} = \frac{\left|\boldsymbol{\psi}^T \boldsymbol{M}_{TAM} \boldsymbol{\phi}\right|^2}{(\boldsymbol{\psi}^T \boldsymbol{M}_{TAM} \boldsymbol{\psi})(\boldsymbol{\phi}^T \boldsymbol{M}_{TAM} \boldsymbol{\phi})} \tag{4.19}$$

where $\boldsymbol{\Psi}$ is the mode shape obtained from the nominal finite element model, $\boldsymbol{\phi}$ is the mode shape determined from the erroneous finite element model, $\boldsymbol{M}_{TAM}$ is the reduced mass matrix, and superscript *T* represents the transpose. Here, the $\boldsymbol{M}_{TAM}$ was computed using the SEREP.

The SEREP test analysis model was computed using the normalised modal matrix, $\boldsymbol{\Psi}$ as:

$$\boldsymbol{M}_{TAM} = (\boldsymbol{\Psi}^{\dagger})^T \boldsymbol{\Psi}^{\dagger} \tag{4.20}$$

where $\boldsymbol{\Psi}^{\dagger}$ is the generalised inverse [93] of the modal matrix $\boldsymbol{\Psi}$. For the computation of $\boldsymbol{M}_{TAM}$, the minimum required target modes were included and these modes were determined using 33 tri-axial sensors [103]. The MAC and the NCO values for all the 12 models of the three spacecraft structures were computed using Eq. (4.18) and Eq. (4.19) respectively. The average MAC and NCO values were computed using the diagonal values of the MAC and NCO matrices respectively for all the spacecraft models. The results are summarized in the Table 4.2, from which it can be observed that Spacecraft 1 has the highest MAC and NCO diagonal averages and it indicates the least error in the FEMs of Spacecraft 1 with respect to the nominal model. It should also be

noted that, the number of target modes and the complexity of the structure increases from Spacecraft 1 to 3.

Table 4.2 Correlation characteristics of the different spacecraft models

Model	Spacecraft 1		Spacecraft 2		Spacecraft 3	
	MAC diagonal average	NCO diagonal average	MAC diagonal average	NCO diagonal average	MAC diagonal average	NCO diagonal average
1	0.7977	0.9466	0.5533	0.3512	0.4123	0.2636
2	0.7864	0.9599	0.8182	0.8333	0.4055	0.2254
3	0.8396	0.9570	0.8380	0.8446	0.4018	0.2814
4	0.9236	0.9532	0.7559	0.7926	0.3607	0.3127
5	0.6931	0.9783	0.5541	0.2023	0.3432	0.3291
6	0.7202	0.9818	0.2930	0.2744	0.4310	0.2624
7	0.9252	0.9711	0.2540	0.2668	0.3236	0.2688
8	0.9396	0.9761	0.2327	0.2890	0.9957	0.9922
9	0.7207	0.9877	0.2442	0.2886	0.8570	0.8081
10	0.7208	0.9874	0.2366	0.2870	0.3857	0.3541
11	0.7048	0.9877	0.2223	0.2825	0.4070	0.3614
12	0.9949	0.9996	0.1884	0.2596	0.6662	0.5530

The illustration of individual MAC values of one model (Model 12) of Spacecraft 3 is shown in Fig. 4.3 and can be seen that many target modes have significant contribution to the MAC average. However, the perturbation introduced in the FEM affect the target modes in different levels.

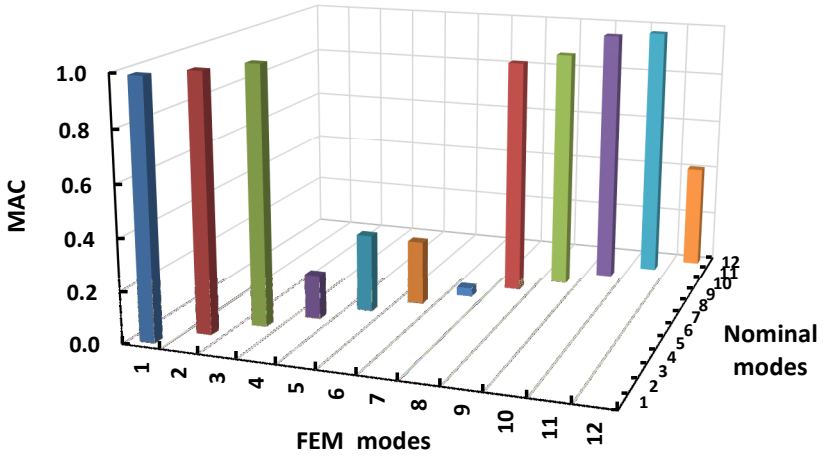

Fig. 4.3 MAC values of all the target modes (Model 12 of Spacecraft 3).

A 1g excitation, where *g* is the acceleration due to gravity (9.81 m/s^2), is applied in the *Y* direction to the base of all the spacecraft structures. The frequency responses at seven different locations for each spacecraft and the force transmitted to the base were calculated using a Matlab program with the reduced mass and stiffness matrices obtained from Nastran using the Craig-Bampton method. It was also considered a constant modal damping of $\zeta_i = 0.02$ (in Eq. (4.13)) for all the spacecraft models. It should be noted that, the values obtained from the nominal FEM of the corresponding spacecraft models were taken as the experimental or 'true' values for the correlation studies. As an example, the absolute values of the transmitted force in the *Y* direction for one of the erroneous models (model 1 for Spacecraft 1 and Spacecraft 3; model 12 for Spacecraft 2) along with the corresponding nominal values are graphically illustrated in Fig. 4.4 for all of the spacecraft. The frequency range considered in this study is 0.0-100.0 Hz for all structures.

As expected, Fig. 4.4 indicates that, the maximum transmitted force for the nominal or the erroneous model is primarily determined by the mode having the largest effective mass in the direction of excitation. All the spacecraft models considered here have few predominant modes in the direction of excitation in the required frequency band. Hence, the transmitted force in the direction of excitation has very few peaks. The percentage of error in the peak absolute transmitted force, $Error_{Force}$ is evaluated as,

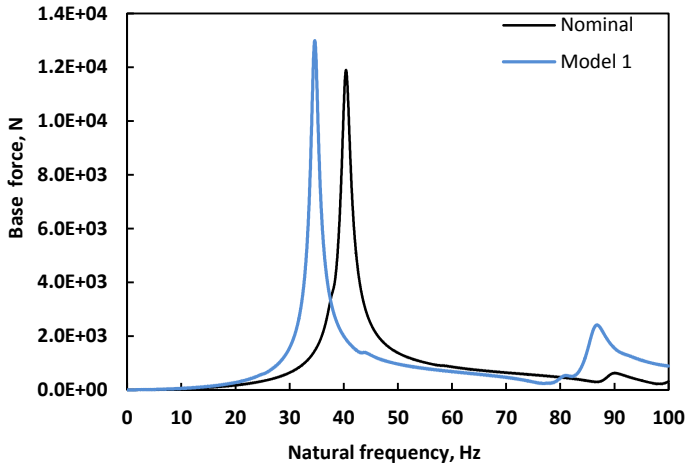

a) Spacecraft 1

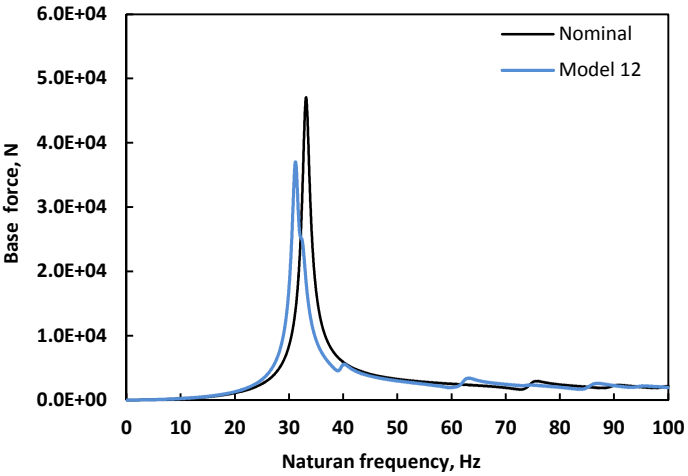

b) Spacecraft 2

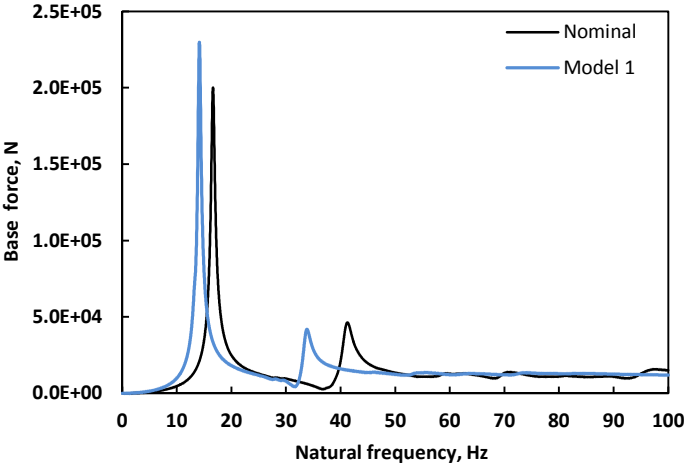

c) Spacecraft 3

Fig. 4.4 Transmitted force in the *Y* direction.

$$Error_{Force} = \left| \frac{f_{Nom} - f_{FEM}}{f_{Nom}} \right| 100 \tag{4.21}$$

where, f_{Nom} is the absolute value of the peak nominal force transmitted to the base in the direction of excitation and f_{FEM} is the absolute value of the peak transmitted force calculated from the erroneous finite element model in the direction of excitation. The error in the base force was calculated for 12 different models of Spacecraft 1 to 3 and these errors are plotted against the corresponding MAC diagonal average values as shown in Fig. 4.5. From this figure, it can be seen that occasionally the models with a very low value of MAC (0.4 or less) predict the transmitted force within an error below 5%.

At the same time, results in Fig. 4.5 also show that, sometimes a high value of MAC (above 0.9) can give more than 5% error in the transmitted force as seen in the case of Spacecraft 1 model. It can also be observed that, different models of the same spacecraft having equal MAC indicate different percentage of error (as high as 15% in Spacecraft 3) in the transmitted force during the base excitation. Hence, the variation of the average value of MAC with base force is unable to represent the possible error in the base force.

Variations of NCO average values with the base force error are shown in Fig. 4.6. As in the case of MAC, FEMs with the same NCO values sometimes indicate different levels of errors in the transmitted force. Sometimes, models with very low NCO diagonal values (less than 0.4) are able to represent the transmitted force within 5% error. It is evident from the Figs. 4.4–4.5, that neither the diagonal average of MAC nor NCO can quantitatively predict the capability of the finite element model to accurately compute the force transmitted to the base.

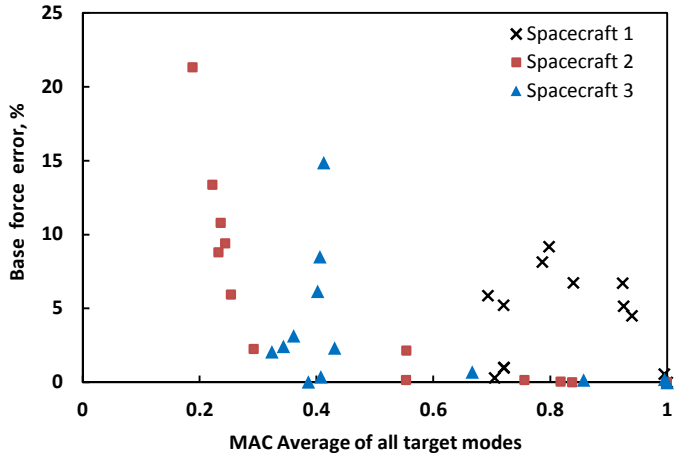

Fig. 4.5 Variation of base force error with the MAC values for three spacecraft models.

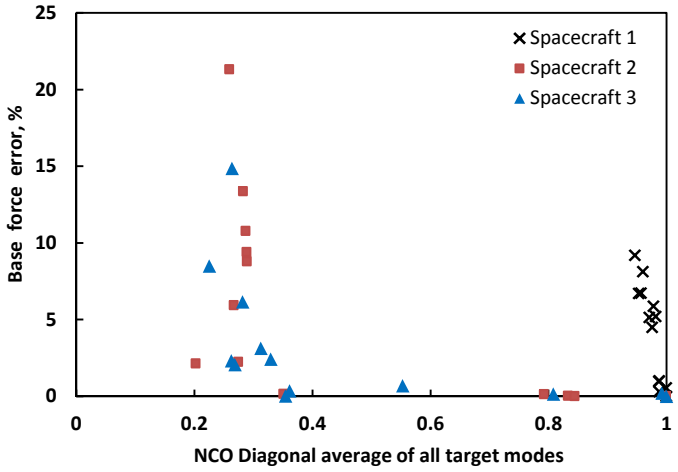

Fig. 4.6 Variation of base force error with the NCO values for three spacecraft models.

4.4.3 Acceleration Response

Spacecraft structures are designed for specific acceleration levels, normally specified in terms of *g* based on the launch vehicle [65]. Verification of acceleration levels on the different locations of the spacecraft is an inevitable requirement for a successful mission. The acceleration responses at the seven different locations shown in Fig. 4.1 for all the spacecraft models were computed for the unit acceleration (*1g*) at the base in the *Y* direction. Using the erroneous finite element models, these analyses were repeated for three spacecraft and the peak acceleration at seven locations was determined in the

frequency band. As an example, the absolute value of the acceleration response in the direction *Y* at location 1 (Fig. 4.1) when the spacecraft is excited with *1g* in the *Y* direction for one of the erroneous model along with the corresponding nominal values are shown in Fig. 4.7 for different spacecraft models.

It can be observed that the response of Spacecraft 1 and 2 at location 1 primarily occurs at one frequency of excitation whereas Spacecraft 3 has multiple peaks thus indicates the involvement of many modes. The erroneous finite element models alter both the response levels and the frequency at which the resonance occurs but show the similar characteristics of the nominal models. The percentage error in the magnitude of peak acceleration, $Error_{Accn}$ at a particular response location is evaluated as:

$$Error_{Accn} = \left| \frac{a_{Nom} - a_{FEM}}{a_{Nom}} \right| 100 \tag{4.22}$$

where, a_{Nom} is the absolute value of the nominal peak acceleration in the frequency band and a_{FEM} is the absolute value of the peak acceleration obtained from the erroneous finite element model. The average error in peak acceleration is then computed using the values observed at the seven different locations.

Figure 4.8 shows the average absolute acceleration errors in the *Y* direction with the corresponding average MAC values for different erroneous models of three spacecraft structures during *1g Y* excitation. It can be observed that models with MAC values, which are equal or close (for example, maximum difference of 0.05) can result in large changes in the acceleration response. These results also show that, models with the MAC < 0.8 are sometimes able to predict the acceleration within 5% error and models with lower MAC values are sometimes better than the model with higher MAC values for the response predictions. In Fig. 4.9, the average NCO diagonal values were plotted with the error in peak acceleration for three spacecraft and this figure shows the similar trend of Fig. 4.8. As observed in the case of base force, MAC or NCO does not give any useful indication on how the FEM will represent the acceleration response if the model possesses a particular value of MAC or NCO.

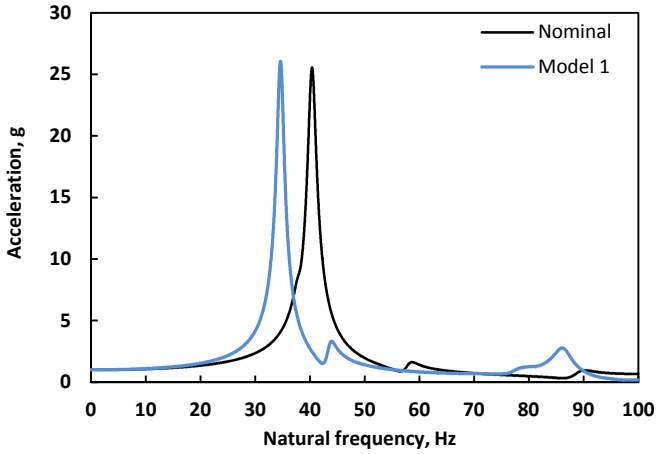

a) Spacecraft 1

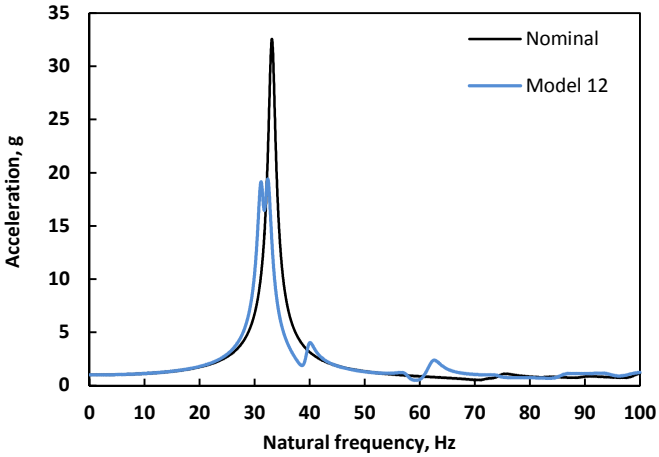

b) Spacecraft 2

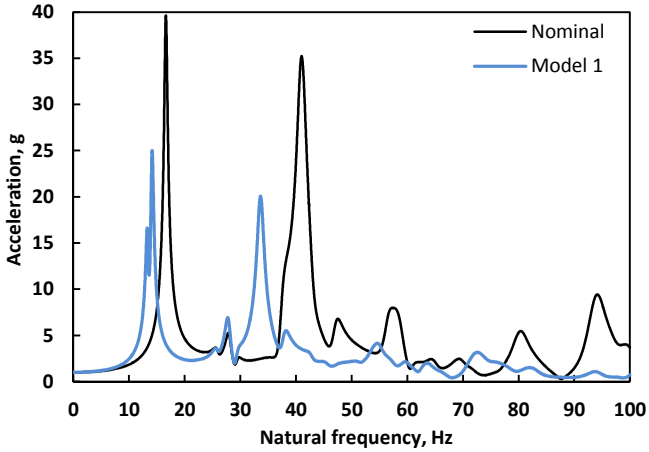

c) Spacecraft 3

Fig. 4.7 Typical frequency responses.

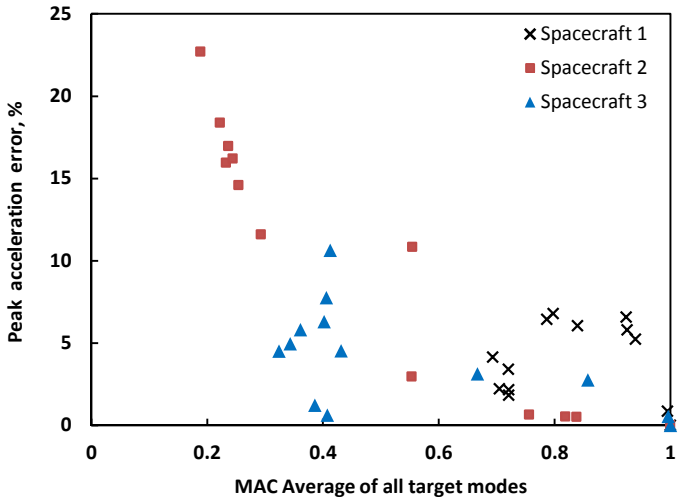

Fig. 4.8 Variation of peak acceleration error with the MAC values for three spacecraft models.

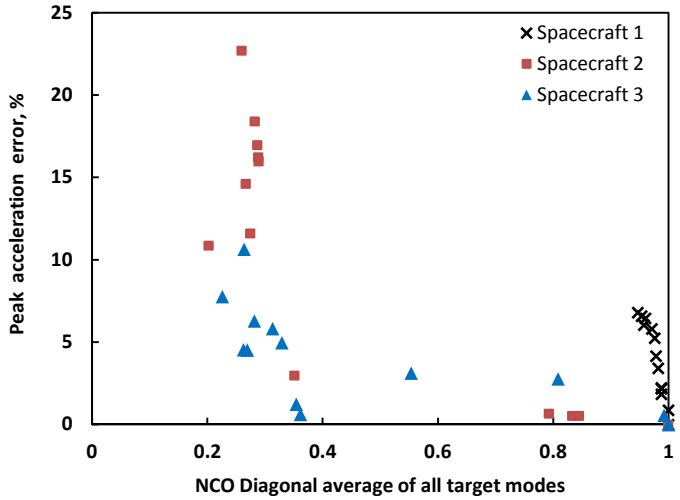

Fig. 4.9 Variation of peak acceleration error with the NCO values for three spacecraft models.

4.4.4 Displacement Response

The dynamic displacements at the salient points on spacecraft structures give an indication of the deformation caused on the structure during the vibration exposure and this is proportional to the level of stress. This also expedites the computation of stress induced in the vital structural components during the dynamic loading. The dynamic displacements at seven different locations on each spacecraft structure were calculated in the 0.0–100.0 Hz range during

base excitation. These locations are the same as the locations where the accelerations were monitored. As in the case of the acceleration error, the error in the peak absolute displacement in the direction of *Y* at the seven locations were computed when unit (*1g*) acceleration in the *Y* direction was applied at the base. The average peak displacement errors with the corresponding nominal parameters were estimated for the different models of all spacecraft.

Figure 4.10 shows the average displacement errors for different erroneous models in the *Y* direction with the corresponding MAC values whereas Fig. 4.11 shows the variation of peak absolute displacement error with NCO diagonal average for three spacecraft models. It can be observed from the Spacecraft 1 model in Fig. 4.11 that, even if the FEM has NCO diagonal values above 0.95, the error in the peak dynamic displacement may reach as high as 40%. However, the maximum off diagonal term in the NCO matrices of Spacecraft 1 models was only 0.08 as observed in model 1. This clearly indicate that these models can easily pass the commonly used correlation criteria [9, 10] for the finite element models of the spacecraft structures but fail to represent the force response characteristics. As observed in the case of the base force and peak acceleration, neither MAC nor NCO indicates the ability of the model to represent the dynamic displacement. It can be noted that the dynamic response at a particular location depend not only on the mode shape and the corresponding frequency, but also on the effective mass of the particular mode. These standard correlation methods do not consider the mass participation and thus lead to poor response predictions. This is in accordance with the results shown in Chapter 3, where, it was shown using the Monte Carlo simulation that a model with a higher NCO value is not necessarily good in representing a better receptance than a model with lower NCO value [103]. It should also be noted that MAC and NCO check are insensitive to eigenvector norms as arbitrary scaling of eigenvectors do not change the index obtained from MAC or NCO.

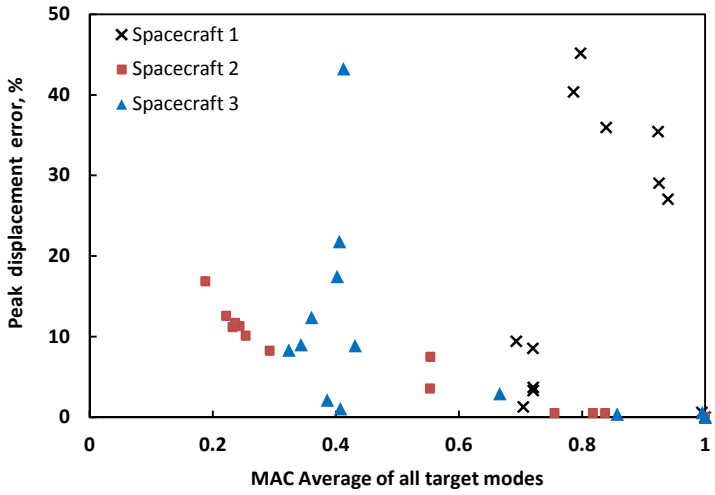

Fig. 4.10 Variation of peak absolute displacement error with the MAC values for three spacecraft models.

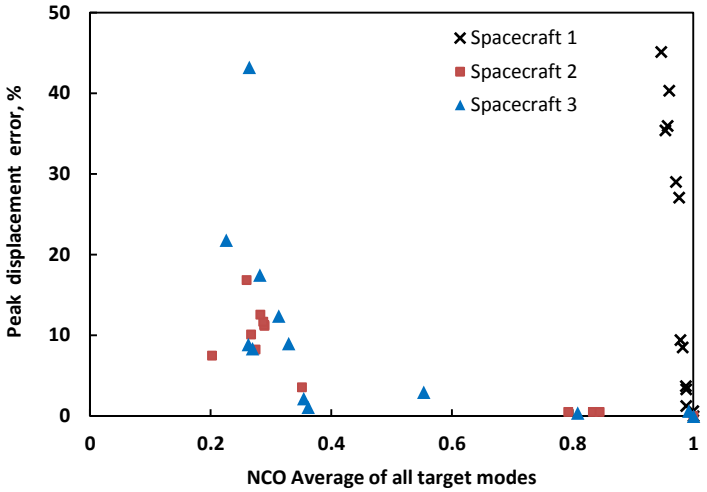

Fig. 4.11 Variation of peak absolute displacement error with the NCO values for three spacecraft models.

4.4.5 Base Force Assurance Criterion

It has been shown that neither MAC nor NCO check is a suitable indicator to assess the capability of a finite element model to accurately simulate the forced vibration characteristics. The force transmitted to the base can be measured during a base excitation test and analytically it can be computed using Eq. (4.16). As in the previous case, the force transmitted to the base computed using the nominal FEM is taken as the experimental ('true') value

and the transmitted force obtained from the different erroneous FEMs were taken as the possible FE predicted forces. These computations were performed in the 0.0 – 100.0 Hz range and then the comparison of both of the base force vectors were carried out using Eq. (4.17), thus the BFAC values for the different finite element models of the same spacecraft were obtained. The BFAC values of the second and third spacecraft were also calculated in a similar way. As per the definition of BFAC for the typical base shake analysis, this is a 6x6 matrix for each direction of excitation. The first three terms in the diagonal of this matrix represents the correlation of transmitted force with the nominal values in the direction *X, Y* and *Z* respectively whereas the last three terms represents the correlation of trasmitted moments in the respective axes.

Generally, the forced vibration test of the spacecraft is performed by exciting the base in three mutually perpendicular axes (one axis at a time) during which accelerations, transmitted force and the moments are measured. The peak absolute acceleration error in the frequency band of interest (calculated at the seven different locations on the spacecraft) for different models of the each spacecraft with BFAC diagonal average values for the *Y* direction of excitation is shown in Fig. 4.12. The trend line for the spacecraft models indicate that, unlike MAC or NCO, BFAC can reasonably well represent the FEMs capability of estimating the acceleration response error at the important locations on the spacecraft. Figure 4.13 shows the variation of BFAC average value against the peak absolute displacement error in the *Y* direction for each of the three spacecraft models.

It can be observed that, unlike MAC or NCO shown in Figs. 4.8–4.11, a typical value of the BFAC average always indicates the possible error in the absolute acceleration and the absolute displacement. Results also show that, if a spacecraft model has a BFAC value greater than 0.8, then the error in the peak acceleration or dynamic displacement is less than 5%. Also, these types of plots shown in Figs. 4.12–4.13 can be easily generated for any spacecraft model in the required direction of excitation prior to the dynamic testing to assess the ability of the FEM to simulate the dynamic response when the FEM contains some modeling inaccuracies.

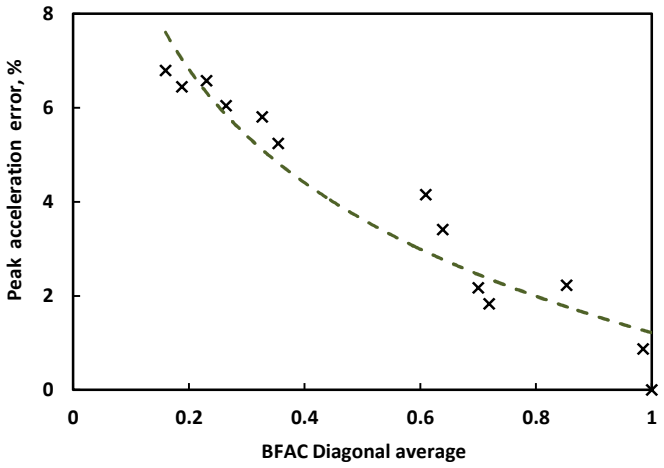

a) Spacecraft 1

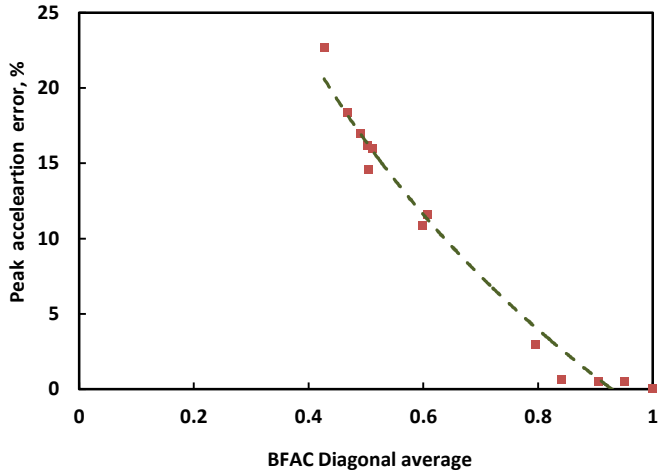

b) Spacecraft 2

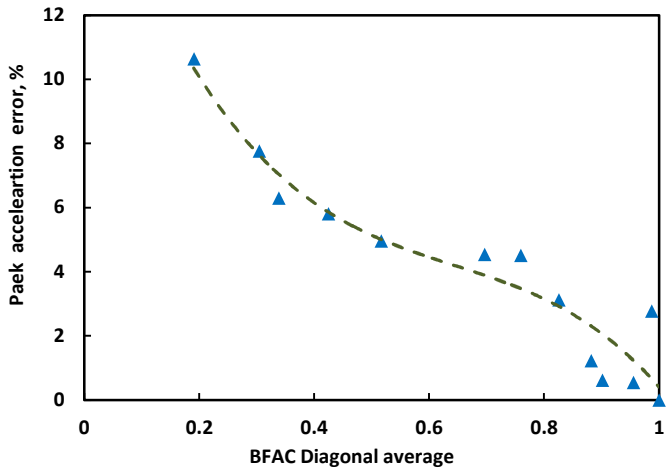

c) Spacecraft 3

Fig. 4.12 Variation of peak acceleration error with the BFAC average value for three different spacecraft models for the excitation in the *Y* direction.

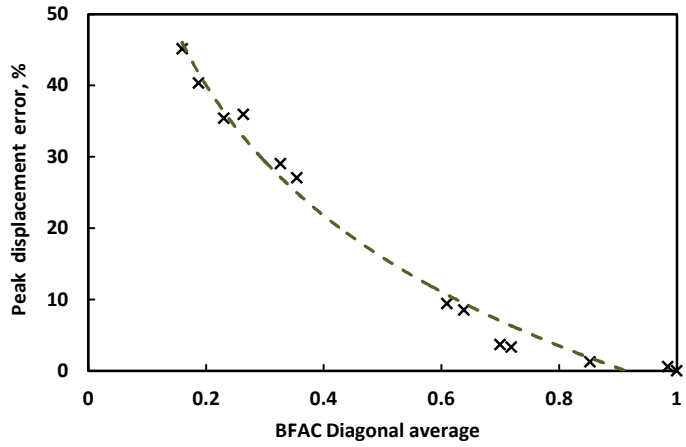

a) Spacecraft 1

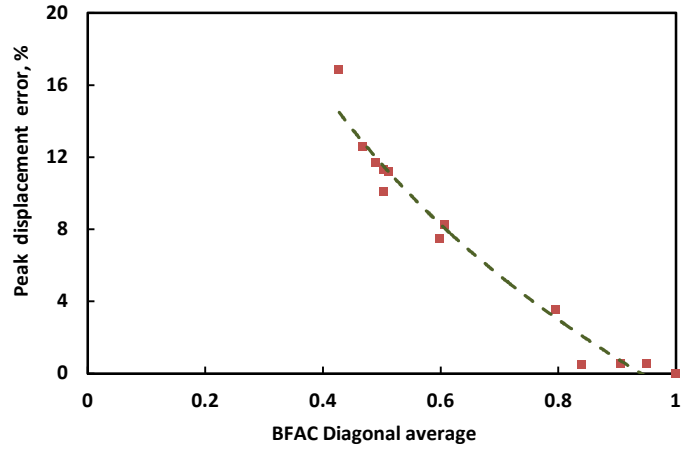

b) Spacecraft 2

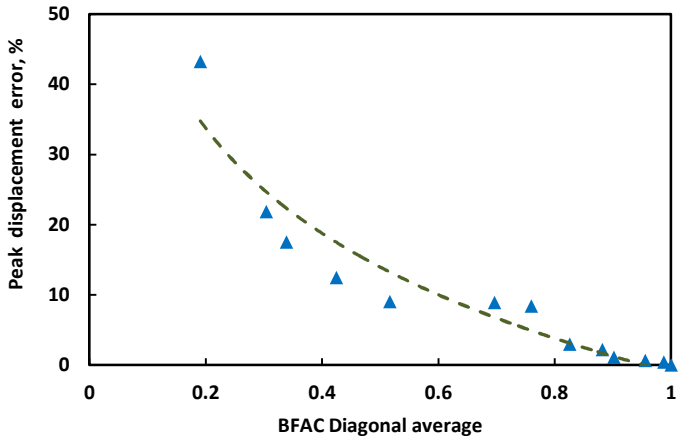

c) Spacecraft 3

Fig. 4.13 Variation of peak absolute displacement error with the BFAC average value for three different spacecraft models for the excitation in the *Y* direction.

The BFAC values are also shown for the *1g* excitation in the *X* direction for the most complex structure considered here i.e., Spacecraft 3. The absolute acceleration error and the absolute displacement error in the *X* direction in the 0.0 – 100.0 Hz range were also computed at the same seven response locations for all the models of this structure under the base excitation in the *X* direction [106]. The corresponding plots are shown in Fig. 4.14. It can be seen that, as in the case of *1g Y* excitation, the BFAC average in 1g *X* also correlates reasonably well with the dynamic characteristics error. The results for the other two spacecraft also show the same trend during the excitation in the *X* direction but are not shown here for briefness.

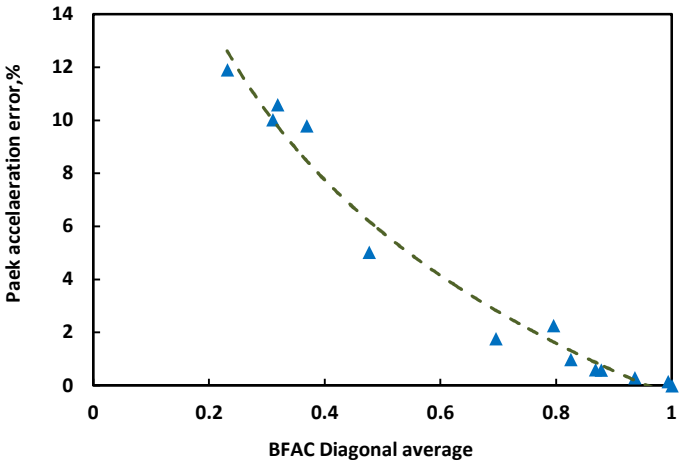

a) Acceleration error

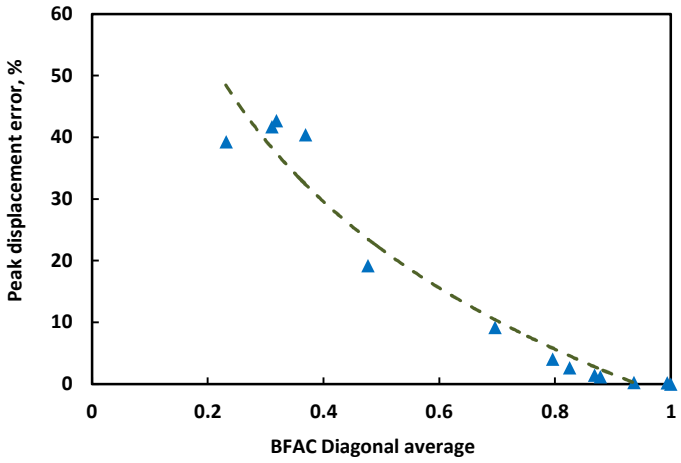

b) Displacement error

Fig. 4.14 Correlation of dynamic characteristics with BFAC average value for Spacecraft 3 for the excitation in the *X* direction.

In all the examples (shown above) used the absolute value of the base force to compute the BFAC. The BFAC values of spacecraft 3 under the excitation in *1gY* were also computed using the complex base force and its correlation with the acceleration and displacement error are shown in Fig. 4.15. It should be noted that, in this case, the absolute value of $\boldsymbol{P}^T\boldsymbol{F}$ is required in the numerator of Eq. (4.17). It can be noticed that, the BFAC show the same trend as before (Figs. 4.12c – 4.13c) and correlate reasonably well with the dynamic characteristics error.

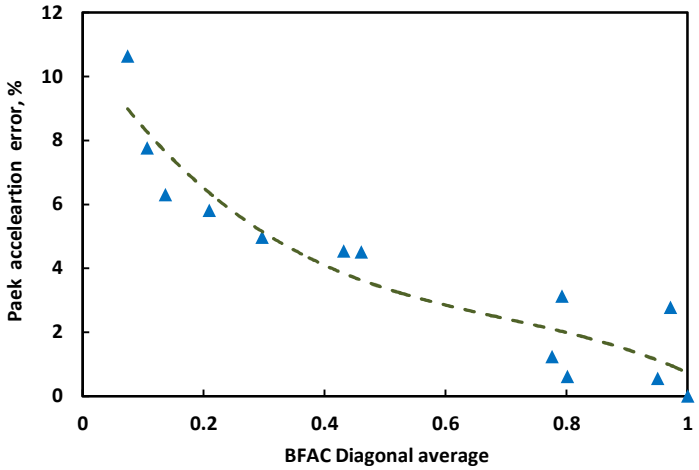

a) Acceleration error

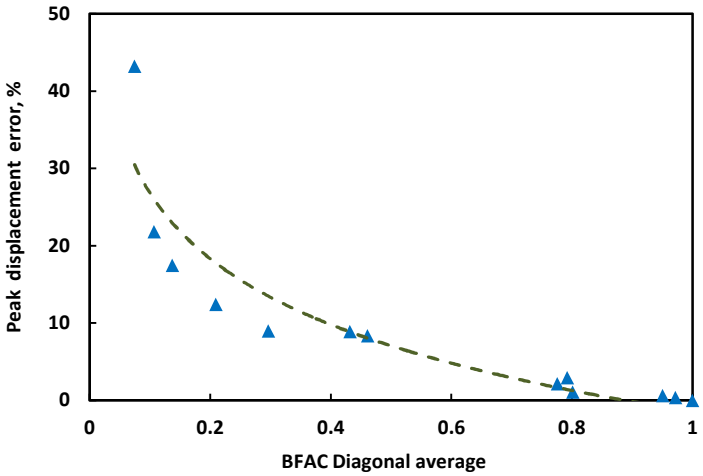

b) Displacement error

Fig. 4.15 Correlation of BFAC average value using the complex force with the dynamic characteristics of Spacecraft 3

4.4.6 Comparison of Synthetic and Intentionally Erroneous Modes

To study the robustness of SEREP as in the previous chapter, the synthetic modes were generated from the nominal FEM modes using the random numbers and a percentage of inaccuracy (Eqs. (3.9)–(3.11)). The base excitation analysis of different spacecraft models were carried out using the physically or intentionally erroneous modes obtained from the nominal FEM by changing the stiffness of the structure. A comparison between the modes obtained using these two methods are performed in this section.

Figure 4.16 shows the nominal mode (the second mode) of Spacecraft 2 and the corresponding physically altered mode determined using 33 tri-axial sensors. This particular mode pair has a MAC value of 0.8983. The figure also shows a synthetic mode obtained by applying a fixed percentage of inaccuracy to the nominal mode as explained in the Chapter 3 (Eqs. (3.9)–(3.10)). An inaccuracy of 59.3% is required to generate this synthetic mode, to give an average MAC value of 0.8983 with the corresponding nominal mode, using 1000 Monte Carlo simulations. It can be seen that there is a reasonable resemblance between the physically altered and the synthetic mode.

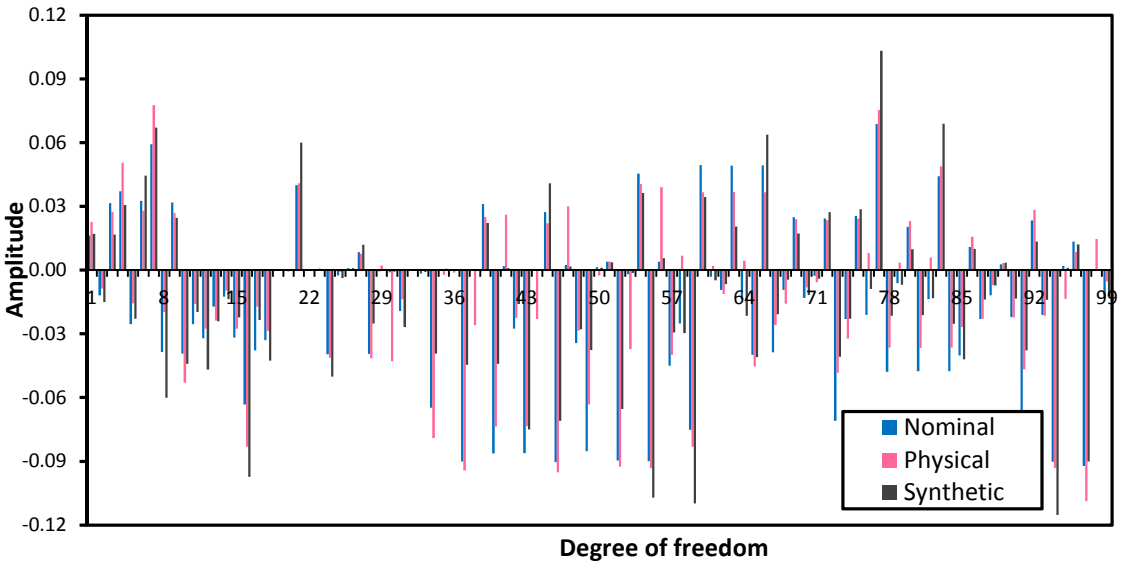

Fig. 4.16 MAC of synthetic and physically altered modes.

The comparison of NCO using the physically altered mode and the synthetic mode also has been performed. The first nominal mode of Spacecraft 3 and

the corresponding physically altered mode are shown in Fig. 4.17. This particular mode pair has a NCO value of 0.9813. Here, the SEREP TAM was used for the NCO, which was generated using 12 target modes as in the previous section. The figure also shows a synthetic mode obtained with a 5.5% inaccuracy with respect to the nominal mode. It has been observed that, when 1000 Monte Carlo simulations were performed with a 5.5% inaccuracy in the synthetic mode will result in a NCO average of 0.9814 for the first mode. As the correlations between the modes are very high, the modes obtained from the physically altered and synthetic modes closely match the nominal mode.

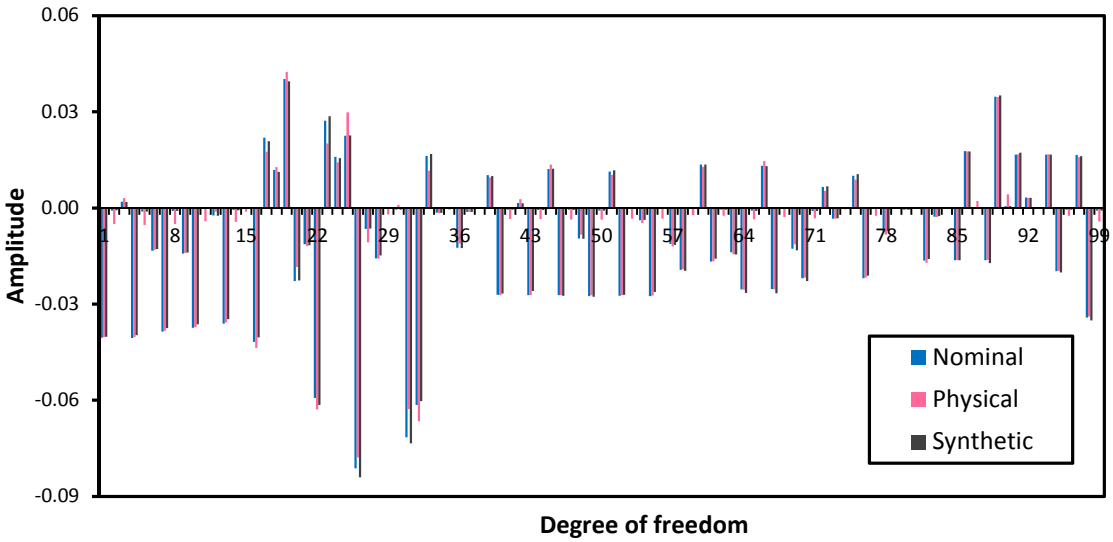

Fig. 4.17 NCO of synthetic and physically altered modes.

Based on the above results, it can be concluded that, the modes obtained from the synthetic methods (along with Monte Carlo simulations) and the physically erroneous models are essentially the same. Hence, a similar correlation values using MAC and NCO can be obtained either by a statistical approach or by a more tedious physically altered models. However, the synthetic approach used here only alters the mode shapes and is unable to alter the modal effective masses, which are required for the base excitation analysis.

4.5 Summary

The base shake dynamic tests are widely used in the space industry to verify FEM and to verify the design margins. The analytical results are compared with the test results using the MAC and the NCO check and it is considered that the FEM is suitably representing the actual system if it possesses a certain value of these criteria. In this study, it was shown that these validation methods do not always assure the capability of the FEM to represent the forced response characteristics. Three different spacecraft structural FEMs were considered and the results of the analyses were taken as true experimental results. These nominal models were then modified to produce a number of intentionally erroneous finite element models. The dynamic characteristics of the erroneous models were then compared with those of the nominal model. It was observed that, sometimes for the same modal assurance criterion value, two different models of the same spacecraft can give a reasonably different percentage error in the force transmitted to the base (as high as 15%). A similar phenomenon is observed in the case of the NCO criterion. It is also observed that a very low value (less than 0.4) of the diagonal average of the MAC or NCO occasionally gives a good estimate (less than 5% error) of the base force, peak acceleration and the dynamic displacement. Such a low correlation value is generally regarded as an unsuccessful validation of the model. It was also noticed that sometimes models with lower MAC or NCO values gave better predictions of the forced response characteristics than a model with a higher MAC or NCO value.

The proposed base force assurance criterion was found to be suitable for the base shake analysis. In the examples shown in this work, it correlated with capability to predict the error in the peak acceleration response and peak absolute displacement and hence also the stress in the structure in a more effective way. These correlation values for a particular spacecraft can be easily computed prior to the actual dynamic test by generating a number of FEMs of the same structure and thus, it can predict the capability of FEM to represent the acceleration response and the stress in the structure. It was also observed that for these examples, a BFAC with an average value of 0.8 or above ensures

that the error in the displacement or the peak acceleration responses are less than 5% of the nominal value. Although this criterion has been applied only to the spacecraft structures in this study, it could also be applied to any structure under base excitation. Also, a comparison of synthetic and physically altered modes with the nominal mode has been performed and it has been observed that, both these modes can give identical MAC or NCO values by varying the percentage of inaccuracies in the synthetic modes. Hence, the robustness of the correlation method can be performed either using the synthetic modes or physically altered modes.

Different aspects of the validation of conventional spacecraft structures have been presented in Chapter 3 and 4. Multi-physics or multi-functional structures are increasingly being used in the aerospace applications. However, these types of systems are currently used at the subsystem level to meet the specific requirements of the mission. The correlation aspects of two types of commonly employed multi-physics subsystems widely used in aerospace applications will be addressed in the following chapters.

Chapter 5.
Correlation of Viscoelastic Systems

5.1 Introduction

Multi-physics/multi-functional systems are extensively used to enhance the structural performance of numerous systems. This also helps to enhance the structural capability beyond the mere load bearing to self-sensing, diagnosis and control capabilities and hence makes the structure an 'intelligent' system. Here, two types of widely employed multi-physics systems, namely viscoelastic damped system and an electric circuit fed piezoelectric systems are considered. Although a number of FEM correlation methods such as MAC [6], NCO check [5], COMAC [28] and FRAC [30] are available for conventional structures, a specific correlation method for multi-physics system has not been reported. Moreover, these subsystems are developed independently and sometimes supplied by an external agency. A specific correlation method for subsystems will help the space agency to suitably assess the system before it is integrated to the main structure. The correlations of FEMs of viscoelastic and shunted systems are assessed using common and simple configurations. However, the concept can be adapted to more complex systems. The correlation of the piezoelectric system is described in the next chapter.

Viscoelastic materials have been effectively used to reduce the vibration response of light weight structures such as spacecraft, reaction wheel assemblies, and aeroplane fuselages [107]. Thin aluminium plates embedded with viscoelastic materials can be used to mount small antenna such as a telemetry and tele-command patch antennae or micro strip antennae. Honeycomb sandwich panels have widespread use in aerospace structures to form equipment mounting decks and solar panels. These panels are generally larger in dimension than the thin plates mentioned previously along with

higher load bearing capability. Typically, the solar panels are assembled using hold down blocks during launch and deployed on orbit. Viscoelastic materials can also be used to increase the damping in the plates and sandwich structure and this passive damping method is easy to implement and more economical than active damping techniques [84]. The capability of viscoelastic material to exhibit properties of both a viscous fluid and an elastic solid is effectively used to absorb the vibration energy and thereby reduce the structural responses. The amount of viscous or elastic behaviour depends primarily on the temperature of the system and the frequency or the rate of loading. The effectiveness of the damping of such systems is generally assessed using the modal loss factor of a specified mode of interest. A modal loss factor is the ratio of the total energy dissipated per cycle to the maximum amount of energy stored during the cycle [108].

The tuned viscoelastic damper, free layer damping and constrained layer damping are various ways to attach this material to the structure for vibration energy dissipation [84]. The first method is used to reduce the vibration in a single or narrow band of frequencies whereas the last two methods can be designed for the vibration control of single or multiple modes of vibration. In the free layer damping, the damping material is bonded on to the free face of the structure, but in the constrained layer damping, viscoelastic layers are placed between the stiff face sheets. Hence, in the constrained layer damping, the viscoelastic core undergoes high cyclic shear deformation which leads to thermal heat generation and a portion of the vibration energy is dissipated as heat under dynamic loading [107]. This constrained layer damping is more effective than the free layer damping [83, 84].

The accurate determination of the loss factor is an important step in the design of damped structural systems using viscoelastic material. The pioneering work to determine the loss factor of viscoelastic systems using an energy method was performed by Ungar and Kerwin [85]. A FEM has been effectively utilised to analyse the viscoelastic damping in practical systems, which often has complicated geometries [83, 107, 109, 110]. Among these methods, the Modal Strain Energy (MSE) [83] method is widely used to determine the loss factor of constrained viscoelastic systems using a commercial finite element program.

Here, the MSE method is used to determine the loss factor of a simply supported sandwich plate and a honeycomb sandwich panel constrained at the hold down locations. The second model simulates the solar panel of a spacecraft.

The MAC and NCO are the most commonly employed correlation tools for validating the FEMs. The correlation of FEMs of the viscoelastic systems is carried out using MAC, NCO, and BFAC methods and the usefulness is assessed on the analytical prediction of the loss factor of such systems, although these correlation methods are not specifically designed for it. Two different systems are analysed to consider the various modelling inaccuracies such as boundary conditions, material properties, and hinge stiffness (honeycomb sandwich panel). The effect of temperature on the MAC and NCO is also studied.

5.2 Determination of the Loss Factor

The modal loss factor for the constrained layer damping system can be calculated using the undamped modes and the material loss factor for each constituent material. Generally, the face sheet material will have an exceedingly low loss factor compared with the viscoelastic core. Hence, the modal loss factor, η^r for each mode r is approximated as [83]:

$$\eta^r = \eta_v \left(\frac{V_v^r}{V_T^r} \right) \tag{5.1}$$

where η_v denotes the loss factor of the viscoelastic core at the resonance frequency of mode r, V_v^r and V_T^r are the elastic strain energy of the viscoelastic material alone and the strain energy of the total system during the mode r. Generally, the ratio, η^r/η_v, can be directly obtained from the FEM results as the ratio of modal strain energy of the core to the total elastic strain energy. In this study, η_v is taken as 1.0 at 30^0 C for the 3M viscoelastic core in the desired frequency range [111]. Although, this modal strain energy method computes the loss factor from the undamped normal modes, it gives a reasonably good approximation of the damping and leads to an easy way of designing the damping system. However, the frequency dependent material properties of the

core need some approximation to accommodate this method. The derivation of Eq. 5.1 is shown in Appendix 2.

5.2.1 Configuration and Modelling of the Viscoelastic Systems

To study the correlation of FEMs containing viscoelastic materials, a rectangular sandwich plate with viscoelastic layers embedded between the face sheets and a structure with viscoelastic layers embedded between the two honeycomb sandwich panels has been modelled in Nastran [94]. The first model consists of a sandwich plate with a length of 0.3 m and width of 0.2 m. The FEM and the cross sectional details in millimetres (mm) are shown in Fig. 5.1. The viscoelastic core is constrained between the two identical aluminium face sheets and this has been modelled using eight node Hexagonal elements (HEX), whereas the face sheets were modelled using four nodes quadrilateral shell elements (QUAD4) of Nastran. The FEM consist of 1800 elements and the properties of different materials used in the FEM are given in the Table 5.1 [83, 111]. For the viscoelastic material, the 3M viscoelastic polymer properties at 30^0 C and 50 Hz have been considered for the analysis of the sandwich plate. The frequency at which the material properties were taken is the average frequency of the two target modes of the system (described in the following section). As the viscoelastic properties at all frequencies are not available, estimated values using the reference [111] are shown in Table 5.1.

A simply supported boundary condition along the edges of the plate has been applied and these constrained DOFs were rigidly connected together to a single node located at the base [0.15, 0.1, -0.02]. This base node is located directly below the diagonal intersection of the bottom face sheet as the nodes on the lower face sheet are located at z=0 plane. The base excitation is applied to this node in the subsequent analysis. The total mass of the system is 80.98×10^{-3} kg and the coordinate system of the FEM is shown in Fig. 5.1a.

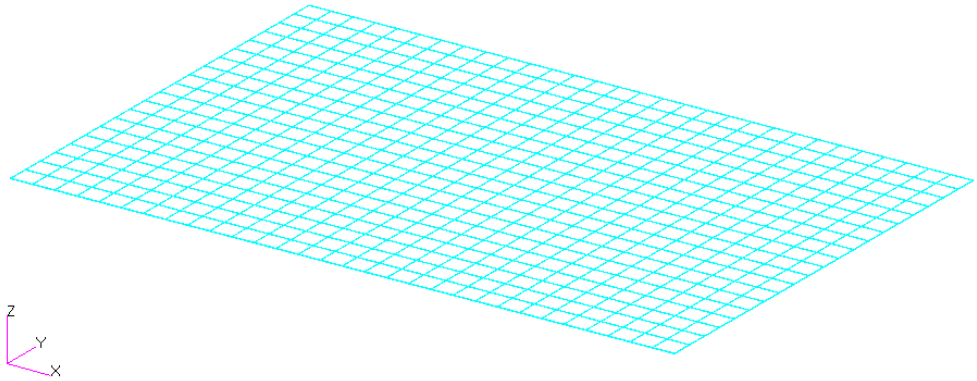

a) FEM and the axis system

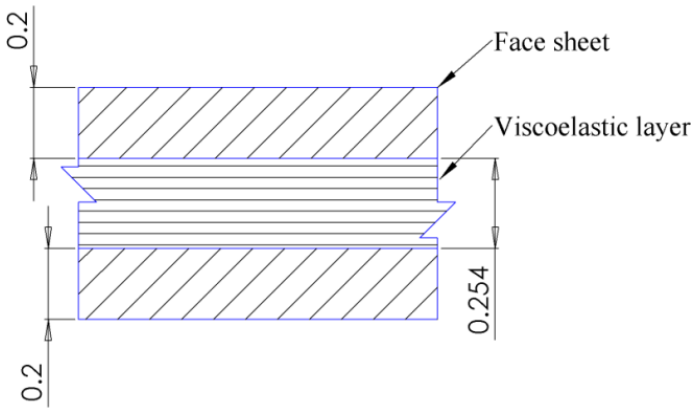

b) Cross sectional view

(All dimensions are in mm)

Fig. 5.1 Model of a constrained layer viscoelastic system.

Table 5.1 Material Properties

Property	Material			
	Honeycomb core	Aluminium	3M	
			50 (Hz)	132 (Hz)
Young's modulus (Pa)	E_{11} =1000.0 E_{22} =1000.0	E = 68.9x10^9		
Shear modulus (M Pa)	G_{13} = 138.0 G_{23} = 138.0		G =2.0	G =3.6
Poisson's ratio, ν	0.3	0.3	0.49	0.49
Density, ρ (kg/m^3)	32.0	2740.0	999.0	999.0

(Subscripts *1* and *2* indicate the in-plane directions; *3* thickness direction)

The second FEM represents a typical solar panel of a spacecraft. The FEM, the axis system and the cross sectional details are given in Fig. 5.2. The chosen solar panel has a rectangular shape (0.8 m x 0.6 m) and the viscoelastic layers are constrained between the two identical sandwich panels and each of these sandwich panels consist of two thin aluminium face sheets ($1.0x10^{-4}$ m thick) and a honeycomb core. This configuration is chosen to obtain the maximum damping effect by placing the viscoelastic layers near the maximum shear stress area along with the manufacturing feasibility of the sandwich assembly. The honeycomb sandwich panels are modelled using layered shell elements (PSHELL) of Nastran and viscoelastic layers are modelled using eight nodes hexagonal elements. The model consists of four identical hold down blocks, which support the panel to the main spacecraft during the launch. Each hold down has an axial stiffness of $1.0x10^{10}$ N/m and a rotational stiffness of $1.0x10^{8}$ N/rad. The nodes in the each hold down area were rigidly connected together and joined to the base point using six CELAS elements, the first three elements corresponds to the three axial stiffnesses and the last three corresponds to the rotational stiffnesses. A single base fixed boundary condition is obtained by rigidly connecting the four base points of the hold down blocks at the bottom of the panel.

The material properties used to model this system is also given in Table 5.1. Here, the properties of the 3M viscoelastic damping polymer at 30^{0} C and 132 Hz have been estimated using reference [111] were considered for the analysis. It should be noted that, 132 Hz is the average frequency of the target modes of the system as described in the following section. It was also considered that, the structure supports an additional mass of 2.0 kg, which accounts for solar cells, harness etc. and this non-structural mass is uniformly distributed over the top surface of the panel. The total mass of the model was 3.04 kg and contain 9240 elements.

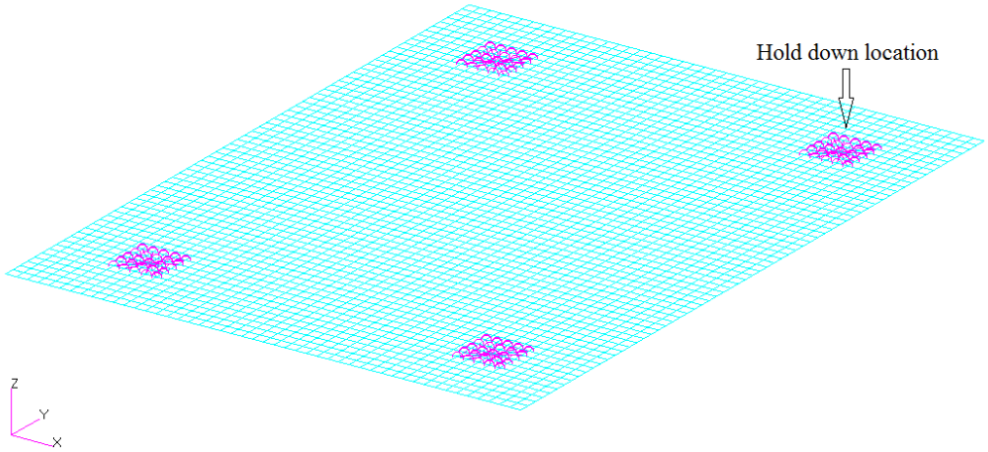

a) FEM and axis system

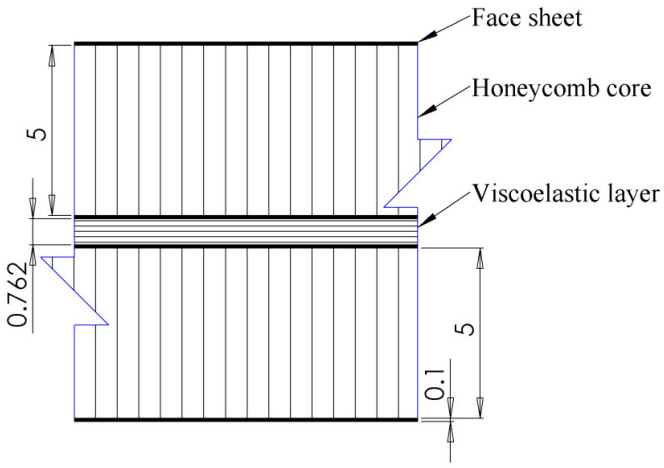

b) Cross sectional view

(All dimensions are in mm)

Fig. 5.2 Model of a honeycomb sandwich panel with viscoelastic core.

5.3 Results and Discussions

An undamped free vibration analysis of the two viscoelastic systems described above was carried out and the model loss factors of the important modes were determined. The loss factor of each mode is determined as the ratio of strain energy of the core to the total strain energy of the corresponding mode [83]. The obtained results for both the systems are given in Table 5.2. In the case of the sandwich plate, the effective mass of modes 2, 3 and 5 in translation were

negligible (less than 10^{-11} kg), hence the first and the fourth modes only are considered as the target modes for the correlation study, which have 2% or more effective mass [95]. These target modes have effective masses of 42.39×10^{-3} kg and 7.36×10^{-3} kg respectively in the Z direction. However, the first and fifth modes of the solar panel model have more than 2% effective mass and hence these modes were taken as the target modes for the system. These target modes have an effective mass of 1.63 kg and 0.55 kg respectively in the Z-direction. As in the previous cases, the results obtained from these FEMs were considered as the nominal or experimental results in the correlation.

Table 5.2 Dynamic characteristics of the nominal FEMs

Mode number	Frequency (Hz)	Loss factor	Structure
1	29.13	0.1496	Sandwich plate
2	44.53	0.1368	
3	68.28	0.1671	
4	70.21	0.1271	
5	82.32	0.1379	
1	72.22	0.0887	Honeycomb sandwich panel
2	93.44	0.0884	
3	131.53	0.0782	
4	164.13	0.1229	
5	191.04	0.1154	

To show the effect of the reduction in the structural response due to the additional damping from the viscoleastic material, a base excitation analysis was conducted using the aluminium sandwich plate. Figure 5.3 shows the absolute acceleration response in the *Z*-direction at the diagonal intersection point of the top face sheet under a 1g sinusoidal exication in the *Z* direction. The figure also shows the response of a bare aluminium plate having the thickness of the total face sheets (4×10^{-4} m) of the viscoelastic system. The damping in the viscoelastic system was taken as the average loss factor of the

two target modes (0.1384) and that in the bare aluminium plate was considered to be 2% critical damping [112]. It can be seen that, there is 12.97 times reduction in the response due to the viscoelastic damping, with a mass penalty of 23.14% (15.22×10^{-3} kg). It should be noted that, here the attention is limited to the correlation of these types of FEMs rather than the optimum design of viscoelastic systems.

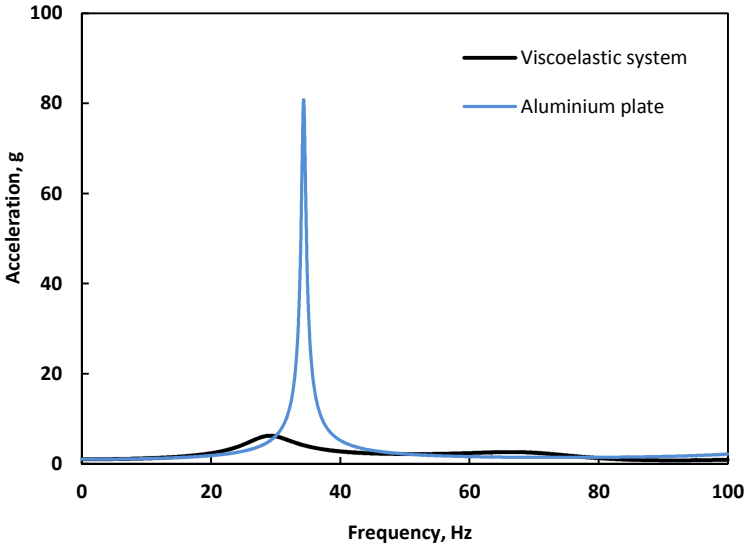

Fig. 5.3 Acceleration response of a bare plate and a viscoelastic damped system.

5.3.1 Standard Correlation Methods and the Modal Loss Factor

To perform the FEM correlation of the viscoelastic systems, twelve intentionally erroneous FEMs were created from the nominal FEMs of the aluminium sandwich plate and the sandwich solar panel by changing the boundary conditions of the structure. Some erroneous models were created by changing both the boundary conditions and the material properties. In the case of solar panel FEM, the hold down stiffness was also varied to generate different FEMs. These changes simulate the common modelling errors. The target modes of different models and the nominal model of the sandwich plate were determined using the 28 nodes in the FEM, which represent the 28 accelerometers in the Z-direction (Fig. 5.1a). The sensor locations are spread across the upper face sheet of the sandwich plate. The obtained target mode shapes using the intentionally erroneous FEMs of the sandwich plate are given in Figs. 5.4-5.5. The modal frequencies and the corresponding loss factors of

the target modes of these erroneous models are given in Table 5.3. In these models, the edge fixed boundary conditions and/or material properties were altered to reduce the stiffness of the system.

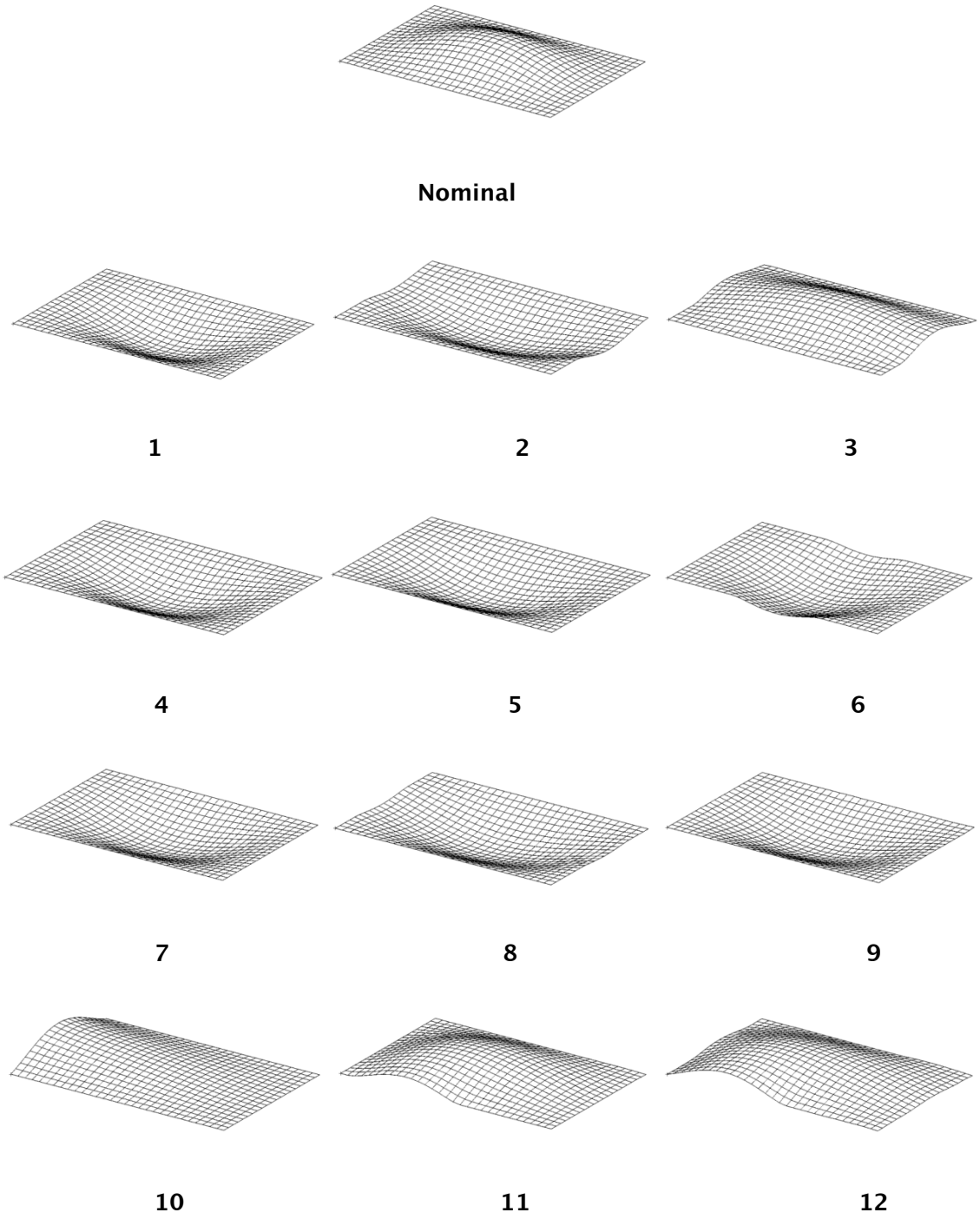

Fig. 5.4 The first target mode of different FEMs of the sandwich plate.

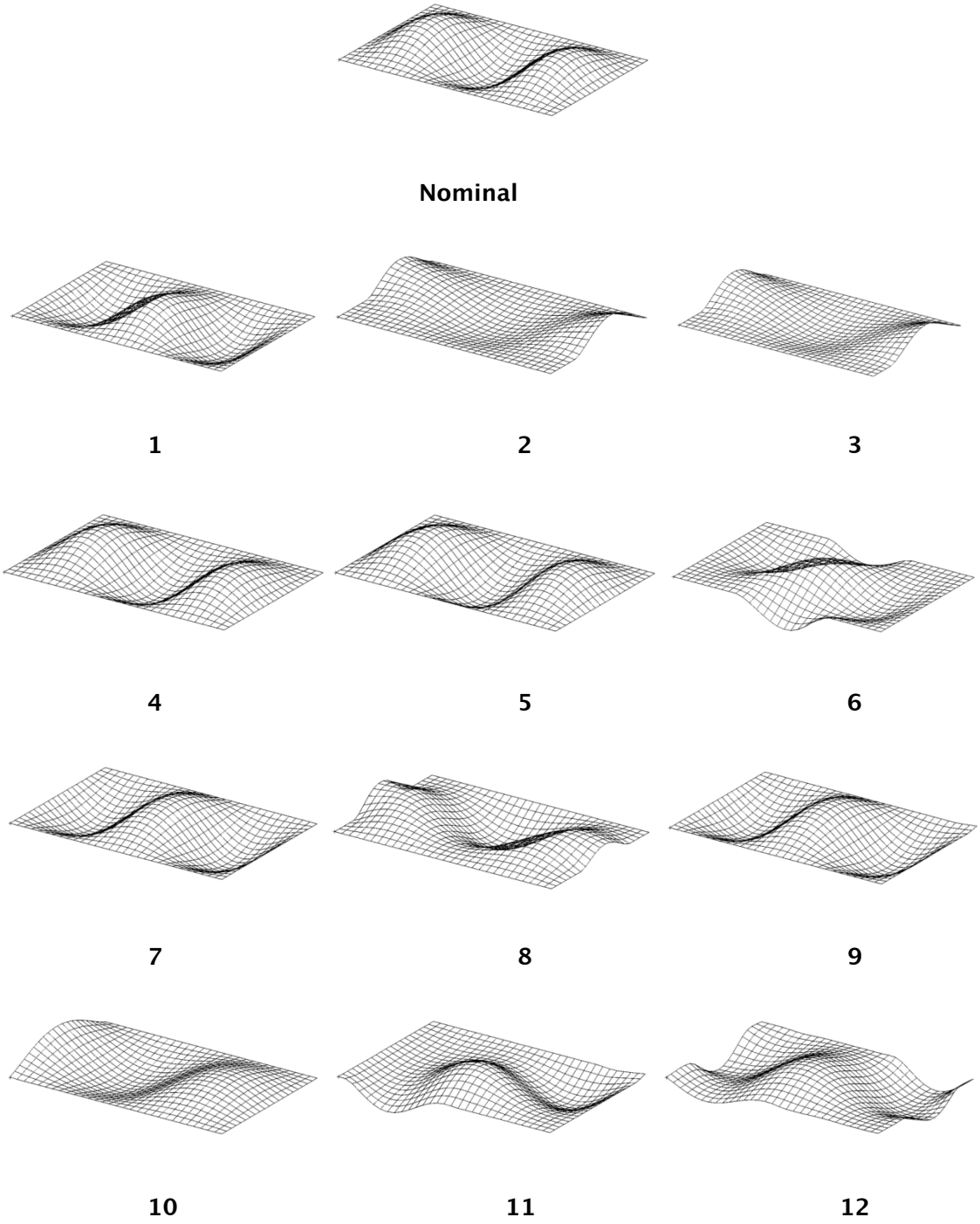

Fig. 5.5 The second target mode of different FEMs of the sandwich plate.

Table 5.3 Dynamic characteristics of different FEMs of the sandwich plate

Model Number	Target mode 1		Target mode 2	
	Frequency (Hz)	Loss factor	Frequency (Hz)	Loss factor
1	27.56	0.1354	68.52	0.1203
2	26.91	0.1514	56.82	0.1024
3	26.37	0.1510	66.96	0.0966
4	26.53	0.1233	67.30	0.1102
5	25.44	0.1118	65.11	0.0904
6	22.12	0.0989	59.16	0.0848
7	23.81	0.0904	62.55	0.0738
8	22.18	0.0826	54.03	0.0700
9	22.70	0.0824	61.14	0.0683
10	19.11	0.0890	47.17	0.0583
11	19.94	0.0729	57.36	0.0629
12	17.81	0.0677	46.35	0.0606

The two target modes of the honeycomb sandwich panel models (solar panel), were also determined using the 28 DOFs in the Z-direction. The nominal and the erroneous target modes (mode 1 and mode 5) are shown in Figs. 5.6-5.7. The modal frequencies of the target mode along with the corresponding loss factors for all the different FEMs are given in Table 5.4.

The viscoelastic system considered in this chapter has more damping than the spacecraft models considered earlier. Therefore, to understand the effect of damping on the MAC, the complex modes of the sandwich plate and the honeycomb sandwich panel were computed using Nastran. For the analysis, the average modal loss factor of the target modes of the respective nominal models was used and the obtained mode shapes were considered as 'true' modes. Similarly, the complex modes of the different FEMs were also calculated using the respective average loss factor of the erroneous FEMs of the two systems. The calculated MAC of the two target modes using the complex modes and the real modes for these systems are given in Tables 5.5-5.6.

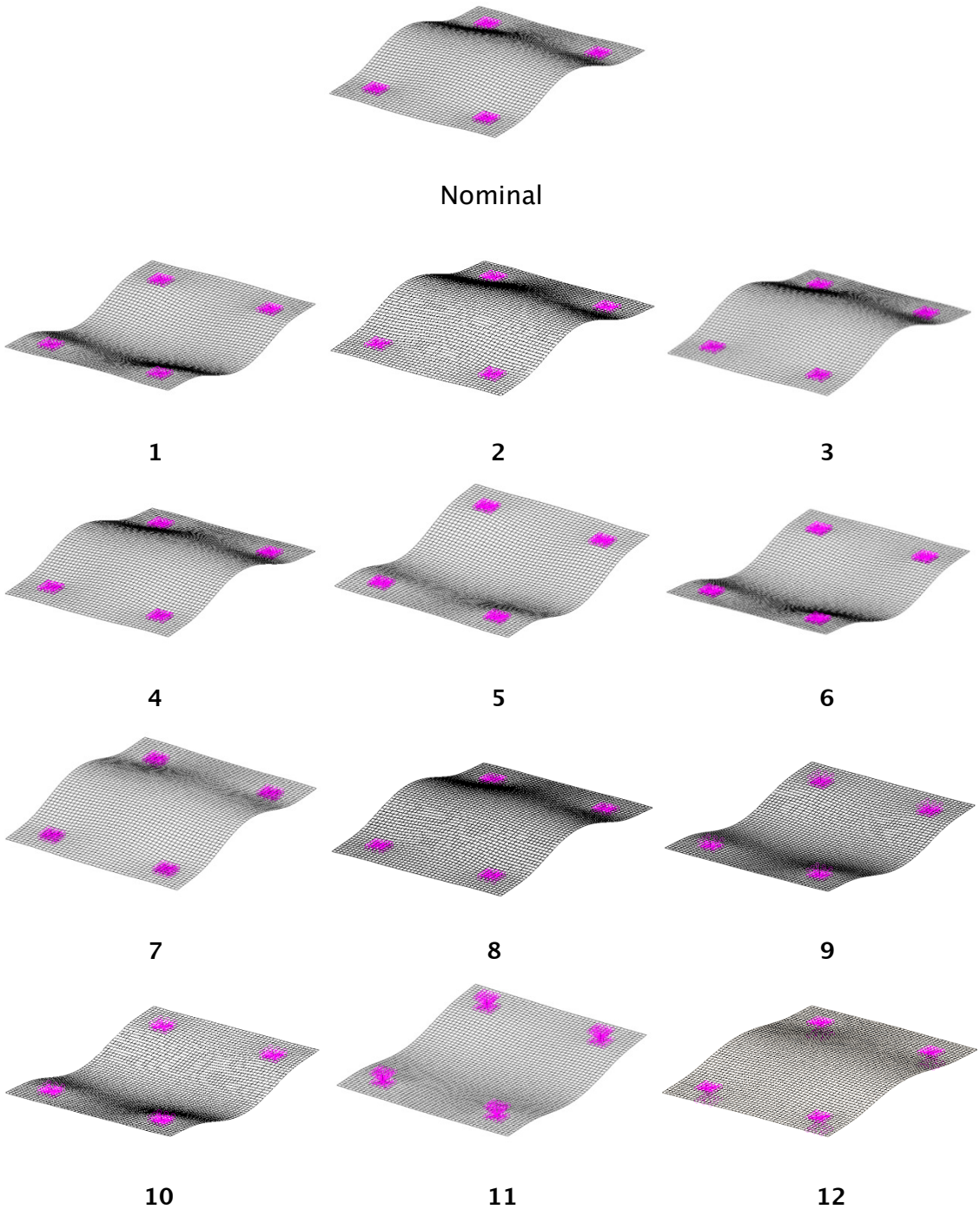

Fig. 5.6 The first target mode of different FEMs of the honeycomb sandwich panel.

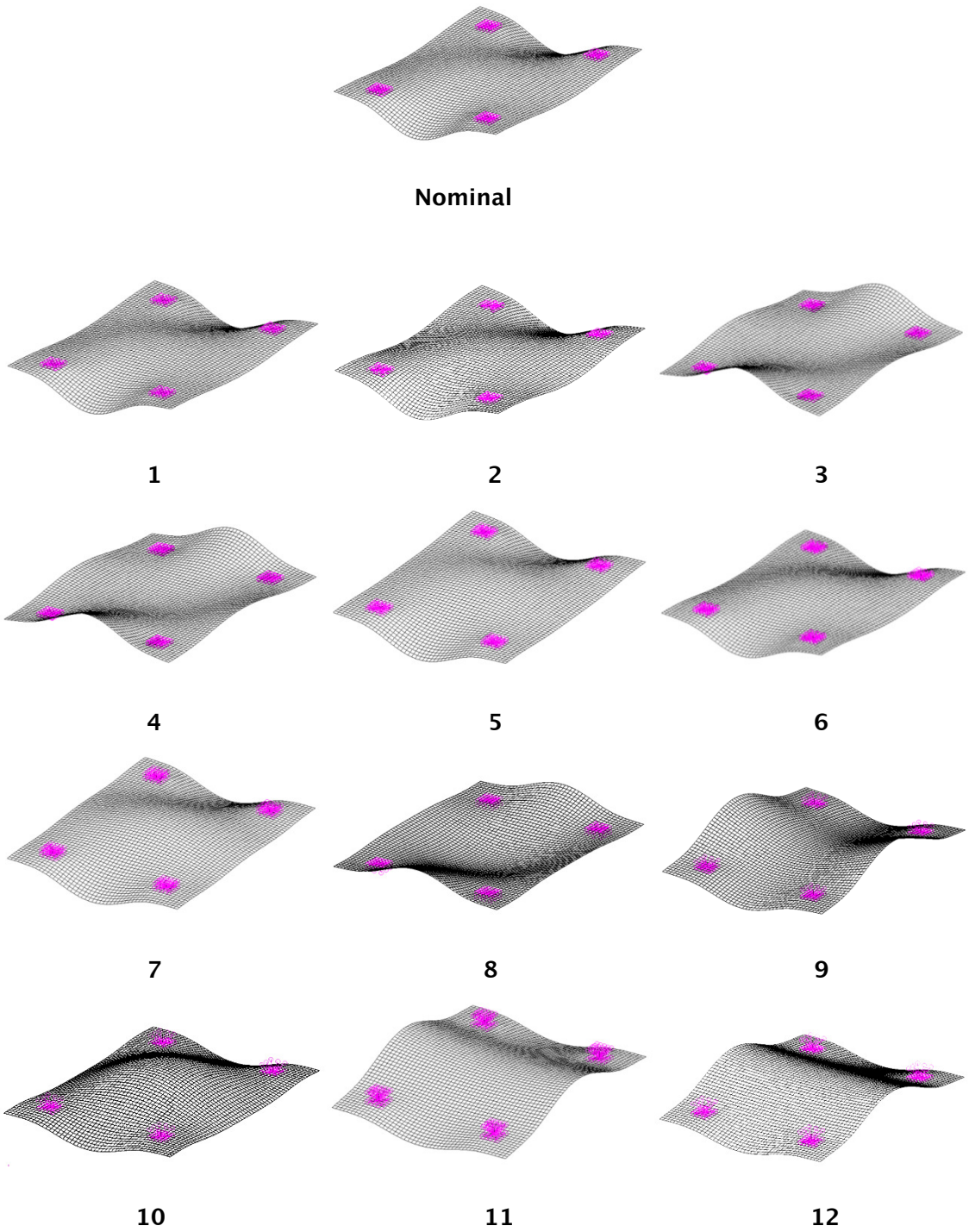

Fig. 5.7 The second target mode of different FEMs of the honeycomb sandwich panel.

Table 5.4 Dynamic characteristics of different FEMs of the honeycomb sandwich panel

Model Number	Target mode 1		Target mode 2	
	Frequency (Hz)	Loss factor	Frequency (Hz)	Loss factor
1	72.22	0.0887	191.04	0.1154
2	71.92	0.0880	189.13	0.1128
3	67.36	0.0802	180.33	0.1041
4	67.86	0.0764	182.65	0.1007
5	67.64	0.0759	181.30	0.0991
6	68.75	0.0803	171.00	0.0855
7	65.38	0.0711	166.98	0.0796
8	66.10	0.0737	155.41	0.0556
9	62.86	0.0653	152.74	0.0614
10	55.73	0.0519	119.66	0.0648
11	59.62	0.0577	139.96	0.0517
12	47.05	0.0315	109.56	0.0562

From the results shown in the Tables 5.5-5.6, it can be seen that there is no significant change in the MAC values when the target modes are computed using the real or the complex modes. This indicates that, the damping did not alter the modes in the considered systems. It should also be noted that, the loss factor for all the models considered was less than 15% in both the systems and hence real modes are sufficient to calculate the MAC for these types of systems. Whence, only real modes are used for the further study.

It was shown in the previous chapters that, neither MAC nor NCO is able to represent the dynamic displacement and the acceleration characteristics of lightly damped complex elastic systems. It is understood that the actual damping in the system is very difficult to model and is usually determined by experimental methods. Here, the damping due to the viscoelastic material alone is considered and attention is limited to its variation with the commonly employed correlation tools MAC and NCO. Although these correlation tools are not suitable for the force response characteristics as shown in the previous chapters, they are extensively used for structural model validation. In the

remaining section, the variation of the MAC and NCO check with the modal loss factor, as the loss factor is the important design factor in the viscoelastic system, is examined.

Table 5.5 Comparison of MAC of the sandwich plate using real and complex modes

Model Number	MAC 1		MAC 2	
	Real Modes	Complex modes	Real Modes	Complex modes
1	0.9914	0.9914	0.9701	0.9698
2	0.9349	0.9348	0.3706	0.3704
3	0.8867	0.8866	0.3607	0.3604
4	0.9878	0.9878	0.9827	0.9826
5	0.9853	0.9852	0.9727	0.9725
6	0.9591	0.9590	0.4494	0.4501
7	0.9933	0.9932	0.9819	0.9818
8	0.9762	0.9761	0.5899	0.5896
9	0.9899	0.9899	0.9750	0.9748
10	0.4576	0.4574	0.1698	0.1696
11	0.8990	0.8988	0.3495	0.3494
12	0.8319	0.8317	0.5205	0.5202

The percentage error in loss factor, $Error_{LS}$ in comparison with the corresponding nominal value has been determined for both the target modes using the equation:

$$Error_{LS} = \left| \frac{LS_{Nom} - LS_{FEM}}{LS_{Nom}} \right| 100 \tag{5.2}$$

where LS_{Nom} is the nominal loss factor of the target mode and LS_{FEM} is the corresponding loss factor obtained from the erroneous FEM.

Table 5.6 Comparison of MAC of the honeycomb sandwich panel using real and complex modes

Model Number	MAC 1		MAC 2	
	Real Modes	Complex modes	Real Modes	Complex modes
1	0.9999	0.9999	0.9993	0.9993
2	0.9986	0.9986	0.9829	0.9829
3	0.9985	0.9985	0.9826	0.9826
4	0.9986	0.9986	0.9831	0.9831
5	0.9952	0.9951	0.9382	0.9381
6	0.9959	0.9959	0.9299	0.9299
7	0.9812	0.9811	0.8117	0.8116
8	0.9862	0.9861	0.7851	0.7850
9	0.9338	0.9337	0.3187	0.3188
10	0.9652	0.9652	0.5451	0.5449
11	0.8452	0.8451	0.4122	0.4122
12	0.8131	0.8131	0.3888	0.3887

The variation of loss factor errors for both the target modes of the sandwich plate with the MAC values of the corresponding modes are shown in Fig. 5.8 and the corresponding plots for the honeycomb sandwich panel (solar panel) models are shown in Fig. 5.9. It should be noted that generally, the model with MAC values above 0.9 are considered as a successful correlation and the model is assumed to be fit for further analysis. From Fig. 5.8, it can be seen that a negligible change in the MAC value (0.005) may result in the abrupt change (as high as 40%) in the loss factor. It can also be seen that occasionally the model with a lower MAC is able to give a better prediction of the loss factor than the model having higher MAC. This can also be observed in the honeycomb sandwich panel (Fig. 5.9). Both of the figures indicate that, even if the FEM pass the standard MAC, the loss factor error can be more than 40%. As in the case of the dynamic characteristics of the spacecraft structure, the MAC fails to correlate the modal loss factor of the viscoelastic system.

This is primarily due to the definition of MAC, which is a vector correlation between the two modes. If the two mode shapes are identical or its shapes are

matched well, then it leads to a MAC correlation value close to one. The results show that, even with the similar modes, the energy dissipated in the viscoelastic core can be changed considerably and hence the error in the prediction of loss factor can be increased. It should also be noted that, MAC values will not be altered with the scaling of the modes, but the strain energy and hence the loss factor will differ for that mode.

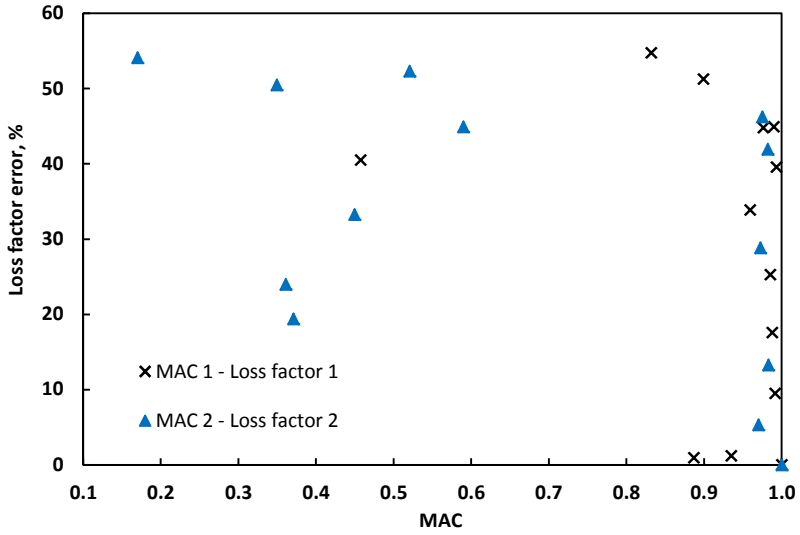

Fig. 5.8 Variation of MAC of the sandwich plate with loss factor error.

The NCO diagonal values of the two target modes and the corresponding loss factor errors for the sandwich plate are shown in Fig. 5.10 and those for the honeycomb sandwich panel are shown in Fig. 5.11. The off-diagonal terms in the NCO matrix for all the models whose diagonal terms are above 0.9 are all less than 0.1. Hence, as per the conventional correlation criteria, all these models pass the correlation check. In Fig. 5.10, many models with NCO values very close to 1 (0.99 or above) also give errors in the loss factor as high as 54%. It can also be observed that some models fail the NCO check but are able to give a better prediction of the loss factor than one which pass the NCO check. From Fig. 5.11, it can be observed that models, which pass the NCO criteria can incorrectly estimate of the loss factor, in this case with as high as 71% error. Similar to MAC, the NCO check also fails to indicate the loss factor of the viscoelastic systems. It is worth mentioning that the MAC and NCO values calculated using all the tri-axial modes (28 tri-axial accelerometers) having 84 DOFs for each target modes also gave the same MAC and NCO

values (up to the third decimal place) as the target modes of the systems considered here have a predominant motion only in the Z-direction.

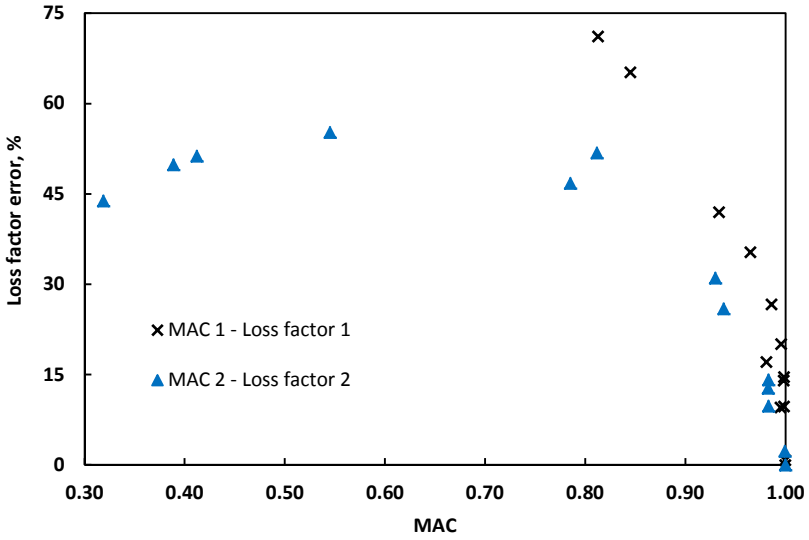

Fig. 5.9 Variation of MAC of the Honeycomb sandwich panel with loss factor error.

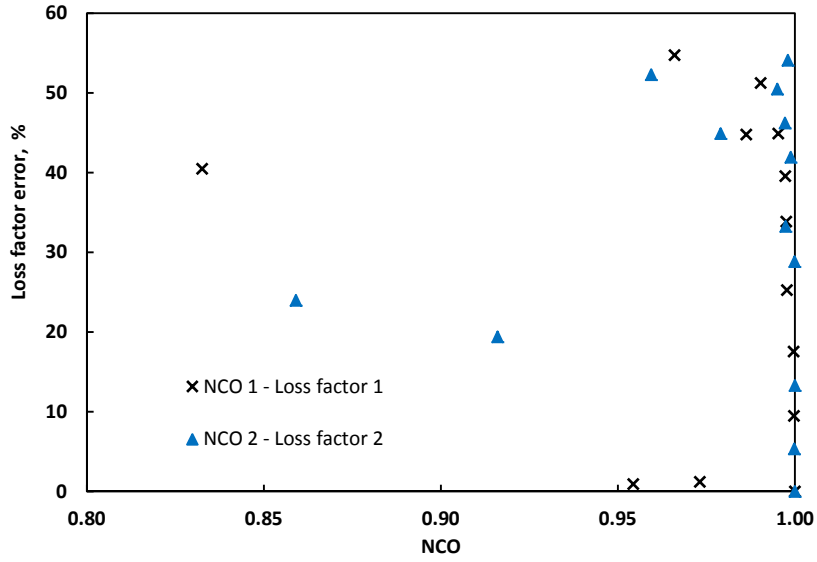

Fig. 5.10 Variation of NCO of the sandwich plate with loss factor error.

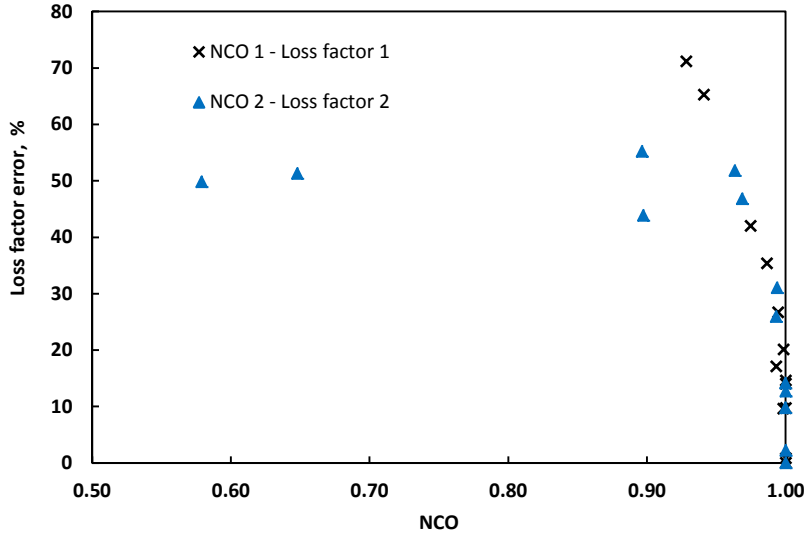

Fig. 5.11 Variation of NCO of the honeycomb sandwich panel with loss factor error.

5.3.2 Base Force Assurance Criterion and the Loss Factor

It was shown that, BFAC can correlate the forced dynamic characteristics of spacecraft under base excitation in a better way than the MAC or NCO [113]. The base force has been determined using a MATLAB [98] program under a harmonic excitation of *1g* in the *Z* direction (Fig. 5.1) at the base node for all the models. The BFAC values for both the sandwich plate and the honeycomb sandwich panel were computed using the nominal and the erroneous transmitted force to the base determined from the corresponding FEMs. As there are two target modes in the frequency band of interest, the average loss factor has been used for this computation. The BFAC in the *Z* direction with average loss factor errors are shown in the Figs. 5.12–5.13. It has been observed that, BFAC in the direction of excitation (*Z* direction) gives good correlation with the average loss factor errors for both the systems. It can also be seen that a definite value of BFAC indicates the possible error in the average loss factor. The base force can also be determined experimentally during the base excitation of the system using a force measuring device.

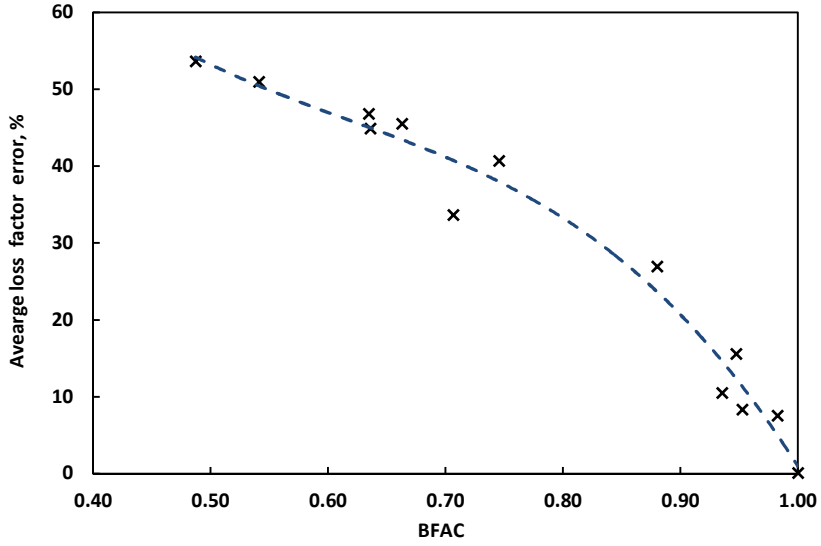

Fig. 5.12 Variation of BFAC of the sandwich plate with average loss factor error.

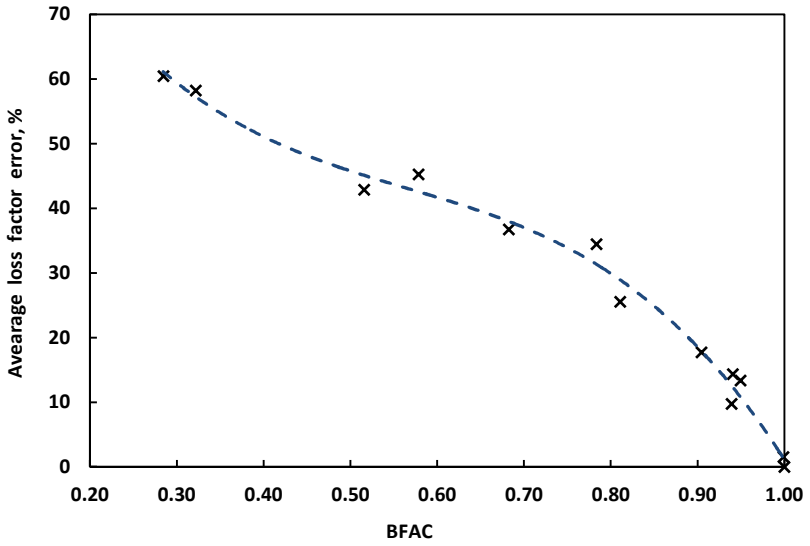

Fig. 5.13 Variation of BFAC of the honeycomb sandwich panel with the average loss factor error.

5.3.3 The Effect of Temperature on the Standard Correlation Methods

In this section, an attempt is made to assess the effect of temperature on the MAC and the NCO check. As the viscoelastic properties change with temperature and frequency, the properties at different temperatures were used to create different FEMs of the sandwich plate and the honeycomb sandwich panel. It is assumed that the variation of viscoelastic properties over the range

of frequencies is negligible and the property at 50 Hz is taken at 10 to 70 °C to create different models of the sandwich plate and the property at 132 Hz is taken at 10 to 70 °C for the honeycomb sandwich panel. The approximate frequency at which the viscoelastic properties chosen for both the systems are based on the average frequency of the two target modes shown in Table 5.2. The analysis also neglected the thermal deformation. The viscoelastic properties at 30 °C were considered for the nominal or base line model as in the earlier case. The required shear modulus of the viscoelastic core was estimated from the catalogue [111] at the required temperatures and shown in Table 5.7. The density and the Poisson ratio of the core were kept the same as the nominal model. The effect of temperature on the material properties of the face sheets is significantly lower than the viscoelastic core in the temperature range used in the analysis and hence neglected.

Table 5.7 Viscoelastic properties at different temperatures

Temperature (°C)	Shear modulus, G (MPa)	
	Frequency=50 Hz	Frequency =132 Hz
10	10.0	15.0
20	4.5	6.5
40	1.0	1.6
50	0.45	0.7
60	0.4	0.55
70	0.3	0.4

To demonstrate the effect of temperature on the viscoelastic properties and hence on the structural response, the base excitation analysis under the 1g excitation in the *Z* direction was performed using the aluminium sandwich plate FEM. Different models have been created using the viscoelastic properties at temperature of 10 to 70 °C. The material loss factor remains constant ($\eta_v = 1$) over the temperature range from 30 to 60 °C whereas it is taken as 0.9 for 20 °C and 70 °C and 0.55 for the 10 °C [111]. The absolute acceleration at the diagonal intersection of the top face sheet was computed in the 0.0–100.0 Hz frequency band for all the models and the absolute acceleration responses

in the Z direction for different temperatures are shown in Fig. 5.14. There are only two modes in the *Z* direction for all the models and, as expected, these two peaks of the acceleration response and the resonance frequencies vary with temperature. The maximum variation of 294% in the acceleration response from the nominal model (30 °C) is observed at 10 °C.

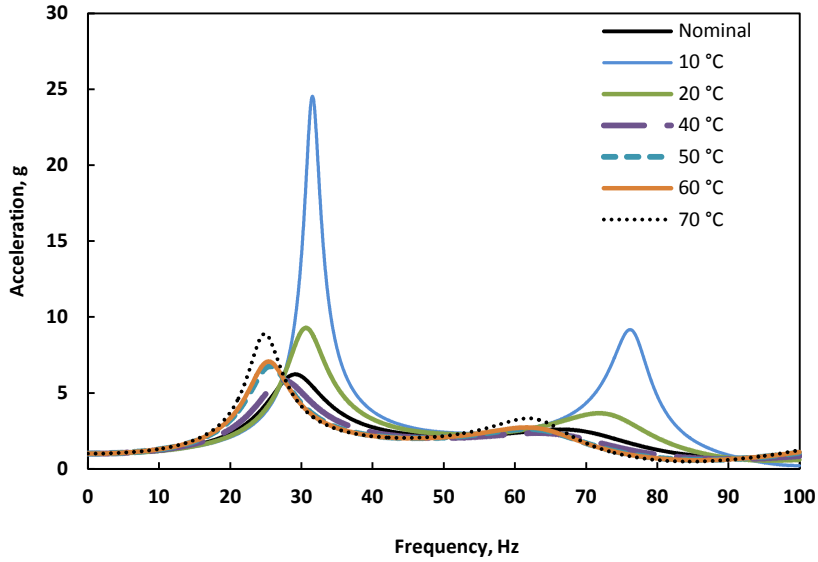

Fig. 5.14 Acceleration response at different temperatures.

Another set of models was created using the nominal FEM of the aluminium sandwich plate by modifying the properties of 50% of the viscoelastic elements with material properties at 10 to 70 °C. All of these elements are selected in such a way that it splits the plate into two halves along the length (X- axis in Fig. 5.1). This simulates that the half part of the structure is under the temperature effect. Then the MAC and the NCO values for both the two target modes were calculated using these models, which correspond to different temperatures, and the variation of the MAC and the NCO values with temperature are shown in Fig. 5.15 and Fig. 5.16 respectively. It can be seen that, practically there is no difference in the NCO values calculated at the different temperatures and there is a maximum of 2% change in the MAC value. Although, the viscoelastic property was highly different for 10 °C, this change is not observed in the MAC or NCO values for this model. This is due to the minor changes in the mode shapes of the models considered. Since only material properties were changed, the difference in the modes from the nominal mode is minimal in this simple structure. Similar results (a maximum

of 2% change in the MAC and negligible change in the NCO values) were obtained for a comparable sandwich plate which has a viscoelastic core material only in 50% of the length (remaining core filled with aluminium) and the viscoelastic material was affected with temperature variation from 10 to 70 °C.

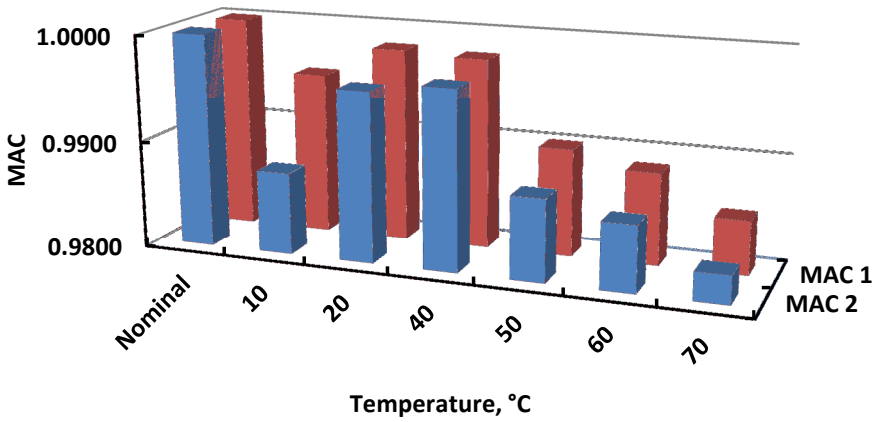

Fig. 5.15 Sandwich plate: MAC at different temperatures.

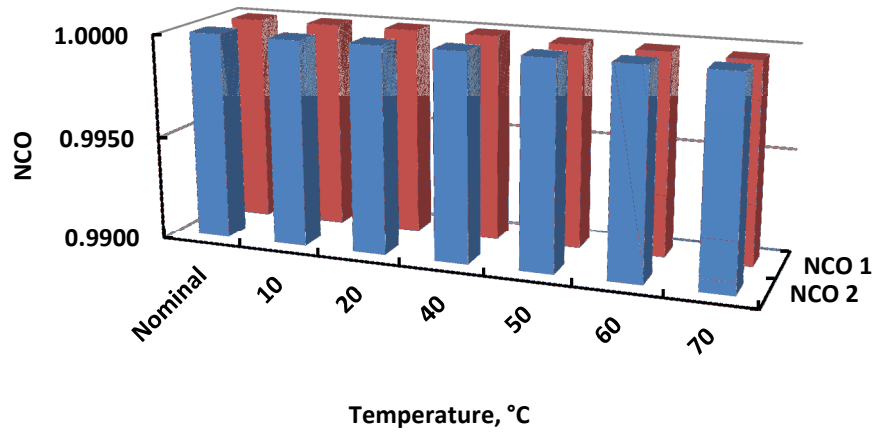

Fig. 5.16 Sandwich plate: NCO at different temperatures.

Using the nominal FEM of the honeycomb sandwich panel, six other FEMs were created by considering the variation of viscoelastic properties with temperature from 10 to 70 °C. The temperature dependent material properties shown in

Table 5.5 were used to create different models. The MAC and NCO values of the two target modes were calculated using these models and the variation of these quality indicators with the temperature is shown in Figs. 5.17–5.18. The MAC of the second target mode varies from 1.0 to 0.64 and the lowest MAC value occurs at 70 °C. As in the sandwich plate models, the NCO values of both the target modes did not vary with temperature. The mass weighting matrix in the NCO correlation nullifies the changes in the mode shape and hence, the changes in the NCO are minimal. It can be concluded that there is no necessity to compute the NCO values for different temperatures for these types of systems, if the uncertainty exists only in the material properties.

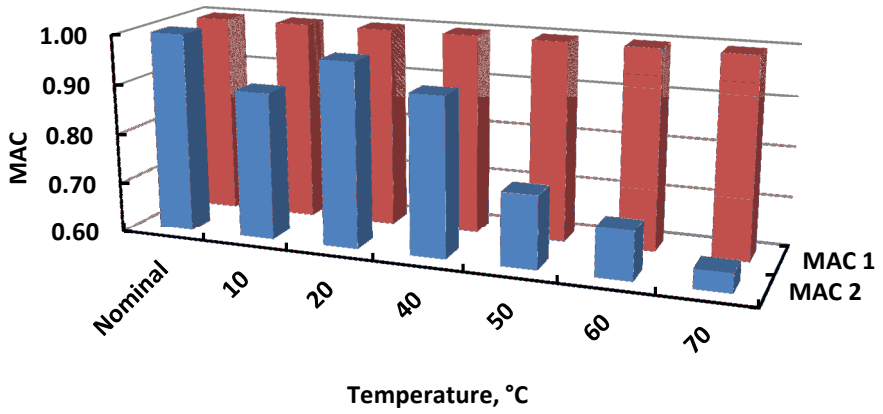

Fig. 5.17 Honeycomb sandwich panel: MAC at different temperatures.

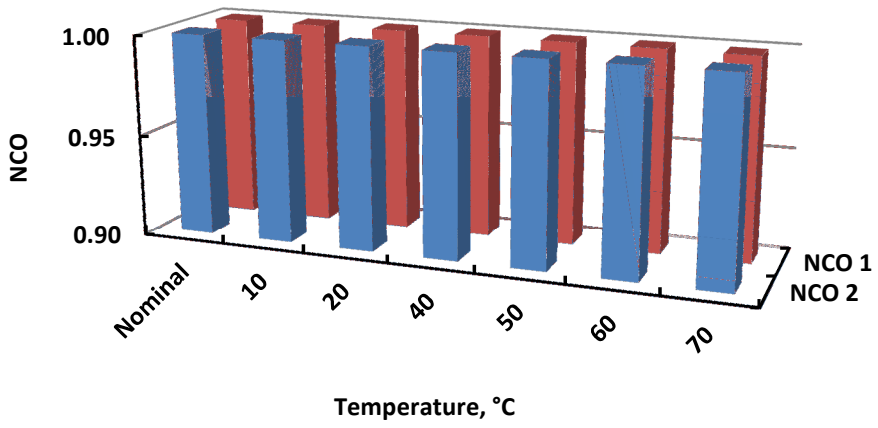

Fig. 5.18 Honeycomb sandwich panel: NCO at different temperatures.

5.4 Summary

Viscoelastic materials have been used for vibration reduction in lightweight aerospace structure with a minimal mass penalty. The modal loss factor is the important parameter in the design of such systems. The effectiveness of using the commonly employed FEM correlation methods; the MAC and NCO check on the prediction of the modal loss factor for a sandwich plate with viscoelastic core and a honeycomb sandwich panel simulating a solar panel have been analysed using intentionally erroneous FEMs. To assess the effect of damping on the MAC, the MAC was computed using the complex modes and it was observed that there is no significant change compared to the corresponding value determined from the real modes. Hence, only normal modes were used for the further analysis. It has been observed that these correlation methods do not give any indication on the capability of the model to predict the loss factor. The base force assurance criterion is found to be more effective than the MAC or NCO check in the prediction of loss factor of such systems. Also, the effect of temperature on the MAC and NCO check were studied using the temperature dependent material property of the viscoelastic material. It has been noted that the maximum variation in the MAC value is only 2% (even when 50% of the structure is under the effect of temperature) for the plate structure and a maximum change of 36% in the MAC value is observed for the sandwich panel. However, the NCO values do not vary (up to the third decimal place) within the temperature band considered (10 to 70 °C) for both the plate and honeycomb sandwich systems. This indicates that, the FEM does not need to be correlated at different temperatures using the NCO criterion if the uncertainty is mainly attributed to the material properties of the systems considered.

The correlation of the second multi-physics system considered is described in the following chapter.

Chapter 6.
Correlation of a Piezoelectric System

6.1 Introduction

Another commonly applied multi-physics system in the aerospace industry consists of piezoelectric patch(es) connected with an electric shunt circuit(s) and then bonded to the host structure for vibration damping [50, 54, 114]. The relevance of these assemblies is that they are mainly used to control the dynamics of the system in which they are embedded. These types of electro-elastic systems have been analysed using the variational principle by different researchers [46, 47]. Tzou and Ye [115] also used the variational principle to define the piezo-thermoelastic finite elements. The finite element model has been effectively used for the dynamic analysis of such coupled system [116-119] and the commercially available software such as ANSYS [120] provides a convenient way to model more complex and practical systems.

In this chapter, the usefulness of the MAC in the validation of multi-physics FEM consisting of an electric circuit and a piezoelectric patch bonded to a titanium plate is evaluated. Titanium material has a low thermal expansion (nearly one fourth of aluminium) and a lower density than steel and hence suitable for the aerospace applications. Here, the coupled FEM has both 'mechanical' and 'electrical' DOFs and an investigation will be carried out to check whether 'mechanical' criterion (MAC) is sufficient to correlate the model. To perform the validation of this coupled FEM, the results obtained from the nominal FEM under the dynamic loading was taken as the experimental data and the results obtained from the different erroneous FEMs were considered to be the analytical data set. The intentionally erroneous models, simulating the modelling inaccuracies, were generated from the nominal FEM by considering the uncertainty in the piezoelectric material properties. It has been observed

that there exists an uncertainty in the piezoelectric material properties and these variations affect the analytical predictions of the coupled system [50, 54]. A review of the finite element formulation of an electric circuit fed piezoelectric system is presented and a new validation method for the multi-physics system has introduced.

6.2 Electro-Elastic System

Piezoelectric materials are used in structural vibration control and in transducer technology. A closed form solution to find the coupled effect of the electrical and structural behaviour is limited to a simple configuration as the equations of piezoelectricity are quite complex. Hence, Allik and Hughes [47] proposed a general method for electro-elastic analysis by incorporating the piezoelectric effect in the finite element formulation as described below.In their formulation, the virtual work density, δW is defined as:

$$\delta W = \delta \boldsymbol{x}^T \boldsymbol{f} - \delta v q \tag{6.1}$$

where $\boldsymbol{x}$ represents the displacement vector, $\boldsymbol{f}$ the mechanical force density, v the electric potential, and q the charge density. Here, it should be noted the analogy between electrical and mechanical variables, that are given in Appendix A3. For a linear material behaviour, the constitutive equations for a piezoelectric crystal can be written as:

$$\boldsymbol{\sigma} = \boldsymbol{C\varepsilon} - \boldsymbol{Pe} \tag{6.2}$$

$$\boldsymbol{d} = \boldsymbol{P}^T \boldsymbol{\varepsilon} + \boldsymbol{De} \tag{6.3}$$

where $\boldsymbol{\sigma}$ denotes the stress tensor, $\boldsymbol{C}$ the elastic stiffness tensor evaluated at a constant electric field, $\boldsymbol{\varepsilon}$ mechanical strain, $\boldsymbol{P}$ the piezoelectric tensor, $\boldsymbol{e}$ the electric field, $\boldsymbol{d}$ the electric flux density, and $\boldsymbol{D}$ the dielectric tensor evaluated at constant mechanical strain. Then the variational principle for the electro-mechanical system can be written as [47]:

$$\iiint_V \left\{ \delta\boldsymbol{\varepsilon}^T \boldsymbol{C}\boldsymbol{\varepsilon} - \delta\boldsymbol{\varepsilon}^T \boldsymbol{P}\boldsymbol{e} - \delta\boldsymbol{e}^T \boldsymbol{P}^T\boldsymbol{\varepsilon} - \delta\boldsymbol{e}^T \boldsymbol{D}\boldsymbol{e} - \delta\boldsymbol{x}^T \bar{\boldsymbol{f}} + \rho\delta\boldsymbol{x}^T \ddot{\boldsymbol{x}} + \delta v\bar{q} \right\} dV - \iint_{S_1} \delta\boldsymbol{x}^T \bar{\boldsymbol{\sigma}} dS + \iint_{S_2} \delta v\bar{q}' dS - \delta\boldsymbol{x}^T \boldsymbol{p} + \delta vQ = \boldsymbol{0} \tag{6.4}$$

where $\bar{\boldsymbol{f}}$ represents the prescribed body force, $\bar{\boldsymbol{\sigma}}$ the surface traction, $\boldsymbol{p}$ the point force, ρ the density of the piezoelectric material, $\bar{q}$ the body charge, $\bar{q}'$ the surface charge and Q the point charge. Also the triple integration is performed over the entire volume, V; S_1 and S_2 represent the sections of the boundary where traction and charge respectively are prescribed.

The electro-elastic relationship for a finite element is arrived by representing the continuous displacement and the electric potential in terms of i nodal parameters using the shape functions $\boldsymbol{N}_x$ and $\boldsymbol{n}_v$[47]. Hence,

$$\boldsymbol{x} = \boldsymbol{N}_x \boldsymbol{x}_i \tag{6.5}$$

$$v = \boldsymbol{n}_v \boldsymbol{v}_i \tag{6.6}$$

where $\boldsymbol{x}_i$ and $\boldsymbol{v}_\mathrm{i}$ are the nodal values of the displacement and the electric potential respectively. Similarly, the prescribed body force, the surface traction, the body charge and the surface charge distributions are expressed through the shape functions and nodal values as:

$$\bar{\boldsymbol{f}} = \boldsymbol{N}_{\bar{f}} \bar{\boldsymbol{f}} \tag{6.7}$$

$$\bar{\boldsymbol{\sigma}} = \boldsymbol{N}_{\bar{\sigma}} \bar{\boldsymbol{\sigma}}_i \tag{6.8}$$

$$\bar{q} = N_{\bar{q}} \bar{\boldsymbol{q}}_i \tag{6.9}$$

$$\bar{q}' = N_{\bar{q}} \bar{\boldsymbol{q}}_i' \,. \tag{6.10}$$

The strains and the electric field can be obtained by differentiating Eq. (6.5) and Eq. (6.6) as:

$$\boldsymbol{\varepsilon} = \boldsymbol{B}_x \boldsymbol{x}_i \tag{6.11}$$

$$\boldsymbol{e} = -\boldsymbol{B}_v v_i \tag{6.12}$$

where $\boldsymbol{B}_x$ and $\boldsymbol{B}_v$ are the strain–displacement matrix and the electric field–displacement matrix respectively. Hence, the variation of strain and electric field are:

$$\delta\boldsymbol{\varepsilon}^T = \delta \boldsymbol{x}_i^T \boldsymbol{B}_x^T \tag{6.13}$$

$$\delta \boldsymbol{e}^T = \boldsymbol{\delta v}_i^T \boldsymbol{B}_v^T \,. \tag{6.14}$$

Similarly, from Eq. (6.5) and Eq. (6.6), the variation of displacement and electric potential can be calculated as:

$$\boldsymbol{\delta x}^T = \boldsymbol{\delta x}_i^T \boldsymbol{N}_x^T \tag{6.15}$$

$$\boldsymbol{\delta} v^T = \boldsymbol{\delta v}_i^T \boldsymbol{n}_v^T \,. \tag{6.16}$$

Substituting Eqs. (6.5)–(6.16) into Eq. (6.4) yields:

$$\begin{aligned}&\iiint_V \left\{\delta \boldsymbol{x}_i^T \boldsymbol{B}_x^T \boldsymbol{C}\boldsymbol{B}_x \boldsymbol{x}_i + \delta \boldsymbol{x}_i^T \boldsymbol{B}_x^T \boldsymbol{P}\boldsymbol{B}_v \boldsymbol{v}_i + \delta \boldsymbol{v}_i^T \boldsymbol{B}_v^T \boldsymbol{P}^T \boldsymbol{B}_x \boldsymbol{x}_i - \delta \boldsymbol{v}_i^T \boldsymbol{B}_v^T \boldsymbol{D}\boldsymbol{B}_v \boldsymbol{v}_i - \delta \boldsymbol{x}_i^T \boldsymbol{N}_x^T \boldsymbol{N}_{\bar{f}} \bar{\boldsymbol{f}}_i\right\} dV \\ &+ \iiint_V \left\{\rho \delta \boldsymbol{x}_i^T \boldsymbol{N}_x^T \boldsymbol{N}_x \ddot{\boldsymbol{x}}_i + \boldsymbol{n}_v \delta \boldsymbol{v}_i N_{\bar{q}} \bar{\boldsymbol{q}}_i\right\} dV - \iint_{S_1} \delta \boldsymbol{x}_i^T \boldsymbol{N}_x^T \boldsymbol{N}_{\bar{\sigma}} \bar{\boldsymbol{\sigma}}_i dS + \iint_{S_2} \boldsymbol{n}_v \delta \boldsymbol{v}_i N_{\bar{q}} \bar{\boldsymbol{q}}_i' dS \\ &- \delta \boldsymbol{x}_i^T \boldsymbol{N}_x^T \boldsymbol{p} \;+\; \boldsymbol{n}_v \delta \boldsymbol{v}_i Q = \boldsymbol{0} \,.\end{aligned} \tag{6.17}$$

For equilibrium, the variation of displacement and electric potential should be zero. Therefore, two equilibrium equations for displacement and electric potential can be written as:

$$\boldsymbol{M}_{xx} \ddot{\boldsymbol{x}}_i + \boldsymbol{K}_{xx} \boldsymbol{x}_i + \boldsymbol{K}_{xv} \boldsymbol{v}_i = \boldsymbol{f}_B + \boldsymbol{f}_S + \boldsymbol{f}_p \tag{6.18}$$

$$\boldsymbol{K}_{vx} \boldsymbol{x}_i + \boldsymbol{K}_{vv} \boldsymbol{v}_i = \boldsymbol{q}_B + \boldsymbol{q}_S + \boldsymbol{q}_p \,. \tag{6.19}$$

Details of the individual terms in the equilibrium equations are given in Appendix A3. After the determination of the nodal values of displacement and the electric potential for an element, stresses and electric flux density at any point in the element can be calculated by substituting strain and electric field into Eqs. (6.2)–(6.3) respectively. Hence,

$$\boldsymbol{\sigma} = \boldsymbol{C}\boldsymbol{B}_x\boldsymbol{x}_i + \boldsymbol{P}\boldsymbol{B}_v\boldsymbol{v}_i \tag{6.20}$$

$$\boldsymbol{d} = \boldsymbol{P}^T\boldsymbol{B}_x\boldsymbol{x}_i - \boldsymbol{D}\boldsymbol{B}_v\boldsymbol{v}_i. \tag{6.21}$$

The system level equation can be formed by the nodal addition of elemental contributions. The assembled equation for the complete system with damping can be written in the matrix form as:

$$\begin{bmatrix} \boldsymbol{M}_{xx} & \boldsymbol{0} \\ \boldsymbol{0} & \boldsymbol{0} \end{bmatrix}\begin{Bmatrix} \ddot{\boldsymbol{x}} \\ \ddot{\boldsymbol{v}} \end{Bmatrix} + \begin{bmatrix} \boldsymbol{C}_{xx} & \boldsymbol{0} \\ \boldsymbol{0} & \boldsymbol{0} \end{bmatrix}\begin{Bmatrix} \dot{\boldsymbol{x}} \\ \dot{\boldsymbol{v}} \end{Bmatrix} + \begin{bmatrix} \boldsymbol{K}_{xx} & \boldsymbol{K}_{xv} \\ \boldsymbol{K}_{vx} & \boldsymbol{K}_{vv} \end{bmatrix}\begin{Bmatrix} \boldsymbol{x} \\ \boldsymbol{v} \end{Bmatrix} = \begin{Bmatrix} \boldsymbol{f}_T \\ \boldsymbol{q}_T \end{Bmatrix} \tag{6.22}$$

where $\boldsymbol{C}_{xx}$ is the mechanical damping matrix, $\boldsymbol{f}_T$ and $\boldsymbol{q}_T$ are the total applied force and charge respectively. It should be noted that, all the nodes on one electrode surface of the piezoelectric patch will have identical potential. This indicates that there is a single potential DOF per electrode of piezoelectric patch.

6.2.1 Free Vibration Analysis

A piezoelectric patch can be configured either in an open circuit or in a closed circuit form. The open circuit configuration is also known as the sensor configuration and the potential difference between the electrodes depends on the mechanical load acting on the system. Let the harmonic displacement and electric potential be given by [50]:

$$\boldsymbol{x} = \boldsymbol{x}_o e^{i\omega t} \tag{6.23}$$

$$\boldsymbol{v} = \boldsymbol{v}_o' e^{i\omega t} \tag{6.24}$$

where ω is the circular frequency and t represents the time. For harmonic motion, Eq. (6.22) can be re-written for the undamped free vibration analysis as:

$$\begin{bmatrix} \boldsymbol{K}_{xx} - \boldsymbol{\omega}^2\boldsymbol{M}_{xx} & \boldsymbol{K}_{xv} \\ \boldsymbol{K}_{vx} & \boldsymbol{K}_{vv} \end{bmatrix}\begin{Bmatrix} \boldsymbol{x}_o \\ \boldsymbol{v}_o' \end{Bmatrix} e^{i\omega t} = \boldsymbol{0}. \tag{6.25}$$

The lower part of this equation gives:

$$\boldsymbol{v} = -\boldsymbol{K}_{vv}^{-1}\boldsymbol{K}_{vx}\boldsymbol{x}\,. \tag{6.26}$$

Substituting the value of electric potential into upper part of Eq. (6.25) yields:

$$((\boldsymbol{K}_{xx} - \boldsymbol{K}_{xv}\boldsymbol{K}_{vv}^{-1}\boldsymbol{K}_{vx}) - \boldsymbol{\omega}_o^2\boldsymbol{M}_{xx})\boldsymbol{\phi}_o = \boldsymbol{0}. \tag{6.27}$$

This is the equation of the generalised eigenvalue problem. Here, ω_o is the modal frequency of the open circuit configuration and $\boldsymbol{\phi}_o$ is the corresponding mode shape. In the case of a short circuit configuration, $\boldsymbol{v}_o'$ is zero, hence, the eigenvalue equation reduces to:

$$(\boldsymbol{K}_{xx} - \boldsymbol{\omega}_s^2\boldsymbol{M}_{xx})\boldsymbol{\phi}_s = \boldsymbol{0} \tag{6.28}$$

where ω_s is the modal frequency of the closed circuit configuration and $\boldsymbol{\phi}_s$ is the corresponding mode shape.

6.2.2 Response Analysis of the Piezoelectric Structure under Harmonic Excitation

The response of the system under harmonic excitation can be computed by solving the time dependent equation of motion given in Eq. (6.22). Due to the presence of damping, there will be a phase shift. Hence, the displacement and electric field can be expressed as [54]:

$$\boldsymbol{x}(t) = \boldsymbol{x}e^{-i\Omega t+\varphi_1} \tag{6.29}$$

$$\boldsymbol{v}(t) = \boldsymbol{v}e^{-i\Omega t+\varphi_2} \tag{6.30}$$

where Ω represents the forcing frequency and φ_1 and φ_2 denote the phase shift. Similarly, the applied force and charge are represented by:

$$\boldsymbol{f}_T(t) = \boldsymbol{f}_T e^{-i\Omega t+\varphi_3} \tag{6.31}$$

$$\boldsymbol{q}_T(t) = \boldsymbol{q}_T e^{-i\Omega t+\varphi_4} \tag{6.32}$$

where φ_3 and φ_4 denote the phase shift. Incorporating Eqs. (6.29)–(6.32) in to Eq.(6.22) gives:

$$\begin{bmatrix} \boldsymbol{K}_{xx} - i\Omega \boldsymbol{C}_{xx} - \Omega^2 \boldsymbol{M}_{xx} & \boldsymbol{K}_{xv} \\ \boldsymbol{K}_{vx} & \boldsymbol{K}_{vv} \end{bmatrix} \begin{Bmatrix} \boldsymbol{x} \\ \boldsymbol{v} \end{Bmatrix} = \begin{Bmatrix} \boldsymbol{f}_T \\ \boldsymbol{q}_T \end{Bmatrix}. \tag{6.33}$$

It can be noted that when the natural frequency of the structure hosting the piezoelectric system coincides with the forcing frequency, this leads to the peak harmonic response.

6.2.3 Analysis of the Piezoelectric Structure Connected with an Electric Shunt Circuit

In order to have compatibility between the piezoelectric formulation and the standard electric circuit equation, the latter generally follows Kirchoff's current law; the electric charge balance at each node is enforced [116]. Thus, the circuit elements namely, capacitor (C), resistor (R) and inductor (L) were represented by an equivalent capacitance matrix form. For a harmonic analysis, the capacitor is represented by the equation [54, 121]:

$$C \begin{bmatrix} 1 & -1 \\ -1 & 1 \end{bmatrix} \begin{Bmatrix} v_1 \\ v_2 \end{Bmatrix} = \begin{Bmatrix} 0 \\ 0 \end{Bmatrix}. \tag{6.34}$$

A resistor is expressed for a harmonic analysis as:

$$i\Omega \left(-\frac{1}{\Omega^2 R} \right) \begin{bmatrix} 1 & -1 \\ -1 & 1 \end{bmatrix} \begin{Bmatrix} v_1 \\ v_2 \end{Bmatrix} = \begin{Bmatrix} 0 \\ 0 \end{Bmatrix} \tag{6.35}$$

and an inductor by:

$$\left(-\frac{1}{\Omega^2 L} \right) \begin{bmatrix} 1 & -1 \\ -1 & 1 \end{bmatrix} \begin{Bmatrix} v_1 \\ v_2 \end{Bmatrix} = \begin{Bmatrix} 0 \\ 0 \end{Bmatrix} \tag{6.36}$$

where v_1 and v_2 are the electric potential DOFs at the nodes where these circuit elements are connected. It is worth mentioning that, these equations can be readily added to Eq. (6.22) to couple the electric circuit effect to the piezoelectric structure. Alternately, when a resonant LR shunt is serially connected to the piezoelectric patch, using the standard form of the homogeneous equation for the series RLC circuit ($LC\ddot{v} + RC\dot{v} + v = 0$), the Eq. (6.22) can also be written as:

$$\begin{bmatrix} \boldsymbol{M}_{xx} & 0 \\ 0 & LC \end{bmatrix} \begin{Bmatrix} \ddot{\boldsymbol{x}} \\ \ddot{v} \end{Bmatrix} + \begin{bmatrix} \boldsymbol{C}_{xx} & 0 \\ 0 & RC \end{bmatrix} \begin{Bmatrix} \dot{\boldsymbol{x}} \\ \dot{v} \end{Bmatrix} + \begin{bmatrix} \boldsymbol{K}_{xx} & \boldsymbol{K}_{xv} \\ \boldsymbol{K}_{vx} & \boldsymbol{K}_{vv} \end{bmatrix} \begin{Bmatrix} \boldsymbol{x} \\ v \end{Bmatrix} = \begin{Bmatrix} \boldsymbol{f}_T \\ 0 \end{Bmatrix} \quad (6.37)$$

where C is the capacitance of the piezoelectric patch and $\boldsymbol{v}$ is the potential across the piezoelectric electrodes.

6.2.4 Configuration and Modelling of the Piezoelectric System

To study the correlation aspects of a multi-physics system, a piezoelectric patch bonded onto the upper face of a titanium plate was considered and the geometry of the configuration is shown in Fig. 6.1. Both the plate and piezoelectric patch have a rectangular shape with a uniform thickness of 0.002 m and 3.8×10^{-4} m respectively. A resistor and inductor are connected in series between the top and the bottom electrodes of the piezo electric patch to dissipate the vibration energy of the system. A similar problem has been analysed by Min *et al.* [54] but here the focus is to study the correlation aspects of the multi-physics system rather than the vibration control.

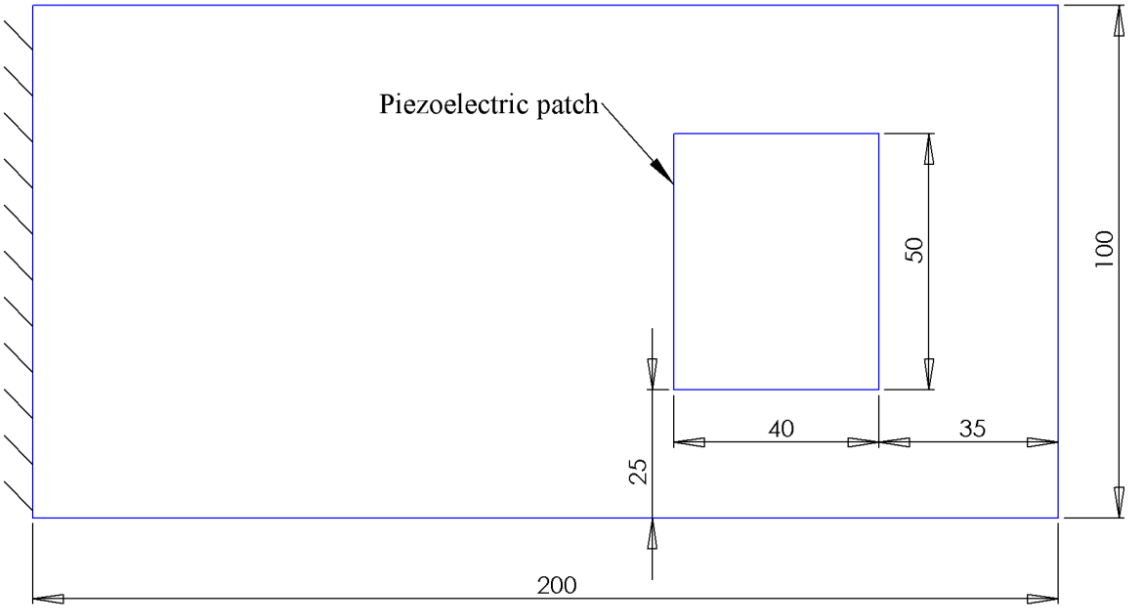

(All dimensions are in mm)

Fig. 6.1 Configuration of the piezoelectric patch on the titanium plate.

The finite element model of the piezoelectric system attached with a resistor and inductor in series is shown in Fig. 6.2. The piezoelectric patch is placed in such a way that it can reduce the dynamic response due to the third bending mode of the structure when it is excited by a harmonic force ($\boldsymbol{f}$) at the fixed end in the *Z* direction as shown in Fig. 6.2. The finite element modelling and the analysis were conducted using ANSYS multi-physics software. The titanium plate was modelled using 20-node SOLID186 elements and the element has three displacement degrees of freedom per node [122]. The piezoelectric patch was modelled using SOLID226 elements with the material property of PZT-5. The SOLID226 is a 20-node element with piezoelectric capability and there are four degrees of freedom per node and the additional fourth degree of freedom is the voltage. The resistor and inductor are modelled using CIRCU94 elements. These elements are capable of simulating the linear electric circuits and can be directly coupled to the piezoelectric elements [123]. The total number of elements used in this model is 883.

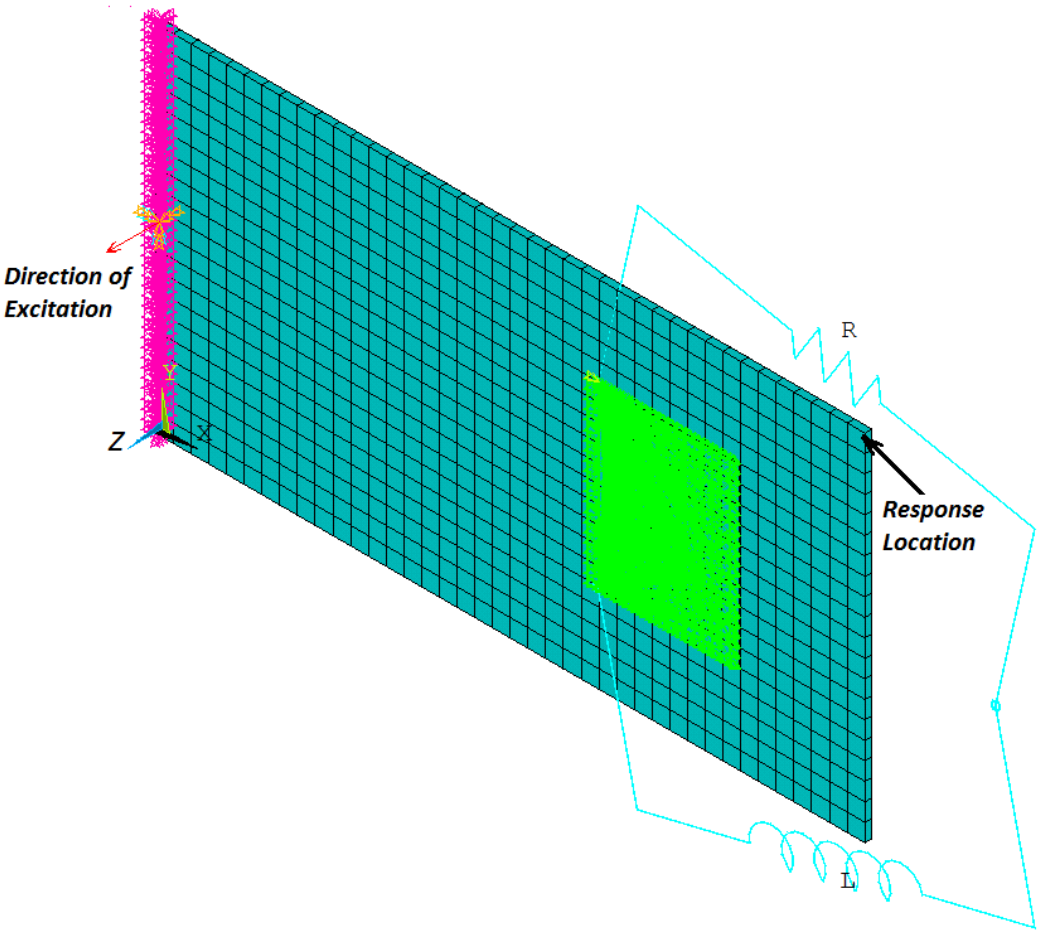

Fig. 6.2 FEM of the shunted piezoelectric system.

The properties of titanium and PZT-5 used in the analysis are shown in Table 6.1 [54]. The poling direction for the piezoelectric material is chosen as the thickness direction of the patch. It should be noted that, ANSYS required material properties in a specific format and hence, the standard material properties need to be converted using stress-strain relationships before using it in the analysis as specified in the coupled-field analysis guide of ANSYS [123].

Table 6.1 Material properties

Property	Material	
	PZT-5	Titanium
Young's modulus (G Pa)	$E_{11} = E_{22} = E_{33} = 77$	E =104.83
Poisson's ratio	$\nu_{12} = \nu_{23} = \nu_{13} = 0.3$	ν =0.3
Density (kg/m^3)	$\rho = 7700$	$\rho = 4428.83$
Shear modulus (G Pa)	$G_{12} = G_{23} = G_{13} = 29.62$	
Piezoelectric coefficients (10^{-12} m/Volt)	$d_{31} = d_{32} = -130$ d_{33} =330 $d_{24} = d_{15}$ =327	
Electric permittivity	${\epsilon_{11}}/{\epsilon_0} = {\epsilon_{22}}/{\epsilon_0} = {\epsilon_{33}}/{\epsilon_0} = 1300$	

(ϵ_0 =8.85x10^{-12} Farad/m; electric permittivity of vacuum)

6.3 Results and Discussions

6.3.1 Dynamic Response of the Piezoelectric System

The multi-physics system has been analysed under the *0.1g* base excitation in the *Z* direction (Fig. 6.2) without any electrical circuits and the bottom electrode of the piezoelectric patch, which interfaces with the plate, in grounded condition. Here, *g* denotes the acceleration due to gravity. The critical damping ratio was taken as 7.8x10^{-4} [54] and the acceleration response at the tip of the cantilever during the third bending mode is shown in Fig. 6.3.

The absolute peak acceleration has an amplitude of 27.43 g and occurs at 724.6 Hz. Then the piezoelectric electrodes are attached with a resistance (1 Ohm) and an inductor (0.65 H). The dynamic response at the tip with these electrical components is shown in Fig. 6.4. The first peak in this figure is the electrical resonance that occurs at 639.7 Hz. These typical values of the electrical parameters are chosen to show a distinct electrical resonance mode. It can be observed that there is a slight decrease in the tip acceleration (7.6%) during the third bending mode compared to the system which does not have any electrical circuits. If further reduction in the peak acceleration response is required, the electrical circuit parameters can be tuned. One such option, with R=1000 Ohm and L=0.65 H gives a tip acceleration as low as 4.4 g during the third bending mode for the same base excitation. This response plot is shown in Fig. 6.5.

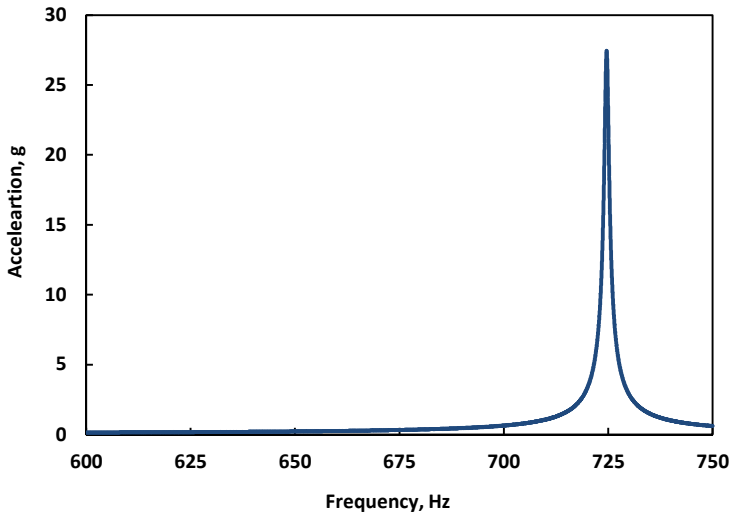

Fig. 6.3 Acceleration response of the tip with the piezoelectric patch.

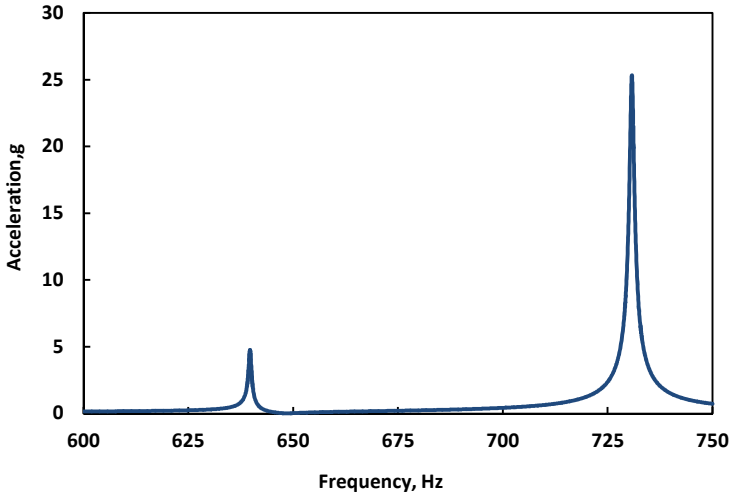

Fig. 6.4 Tip acceleration with electrical circuit (R=1 Ohm, L=0.65 H).

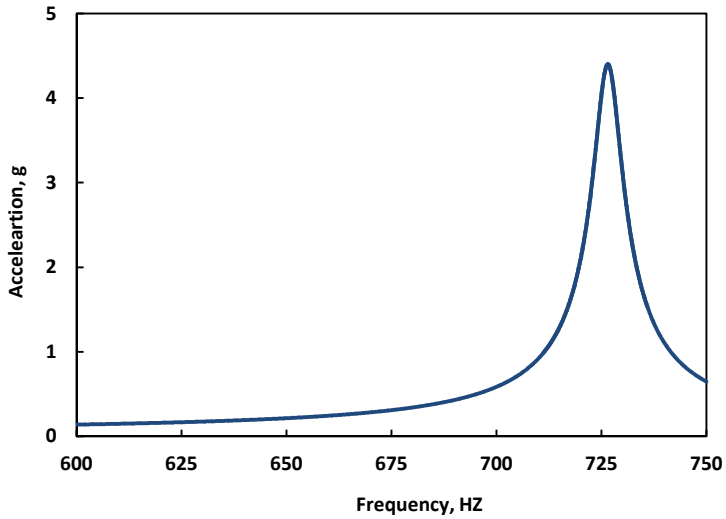

Fig. 6.5 Tip acceleration with the tuned electrical circuit (R=1000 Ohm, L=0.65 H).

6.3.2 Finite Element Model Correlation

Finite element models of the conventional structure can be validated using the MAC [6] or NCO check. To understand, how the FEM of the piezoelectric system performs under the dynamic loading when it possess a certain value of the MAC, a study has been carried out using the different FEMs generated from the nominal FEM. It is understood that MAC is not a criterion for the response analysis but it is the most popular correlation method. The FEM generated

using the material property shown in Table 6.1 is considered as the nominal model and the obtained results were taken as the experimental or nominal results for the correlation study. It is understood that, there is a good amount of uncertainty in the properties of piezoelectric material [50, 54] and hence, ten different intentionally erroneous FEMs were generated from the nominal FEM by varying all the material properties of the system from 0.5% to 25.0% of the nominal value shown in Table 6.1. The percentage changes in the material properties for different erroneous models were chosen as 0.5, 0.75, 1.0, 2.5, 5.0, 7.5, 10.0, 15.0, 20.0 and 25.0. Geometry, boundary condition and the electrical shunt circuit (R=1 Ohm, L=0.65 H) were kept constant throughout.

Tip acceleration, tip displacement and the peak current in the electrical circuit were computed in the frequency range of 5.0–750.0 Hz during the base excitation of the system. As in the previous case, the input acceleration was $0.1g$ in the Z-direction. The percentage error in the absolute acceleration, $Error_{Accn}$ for the third bending mode were calculated with reference to the corresponding nominal values, a_{Nom} as:

$$Error_{Accn} = \left| \frac{a_{Nom} - a_{FEM}}{a_{Nom}} \right| 100 \tag{6.38}$$

where, a_{FEM} is the absolute value of the peak acceleration obtained from the erroneous FEM. Similarly, the absolute tip displacement error for the third bending mode and the peak current error in the shunt circuit were also computed.

The MAC [6] can be calculated using the experimental/nominal mode and FEM mode. For the computation of the MAC, the third bending mode has been considered and the variation of tip acceleration error with the MAC is shown in Fig. 6.6. It has been observed that, a model with a MAC value very close to 1 (0.998) also give high error (say 20%) in the acceleration response. In addition to that, models with negligible difference (0.001) in MAC values may also give different levels of acceleration errors. Here, the change in the mode shape is minimal (hence MAC close to 1) because the variations in the FEMs are only in the material properties. However, variations in the material properties change the frequency of vibration and the effective mass of the mode and hence the response. Although Fig. 6.6 shows some correlation between the MAC and the

tip acceleration, it should be noted that practically it will be very difficult to determine the very small changes (in the order of 10^{-3}) in the MAC values. Thus, effectively there is no correlation between the MAC and the model capability to predict the acceleration response [124]. Similar results were also observed in the spacecraft structure as shown in chapter 4. It should also be noted that, generally model with MAC > 0.9 is considered to be a successful model [9, 10], but here it fails to represent the acceleration response within the limit (e.g., < 5% error).

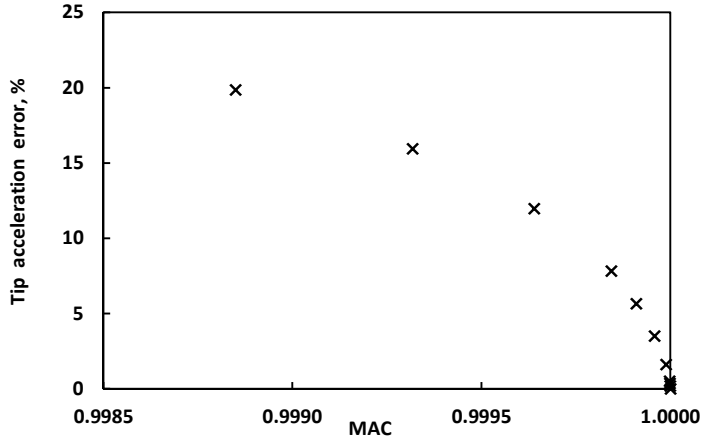

Fig. 6.6 Variation of tip acceleration error with the MAC.

The variation of tip displacement error with MAC of the third bending mode is shown in Fig. 6.7, whereas Fig. 6.8 shows the variation of peak current error with the MAC. As in the case of acceleration error, neither the dynamic displacement nor the electric current shows any useful correlation with the MAC value. Also for the similar MAC values (maximum difference in the order of 10^{-3}), error in the displacement or current may drastically change. Hence, MAC is not a good correlation tool to assess the FEM capability to predict the dynamic characteristics of the multi-physics system. The MAC values very close to 1 are primarily due to the nature of the models considered in this study, which are generated by changing the material properties and the structure is a simple cantilever. Hence, the change in the mode shape is negligible compared to the nominal mode. However, the purpose here is to show that there are FEMs, which can easily pass the MAC, but fail in the prediction of dynamic characteristics of the multi-physics system.

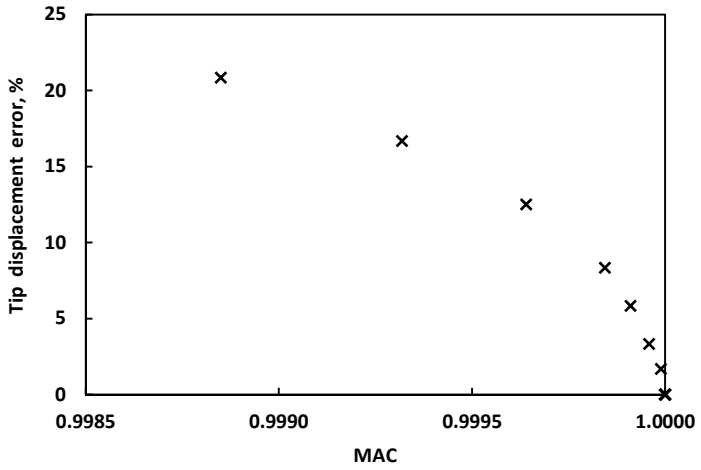

Fig. 6.7 Variation of tip displacement error with the MAC.

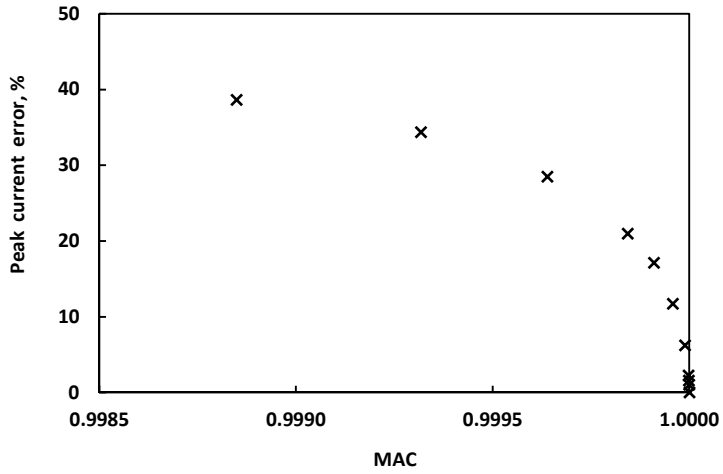

Fig. 6.8 Variation of peak current error with the MAC.

6.3.3 Current Assurance Criterion

It has been shown in the previous section that the conventional correlation method, the MAC, fails to correlate the dynamic characteristics of the multi-physics system, as it is a pure vector correlation of two deformed shapes. The variation of nominal value of the current with frequency, when the piezoelectric structure connected with the electric circuit is excited with a harmonic input (0.1 g) at the base is shown in Fig. 6.9. The maximum current in the circuit occurs during the electrical resonance and in this chosen configuration at 639.7 Hz. The other three peaks in the figure correspond to the first three bending modes of the structure, which occur at 39.4 Hz, 255.1 Hz and 730.8

Hz respectively. It can be noted that, unlike acceleration or displacement, current in the shunt circuit does not depend on the location and will be unique for each circuit. However, current in the circuit varies with the frequency and the current values in the frequency range contain important information about the dynamics of the system. Using this property, in line with the base force assurance criterion, a current assurance criterion is defined as:

$$CAC = \frac{\left(I_{Exp}^{T} I_{FEM}\right)^{2}}{\left(I_{Exp}^{T} I_{Exp}\right)\left(I_{FEM}^{T} I_{FEM}\right)} \tag{6.39}$$

where, I_{Exp} and I_{FEM} are the experimental and the analytically calculated absolute current values in the electrical circuit. It should be noted that both of these quantities are functions of frequency and all the values of current in the frequency domain of interest need to be included for the CAC computation. This quality indicator varies from 0.0 to 1.0 where 1.0 indicates a perfect correlation between the experimental and the analytical result. If there are a number of piezoelectric patches connected with separate electrical networks or there are a number of shunt circuits in parallel, then for such different current values, separate CAC need to be evaluated for the purpose of correlation. During dynamic testing, the value of the current can be measured for the frequency range of interest.

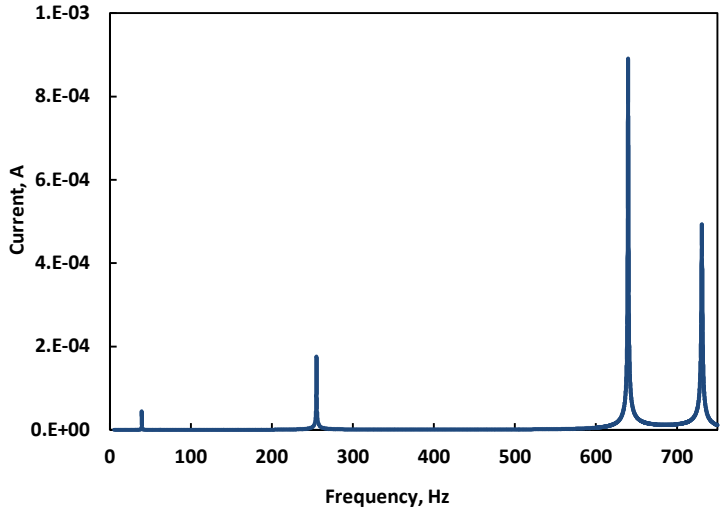

Fig. 6.9 Variation of current with frequency (R=1 Ohm, L=0.65 H).

As in the earlier case, the current obtained from the nominal FEM is taken as the experimental value and those obtained from the different erroneous FEM generated by varying the material properties were taken as the analytical values. The CAC for the different FEMs were calculated in the frequency band of 5.0–750 Hz and the variation of CAC with the absolute tip acceleration error for those models is shown in Fig. 6.10. It can be seen that, for a specific value of CAC, the error in the acceleration response is unique. Hence, CAC can be used as a quality indicator for the acceleration response of this type of system.

The variation of tip dynamic displacement error with CAC is shown in Fig. 6.11 and Fig. 6.12 shows the CAC variation with the error in the peak current in the circuit; both of these quantities correlate well with CAC. For the numerical example analysed here, a CAC value greater than 0.2 always assures that the error in the acceleration, dynamic displacement and the peak current is within 2%, being an acceptable value for the most practical problems.

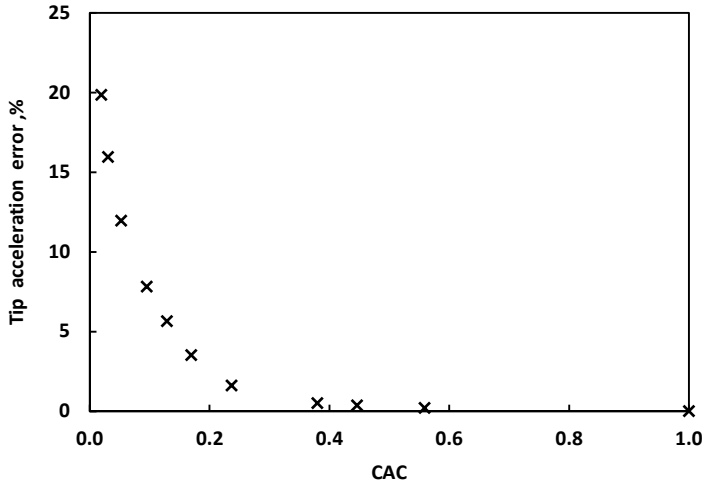

Fig. 6.10 Variation of tip acceleration error with the CAC.

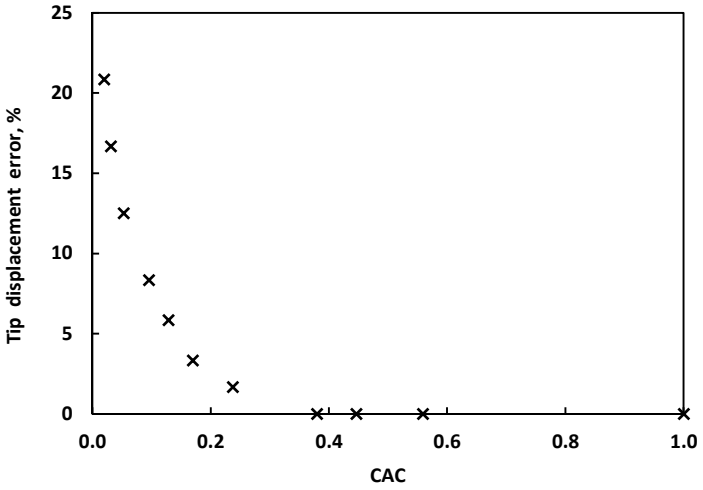

Fig. 6.11 Variation of tip displacement error with the CAC.

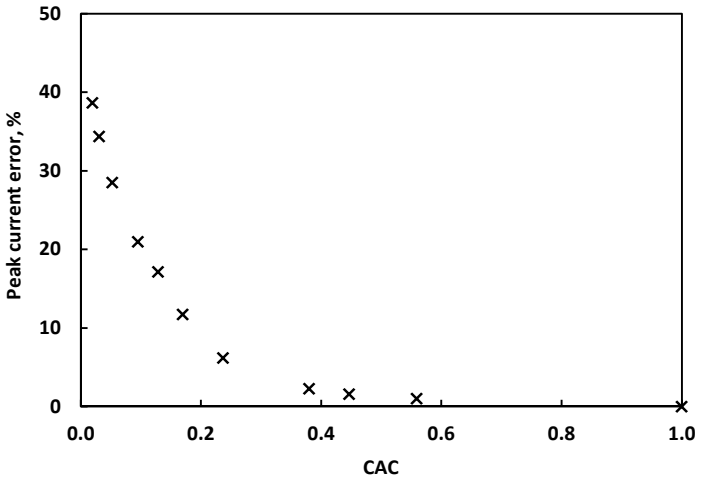

Fig. 6.12 Variation of peak current error with the CAC.

6.4 Summary

Finite element modelling of the structure with an attached electric circuit-fed piezoelectric material has been reviewed. The multi-physics system consists of a cantilever plate, a piezoelectric patch on the top of the plate and a RL circuit in series, which is modelled using ANSYS. The harmonic response analysis is conducted and it is observed that the RL series circuit can be effectively used to dampen the structural response. The FEM correlation of the coupled system is carried out using the nominal FEM model and the intentionally erroneous

models generated from the nominal FEM. It is observed that standard structural modal validation method, MAC does not give any useful correlation of the dynamic characteristics of the multi-physics system. This is because even if there is no observable change in the mode shapes as in this cantilever structure, the response of the structure still varies. However, in this case MAC will indicate a high value. A new correlation tool termed as CAC is introduced by comparing the electric current in the circuit during the harmonic excitation obtained from the nominal model, and that noted from the erroneous FEM model. A good correlation has been obtained between CAC and the structural dynamic characteristics error and it is able to predict the error in the peak current in the electrical circuit. For the typical problem considered in this study, a CAC value of 0.2 always assures that the error in the response is within 2%, hence CAC can be used for the assessment of FEMs of these types of multi-physics systems.

Chapter 7.
Conclusions and Suggestions for Further Work

This chapter presents the conclusions of the work reported in this thesis, main contributions to the state of the art and some guidelines for the further work.

7.1 Enhancements on Structural and Multi-Physics FEM Correlation Methods

7.1.1 Correlation of Spacecraft FEM

Although many correlation methods are available for the validation of FEMs, the MAC and NCO check are the accepted criteria in the space industry. To tackle the generally incomplete measured data and the full set of analytical data in the NCO correlation, which requires a compatibility of the two data sets, many reduction or expansion techniques are available. Reduction in the DOFs is preferred due to its greater accuracy than the expansion since the expansion process required the FEM prior to its validation and this introduces additional errors in the process. It has been observed that, SEREP together with the NCO check is suitable for the validation of spacecraft structures. For a successful correlation using the NCO check, it is better to include only the required target modes in the SEREP reduction. Although, SEREPa is computationally efficient, it leads to an unreasonably low chance of correlation even for very low percentages (0.1 % or less) of inaccuracy present in the modes. In addition, highly uncorrelated target modes generated using random numbers give a better NCO correlation than the correlated target modes.

It has also been observed that although a spacecraft FEM may fail the NCO check, it could still predict the receptance FRF with higher accuracy than another FEM, which passes the NCO check. This indicates the inability of NCO to predict the capability of FEM to represent the receptance. Hence, the accuracy in the prediction of the dynamic stress or strain in the structural components cannot be guaranteed, even if the FEM passes the NCO criterion. In addition, a SEREP based method is introduced to optimally select the sensor locations from the available set. The results show that, the proposed SEREP based sensor location optimisation yields better probability of passing the NCO check than the EFI based optimisation and can avoid the nodal points of the target modes.

Base excitation tests are usually conducted for the qualification of spacecraft structures. It has been shown that the MAC and NCO check do not always ensure the capability of the FEM to represent the forced response characteristics under the base excitation. This was demonstrated using three spacecraft structures FEMs and a number of erroneous finite element models generated from the corresponding nominal models. It is also observed that, sometimes models with very low values (less than 0.4) of the MAC or NCO are able to represent the transmitted force to the base, peak acceleration and the dynamic displacement within an error of 5%. Generally, such a low value of the correlation is considered to be unsuccessful and the models are rejected. In addition, two different FEMs with equal value of the MAC or NCO indicated different levels of transmitted force to the base. It was also observed that sometimes models with a lower MAC or NCO value perform in a better way than the models with a higher MAC or NCO value in predicting the forced response characteristics under base excitation.

The proposed base force assurance criterion has better correlation characteristics than either the MAC or NCO check in the prediction of error in peak acceleration or displacement (and hence stress in the structural elements) under base excitation. With the help of three spacecraft models considered in this study, it is shown that a BFAC average value of 0.8 always assures that the error in the displacement or the peak acceleration responses are less than 5% of the nominal value.

Comparison between the nominal modes, synthetic modes derived from the nominal modes and modes obtained from the erroneous FEMs have been performed. It is observed that synthetic and physically altered modes can give identical mode shapes and hence, irrespective of the method used to generate the mode shapes, the correlation study performed here gives similar results.

7.1.2 Correlation of Multi-Physics Systems

Multi-physics systems are progressively being used in spacecraft design to meet the specific mission requirements. FEMs with or without coupled DOFs are used to predict the behaviour of such systems. It is observed that viscoelastic materials are used for the vibration attenuation in light weight aerospace structures and the modal loss factor is the important design parameter for such systems. To assess the usefulness of accepted correlation methods in the space industry –MAC and NCO - to correlate the viscoelastic damped systems, analyses were performed using the nominal FEM and 12 intentionally erroneous FEMs of two simple configurations. The MAC values were also computed using the complex modes of the viscoelastic systems and did not observe any significant change from the MAC values computed using real modes. Hence, only the real modes were used for the further analysis. It has been shown that the FEM, which pass the MAC or NCO criterion, sometimes gives a modal loss factor error as high 50%. Also, the model that has a lower MAC or NCO value is sometimes better in the prediction of the modal loss factor error than the FEM with a higher MAC or NCO value. Hence, it can be concluded that, as in the case of conventional spacecraft structures, the MAC and NCO check do not give any useful indication of the capability of FEM in predicting the loss factor.

It has been observed that BFAC can correlate the loss factor error more successfully than the MAC or NCO check in the systems analysed; a particular value of BFAC always indicated a specific level of error in the loss factor. The variation in the MAC and NCO values with the temperature were also analysed using two viscoelastic systems and the corresponding erroneous FEMs and it was noticed that there is a maximum change of 36% in the MAC values and a negligible change in the NCO over the temperature band of 10 to 70 °C.

For the second type of multi-physics system considered, the harmonic response analysis was performed using ANSYS multi-physics software. This FEM of a shunted piezoelectric circuit system consisted of structural and electrical DOFs and the required damping was achieved by tuning the resistance and inductance. The validations of this coupled system has been performed using this nominal model and erroneous FEMs created by considering the uncertainty in the piezoelectric material properties. The usefulness of the widely used 'structural' FEM correlation method(MAC) for the correlation of an electro-mechanical system was assessed and it was found that the usefulness is limited. A new correlation tool is introduced for the system by comparing the frequency dependant electric current produced in the circuit during the harmonic excitation obtained from the nominal model and those obtained from the erroneous coupled FEM. This correlation index termed the current assurance criterion is defined in a similar way as the MAC between the mode shapes. A CAC value of 1.0 indicates an identical electric current in the frequency range and 0.0 indicates completely differing current values. It has been observed that the CAC can indicate the possible error in the structural response such as the dynamic displacement and acceleration as well as the peak current in the circuit.

7.2 Main Contributions

The main contributions of this thesis with respect to the current state of the art are summarised as follows.

- The robustness of a SEREP based TAM with respect to inaccuracies in the experimental and analytical modes has been analysed with the help of three different sizes of spacecraft structure FEMs. It has been shown that for practical purposes the modes used in the SEREP should be only the target modes and the computational efficiency of SEREPa deteriorates the test analysis correlation.
- A novel SEREP based sensor location optimisation has been introduced to identify the optimal sensor locations.

- It has been shown that although a spacecraft FEM may fail the NCO check, it could still predict the displacement based FRF with a higher accuracy than the FEM that passes the NCO check.
- It has been shown that the standard correlation tools – the MAC and NCO check- used in the space industry to qualify the FEMs fail to predict the FEM capability of simulating the forced response characteristics under base excitation.
- A new correlation method, termed the base force assurance criterion, is introduced to qualify a FEM under base excitation. Unlike the MAC or NCO check, BFAC can predict the capability of FEM in representing the acceleration response and the stress in the structure under base excitation.
- The correlations of two types of multi-physics systems have been performed using standard correlation tools and the BFAC is found to be a useful tool for the correlation of viscoelastic damped system models. The effect of temperature on MAC and NCO were analysed using viscoelastic properties. In addition, the effect of damping on the MAC was analysed using complex modes.
- An electric current based correlation method was introduced to validate the coupled model of a shunted piezoelectric system under harmonic excitation.

7.3 Further Work

The synthetic modes in this study have been generated from the results of the frequency domain analysis. The primary data from the experiments are in time domain and one could perturb time domain data directly to generate synthetic parameters and then extract the modal parameters for the correlation study. In addition, a stochastic coupled load analysis of spacecraft and launch vehicle can be performed by considering the probability of variation in the design parameters such as the structural dimensions, material properties, and the environmental loads. This uncertainty based load analysis helps to determine the robustness of the design to the most likely variables.

The proposed base force assurance criterion can be verified using the experimentally determined dynamic force at the base of a spacecraft and with

the FEM counterpart. The acceleration response at important locations are routinely monitored in all qualification tests of the spacecraft and with the additional force measurements at the base, the new criterion can be verified. The experimental investigation of the current assurance criterion can also form the basis of further work in multi-physics systems. In addition, depending on the type of physical systems integrated in the multi-physics systems, separate correlation tools can be defined using the appropriate physical quantities.

Appendices

Appendix 1

The sub matrices in the Craig-Bampton equation of motion given in Eq. (4.4) are defined as follows.

$$\boldsymbol{M}_{BB} = \boldsymbol{M}_{RR} + \boldsymbol{M}_{RL}\boldsymbol{\phi}_R + \boldsymbol{\Phi}_R{}^T \boldsymbol{M}_{LR} + \boldsymbol{\phi}_R{}^T \boldsymbol{M}_{LL}\boldsymbol{\phi}_R \,. \tag{A1.1}$$

This is the structural mass matrix reduced at the boundary in the same way as the Guyan reduction [16]. If the boundary set, *R* contains only one DOF for each translation and rotation as in the case of typical base shake analysis of a spacecraft, then $\boldsymbol{M}_{BB}$ is approximately equal to the rigid body mass matrix of the structure. Other reduced sub-mass matrices are defined as:

$$\boldsymbol{M}_{mB} = \boldsymbol{\phi}_L{}^T \left[\boldsymbol{M}_{LR} + \boldsymbol{M}_{LL}\boldsymbol{\phi}_R\right] \tag{A1.2}$$

$$\boldsymbol{M}_{Bm} = \left[\boldsymbol{M}_{RL} + \boldsymbol{\phi}_R{}^T \boldsymbol{M}_{LL}\right]\boldsymbol{\phi}_L = \boldsymbol{M}_{mB}^T \tag{A1.3}$$

$$\boldsymbol{M}_{mm} = \boldsymbol{\phi}_L{}^T \boldsymbol{M}_{LL}\boldsymbol{\phi}_L \tag{A1.4}$$

where, $\boldsymbol{M}_{mm}$ is the generalised mass matrix.

$$\boldsymbol{K}_{BB} = \boldsymbol{K}_{RR} + \boldsymbol{K}_{RL}\boldsymbol{\phi}_R \,. \tag{A1.5}$$

This is the Guyan reduced stiffness matrix at the boundary. The matrix, $\boldsymbol{K}_{BB}$ is zero if the boundary is statically determinate. The generalised stiffness matrix, $\boldsymbol{K}_{mm}$ is given by:

$$\boldsymbol{K}_{mm} = \boldsymbol{\phi}_L{}^T \boldsymbol{K}_{LL}\boldsymbol{\phi}_L \,. \tag{A1.6}$$

Appendix 2

An Approximate Expression for the Modal Loss Factor

The modal loss factor of the complex structure with viscoelastic damping was calculated using the approximate method proposed by Johnson and Kienholz [83]. This approach is based on the modal strain energy method introduced by Ungar [85] and the derivation for the modal loss factor using this method is given below [83].

The equation for the free vibration of viscoelastic system can be written as:

$$\boldsymbol{M}\ddot{\boldsymbol{x}} + (\boldsymbol{K}_{Re} + i\boldsymbol{K}_{Im})\boldsymbol{x} = \boldsymbol{0} \tag{A2.1}$$

where $\boldsymbol{K}_{Re}$ and $\boldsymbol{K}_{Im}$ are the real and the imaginary part of the stiffness matrix. The equation can be converted to an eigenvalue problem by considering a solution,

$$\boldsymbol{x} = \bar{\boldsymbol{\phi}}^{r} e^{i\bar{\lambda}_r t} \tag{A2.2}$$

where $\bar{\lambda}_r$ and $\bar{\boldsymbol{\phi}}^{r}$ are the rth complex eigenvalue and eigenvector. The complex eigenvalue can also be written as:

$$\bar{\boldsymbol{\lambda}}_r = \boldsymbol{\lambda}_r \sqrt{1 + i\eta^{r}} \tag{A2.3}$$

where η^{r} represents the loss factor of the rth mode. For the complex stiffness matrix considered in Eq. (A2.1), the Raleigh's quotient formula can be written as:

$$\bar{\boldsymbol{\lambda}}^2 = \boldsymbol{\lambda}^2 + i\eta\boldsymbol{\lambda}^2 = \frac{\bar{\boldsymbol{\phi}}^T \boldsymbol{K}_{Re} \bar{\boldsymbol{\phi}}}{\bar{\boldsymbol{\phi}}^T \boldsymbol{M} \bar{\boldsymbol{\phi}}} + i\frac{\bar{\boldsymbol{\phi}}^T \boldsymbol{K}_{Im} \bar{\boldsymbol{\phi}}}{\bar{\boldsymbol{\phi}}^T \boldsymbol{M} \bar{\boldsymbol{\phi}}}. \tag{A2.4}$$

The loss factor can be approximated by replacing the complex eigenvector, $\bar{\boldsymbol{\phi}}$ with the real eigenvector, $\boldsymbol{\phi}$ in Eq. (A2.4). In this case, the real eigenvector can be obtained by neglecting the imaginary part of the stiffness matrix and solving the pure elastic eigenvalue problem. Then, equating the real and imaginary part give:

$$\lambda^2 = \frac{\boldsymbol{\phi}^T \mathbf{K}_{Re} \boldsymbol{\phi}}{\boldsymbol{\phi}^T \mathbf{M} \boldsymbol{\phi}} \tag{A2.5}$$

$$\eta\lambda^2 = \frac{\boldsymbol{\phi}^T \mathbf{K}_{Im} \boldsymbol{\phi}}{\boldsymbol{\phi}^T \mathbf{M} \boldsymbol{\phi}} \ . \tag{A2.6}$$

The stiffness matrix obtained using the finite element analysis can be segregated to the terms corresponding to the elastic elements, $\mathbf{K}_e$ and the viscoelastic elements, $\mathbf{K}_v$. The second matrix will be a complex matrix, but for a single viscoelastic material, its imaginary part ($\mathbf{K}_{vI}$), and real part ($\mathbf{K}_{vR}$) follows the relation:

$$\mathbf{K}_{vI} = \eta_v \mathbf{K}_{vR} \tag{A2.7}$$

where η_v is the loss factor of the viscoelastic material at the *r*th resonant frequency. Hence,

$$\mathbf{K}_v = \mathbf{K}_{vR} + i\mathbf{K}_{vI} = \mathbf{K}_{vR}(1 + i\eta_V) . \tag{A2.8}$$

Assuming that only the complex part of $\mathbf{K}_v$ contributes to the imaginary part of the system stiffness matrix, then:

$$\mathbf{K}_{Im} = \mathbf{K}_{vI} . \tag{A2.9}$$

Let V_T be the total strain energy obtained when a purely elastic normal mode analysis is performed. This can be calculated using the normal modes as:

$$V_T = \boldsymbol{\phi}^T \mathbf{K}_{Re} \boldsymbol{\phi} . \tag{A2.10}$$

A portion of the total strain energy will be contributed by the viscoelastic elements and it is given by:

$$V_v = \boldsymbol{\phi}^T \mathbf{K}_{vR} \boldsymbol{\phi} . \tag{A2.11}$$

Using the Eqs. (A2.5)–(A2.6), the modal loss factor can be obtained as:

$$\eta = \frac{\boldsymbol{\phi}^T \mathbf{K}_{Im} \boldsymbol{\phi}}{\boldsymbol{\phi}^T \mathbf{K}_{Re} \boldsymbol{\phi}} \ . \tag{A2.12}$$

Using the relationship shown in Eq. (A2.9) and Eq. (A2.7), the above equation can be re-written as:

$$\eta = \frac{\eta_v \boldsymbol{\phi}^T \boldsymbol{K}_{vR} \boldsymbol{\phi}}{\boldsymbol{\phi}^T \boldsymbol{K}_{Re} \boldsymbol{\phi}}. \tag{A2.13}$$

Substituting Eqs. (A2.10)–(A2.11) in Eq. (A2.13) gives the loss factor for each mode r as:

$$\eta^r = \eta_v \left(\frac{V_v^r}{V_T^r} \right). \tag{A2.14}$$

Appendix 3

Table A3.1 shows the analogy between mechanical and electrical quantities.

Table A3.1 Mechanical and electrical quantities

Mechanical	Electrical
Force density, $\boldsymbol{f}$	Electric charge, $\boldsymbol{q}$
Displacement, $\boldsymbol{x}$	Electric potential, $\boldsymbol{v}$
Stress, $\boldsymbol{\sigma}$	Flux density, $\boldsymbol{d}$
Strain, $\boldsymbol{\varepsilon}$	Electric field, $\boldsymbol{e}$

Individual terms in the equilibrium equations of the electro-mechanical system (given in Eqs. (6.18)-(6.19)) are shown in Table A3.2 [47].

Table A3.2 Electro-elastic parameters

Parameter	Description
$\boldsymbol{M}_{xx} = \rho \iiint_V \boldsymbol{N}_x^T \boldsymbol{N}_x dV$	Mass matrix
$\boldsymbol{K}_{xx} = \iiint_V \boldsymbol{B}_x^T \boldsymbol{C} \boldsymbol{B}_x dV$	Stiffness matrix
$\boldsymbol{K}_{xv} = \iiint_V \boldsymbol{B}_x^T \boldsymbol{P} \boldsymbol{B}_v dV$	Piezoelectric stiffness matrix
$\boldsymbol{f}_B = \iiint_V \boldsymbol{N}_x^T \boldsymbol{N}_{\bar{f}} dV \overline{\boldsymbol{f}}_i$	Body force
$\boldsymbol{f}_S = \iint_{S_1} \boldsymbol{N}_x^T \boldsymbol{N}_{\bar{\sigma}} dS \overline{\boldsymbol{\sigma}}_i$	Surface force
$\boldsymbol{f}_p = \boldsymbol{N}_x^T \boldsymbol{p}$	Concentrated force
$\boldsymbol{K}_{vx} = \iiint_V \boldsymbol{B}_v^T \boldsymbol{P}^T \boldsymbol{B}_x dV$	Piezoelectric stiffness matrix
$\boldsymbol{K}_{vv} = -\iiint_V \boldsymbol{B}_v^T \boldsymbol{D} \boldsymbol{B}_v dV$	Dielectric stiffness matrix
$\boldsymbol{q}_B = -\iiint_V \boldsymbol{n}_v N_{\bar{q}} dV \overline{\boldsymbol{q}}_i$	Body charge
$\boldsymbol{q}_s = -\iint_{S_2} \boldsymbol{n}_v N_{\bar{q}} dS \overline{\boldsymbol{q}}_i^{'}$	Surface charge
$\boldsymbol{q}_p = -\boldsymbol{n}_v Q$	Point charge

Bibliography

[1] Aglietti, G. S., Walker, S. J. I., and Kiley, A., "On the Use of SEREP for Satellite Fem Validation", *Engineering Computations,* Vol. 29, No. 6, 2012, pp. 580-595.

doi: 10.1108/02644401211246292

[2] Aglietti, G. S., Richardson, G., and Quill, P., "Launch Environment", *Encyclopedia of Aerospace Engineering*, John Wiley and Sons, Inc., 2010.

[3] Calvi, A., "Uncertainty-Based Loads Analysis for Spacecraft: Finite Element Model Validation and Dynamic Responses", *Computers and Structures,* Vol. 83, No. 14, 2005, pp. 1103-1112.

doi: 10.1016/j.compstruc.2004.11.019

[4] Hasselman, T. K., Coppolino, R. N., and Zimmerman, D. C., "Criteria for Modeling Accuracy: A State-of-the-Practice Survey", Proceedings of *18th International Modal Analysis Conference,* Vol. 1-2, Society for Experimental Mechanics, Connecticut, USA, Feb. 2000, pp. 335-341.

[5] Ewins, D. J., "Modal Testing Theory, Practice and Application", *Engineering Dynamics Series*, *2* ed., Research Studies Press Ltd, Baldock, England, 2000.

[6] Allemang, R. J., and Brown, D. L., "A Correlation Coefficient for Modal Vector Analysis", Proceedings of *1st International Modal Analysis Conference*, Society for Experimental Mechanics, Connecticut, USA, Nov. 1982, pp. 110-116.

[7] Kammer, D. C., "Test Analysis Model Development Using an Exact Modal Reduction", *International Journal of Analytical and Experimental Modal Analysis,* Vol. 2, No. 4, 1987, pp. 174-179.

[8] O'callahan, J., Avitabile, P., and Riemer, R., "System Equivalent Reduction Expansion Process (SEREP)", Proceedings of *7th International Modal Analysis Conference*, Society for Experimental Mechanics, Connecticut, USA, Jan. 1989, pp. 29-37.

[9] "Loads Analysis of Spacecraft and Payloads", NASA-STD-5002, URL: https://standards.nasa.gov/training/nasa-std-5002/index.html [cited 23/03/2011].

[10] "Modal Survey Assessment", ECSS-E-ST-32-11C, European Space Agency, July 2008, p. 49.

[11] O'callahan, J., "In Search of the IRS", Proceedings of *23rd International Modal Analysis Conference*, Society for Experimental Mechanics, Connecticut, USA, 2005, pp. 1-7.

[12] Avitabile, P., "Model Reduction and Model Expansion and Their Applications: Part 2 - Applications", Proceedings of *23rd International Modal Analysis Conference*, Society for Experimental Mechanics, Connecticut, USA, 2005, pp. 1-8.

[13] Lin, R. M., Lim, M. K., and Du, H., "Improved Inverse Eigensensitivity Method for Structural Analytical Model Updating", *Journal of Vibration and Acoustics-Transactions of the ASME,* Vol. 117, No. 2, 1995, pp. 192-198.

doi: 10.1115/1.2873889

[14] Kammer, D. C., and Tinker, M. L., "Optimal Placement of Triaxial Accelerometers for Modal Vibration Tests", *Mechanical Systems and Signal Processing,* Vol. 18, No. 1, 2004, pp. 29-41.

doi: 10.1016/s0888-3270(03)00017-7

[15] Papadimitriou, C., "Optimal Sensor Placement Methodology for Parametric Identification of Structural Systems", *Journal of Sound and Vibration,* Vol. 278, No. 4-5, 2004, pp. 923-947.

doi: 10.1016/j.jsv.2003.10.063

[16] Guyan, R. J., "Reduction of Mass and Stiffness Matrices", *AIAA Journal,* Vol. 3, 1965, p. 380.

doi: 10.2514/3.2874

[17] Irons, B., "Structural Eigenvalue Problems: Elimination of Unwanted Variables ", *AIAA Journal,* Vol. 3, No. 5, 1964, pp. 961-962.

doi: 10.2514/3.3027

[18] Shah, V. N., and Raymund, M., "Analytical Selection of Masters for the Reduced Eigenvalue Problem", *International Journal for Numerical Methods in Engineering,* Vol. 18, No. 1, 1982, pp. 89-98.

doi: 10.1002/nme.1620180108

[19] Kidder, R. L., "Reduction of Structural Frequency Equations", *AIAA Journal,* Vol. 11, No. 6, 1973, pp. 892-892.

doi: 10.2514/3.6852

[20] Miller, C. A., "Dynamic Reduction of Structural Models", *Journal of the Structural Division-ASCE,* Vol. 106, No. 10, 1980, pp. 2097-2108.

[21] Paz, M., "Dynamic Condensation", *AIAA Journal,* Vol. 22, No. 5, 1984, pp. 724-726.

doi: 10.2514/3.48498

[22] O'callahan, J., "A Procedure for an Improved Reduced System (IRS) Model", Proceedings of *7th International Modal Analysis Conference*, Society for Experimental Mechanics, Connecticut, USA,, Jan. 1989, pp. 17-21.

[23] Friswell, M. I., Garvey, S. D., and Penny, J. E. T., "Model Reduction Using Dynamic and Iterated Irs Techniques", *Journal of Sound and Vibration,* Vol. 186, No. 2, 1995, pp. 311-323.

doi: 10.1006/jsvi.1995.0451

[24] Kammer, D. C., "A Hybrid Approach to Test Analysis Model Development for Large Space Structures", *Journal of Vibration and Acoustics-Transactions of the ASME,* Vol. 113, No. 3, 1991, pp. 325-332.

doi: 10.1115/1.2930188

[25] Sastry, C. V. S., Mahapatra, D. R., Gopalakrishnan, S., and Ramamurthy, T. S., "An Iterative System Equivalent Reduction Expansion Process for Extraction of High Frequency Response from Reduced Order Finite Element Model", *Computer Methods in Applied Mechanics and Engineering,* Vol. 192, No. 15, 2003, pp. 1821-1840.

doi: 10.1016/s0045-7825(03)00204-4

[26] Nimityongskul, S., and Kammer, D. C., "Frequency Domain Model Reduction Based on Principal Component Analysis", *Mechanical Systems and Signal Processing,* Vol. 24, No. 1, 2010, pp. 41-51.

doi: 10.1016/j.ymssp.2009.05.005

[27] O'hara, G. J., "Mechanical Impedance and Mobility Concepts", *Journal of Acoustical Society of America,* Vol. 41, No. 5, 1967, pp. 1180-1184.

[28] Lieven, N. A. J., and Ewins, D. J., "Spatial Correlation of Mode Shapes: The Coordinate Modal Assurance Criterion (COMAC)", Proceedings of *6th International Modal Analysis Conference*, Society for Experimental Mechanics, Connecticut, USA, Feb. 1988, pp. 690-695.

[29] Pascual, R., Golinval, J. C., and Razeto, M., "A Frequency Domain Correlation Technique for Model Correlation and Updating", Proceedings of *15th International Modal Analysis Conference,* Society for Experimental Mechanics, Connecticut, USA, Feb. 1997, pp. 587-592.

[30] Nefske, D., Sung, S.,. "Correlation of a Coarse Mesh Finite Element Model Using Structural System Identification and a Frequency Response Criterion", Proceedings of *14th International Model Analysis Conference*, Society for Experimental Mechanics, Connecticut, USA, Feb. 1996, pp. 597-602.

[31] Collins, J. D., Hart, G. C., Hasselma.Tk, and Kennedy, B., "Statistical Identification of Structures", *AIAA Journal,* Vol. 12, No. 2, 1974, pp. 185-190.

doi: 10.2514/3.49190

[32] Berman, A., and Nagy, E. J., "Improvement of a Large Analytical Model Using Test Data", *AIAA Journal,* Vol. 21, No. 8, 1983, pp. 1168-1173.

doi: 10.2514/3.60140

[33] Kabe, A. M., "Stiffness Matrix Adjustment Using Mode Data", *AIAA Journal,* Vol. 23, No. 9, 1985, pp. 1431-1436.

doi: 10.2514/3.9103

[34] Butland, A., and Avitabile, P., "A Reduced Order, Test Verified Component Mode Synthesis Approach for System Modeling Applications", *Mechanical Systems and Signal Processing,* Vol. 24, No. 4, 2010, pp. 904-921.

doi: 10.1016/j.ymssp.2009.08.008

[35] Starek, L., and Inman, D. J., "Solution of the Model Correlation Problem Via Inverse Methods", Proceedings of *9th International Modal Analysis Conference*, Society for Experimental Mechanics, Connecticut, USA, Apr. 1991, pp. 352-355.

[36] Mottershead, J. E., and Friswell, M. I., "Model Updating in Structural Dynamics - a Survey", *Journal of Sound and Vibration,* Vol. 167, No. 2, 1993, pp. 347-375.

doi: 10.1006/jsvi.1993.1340

[37] Lin, R. M., and Zhu, J., "Finite Element Model Updating Using Vibration Test Data under Base Excitation", *Journal of Sound and Vibration,* Vol. 303, No. 3-5, 2007, pp. 596-613.

doi: 10.1016/j.jsv.2007.01.029

[38] Bergman, E. J., Allen, M. S., Kammer, D. C., and Mayes, R. L., "Probabilistic Investigation of Sensitivities of Advanced Test-Analysis Model Correlation Methods", *Journal of Sound and Vibration,* Vol. 329, No. 13, 2010, pp. 2516-2531.

doi: 10.1016/j.jsv.2010.01.009

[39] Aglietti, G. S., Redi, S., Walker, S. J. I., and Kiley, A., "Robustness of the Orthogonality Checks on a Satellite Fem Using a Serep Test Analysis Model", Proceedings of *24th International Conference on Noise and Vibration Engineering and 3rd International Conference on Uncertainty in Structural Dynamics*, Katholieke Universiteit Leuven, Belgium, Sep 2010, pp. 5079-5092.

[40] Aglietti, G. S., Walker, S. J. I., and Kiley, A., "On the Use of 'SEREP' for Satellite FEM Validation", *4th International Conference on Advanced Computational Engineering and Experimenting*, Paris, Jul. 2010.

[41] Avitabile, P., "Some Common Issues in Modal Correlation/Validation", Proceedings of *24th International Modal Analysis Conference*, Society for Experimental Mechanics, Connecticut, USA, Jan. 2006, pp. 1-5.

[42] Aglietti, G. S., Schwingshackl, C. W., and Roberts, S. C., "Multifunctional Structure Technologies for Satellite Applications", *Shock and Vibration Digest,* Vol. 39, No. 5, 2007, pp. 381-391.

[43] Gibson, R. F., "A Review of Recent Research on Mechanics of Multifunctional Composite Materials and Structures", *Composite Structures,* Vol. 92, No. 12, 2010, pp. 2793-2810.

doi: 10.1016/j.compstruct.2010.05.003

[44] Noor, A. K., Venneri, S. L., Paul, D. B., and Hopkins, M. A., "Structures Technology for Future Aerospace Systems", *Computers and Structures,* Vol. 74, No. 5, 2000, pp. 507-519.

[45] Chopra, I., "Review of State of Art of Smart Structures and Integrated Systems", *AIAA Journal,* Vol. 40, No. 11, 2002, pp. 2145-2187.

doi: doi: 10.2514/2.1561

[46] Eernisse, E. P., "Variational Method for Electroelastic Vibration Analysis", *IEEE Transactions on Sonics and Ultrasonics,* Vol. 14, No. 4, 1967, pp. 153-160.

[47] Allik, H., and Hughes, T. J. R., "Finite Element Method for Piezoelectric Vibration", *International Journal for Numerical Methods in Engineering,* Vol. 2, No. 2, 1970.

doi: 10.1002/nme.1620020202

[48] Aglietti, G. S., Cunningham, P. R., and Langley, R. S., "Verification of Various Modelling Techniques for Simply-Supported Piezoelectric Actuated Thin Panels", *Proceedings of the Institution of Mechanical Engineers Part G-Journal of Aerospace Engineering,* Vol. 216, No. G3, 2002, pp. 155-164.

doi: 10.1243/095441002760553694

[49] Wang, X., Liu, Y., Gao, W., and Chen, J., "Mixed Piezothermoelastic Finite Element Model for Thunder Actuators", *AIAA Journal,* Vol. 49, No. 10, 2011, pp. 2100-2108.

doi: 10.2514/1.j050284

[50] Becker, J., Fein, O., Maess, M., and Gaul, L., "Finite Element-Based Analysis of Shunted Piezoelectric Structures for Vibration Damping", *Computers and Structures,* Vol. 84, No. 31-32, 2006, pp. 2340-2350.

doi: 10.1016/j.compstruc.2006.08.067

[51] Gang, W., Jianwei, W., Shengbing, C., and Jihong, W., "Vibration Attenuations Induced by Periodic Arrays of Piezoelectric Patches Connected by Enhanced Resonant Shunting Circuits", *Smart Materials and Structures,* Vol. 20, No. 12, 2011, pp. 1-9.

doi: 10.1088/0964-1726/20/12/125019

[52] Gao, J. X., and Cheng, L., "Modelling of a High Performance Piezoelectric Actuator Assembly for Active and Passive Vibration Control", *Smart Materials and Structures,* Vol. 13, No. 2, 2004, pp. 384-392.

doi: 10.1088/0964-1726/13/2/017

[53] Gao, J. X., Shen, Y. P., and Wang, J., "Three Dimensional Analysis for Free Vibration of Rectangular Composite Laminates with Piezoelectric Layers", *Journal of Sound and Vibration,* Vol. 213, No. 2, 1998, pp. 383-390.

doi: 10.1006/jsvi.1997.1476

[54] Min, J. B., Duffy, K. P., and Provenza, A. J., "Shunted Piezoelectric Vibration Damping Analysis Including Centrifugal Loading Effects", *51st AIAA/ASME/ASCE/AHS/ASC Structures, Structural Dynamics, and Materials Conference*, Orlando, Florida, AIAA 2010-2716, Apr. 2010.

[55] Stephen, N. G., "On Energy Harvesting from Ambient Vibration", *Journal of Sound and Vibration,* Vol. 293, No. 1-2, 2006, pp. 409-425.

doi: 10.1016/j.jsv.2005.10.003

[56] Christodoulou, L., and Venables, J. D., "Multifunctional Material Systems: The First Generation", *Journal of the Minerals Metals and Materials Society,* Vol. 55, No. 12, 2003, pp. 39-45.

[57] Torquato, S., Hyun, S., and Donev, A., "Multifunctional Composites: Optimizing Microstructures for Simultaneous Transport of Heat and Electricity", *Physical Review Letters,* Vol. 89, No. 26, 2002.

doi: 10.1103/PhysRevLett.89.266601

[58] Torquato, S., Hyun, S., and Donev, A., "Optimal Design of Manufacturable Three-Dimensional Composites with Multifunctional Characteristics", *Journal of Applied Physics,* Vol. 94, No. 9, 2003, pp. 5748-5755.

doi: 10.1063/1.1611631

[59] Elzey, D. M., Sofla, A. Y. N., and Wadley, H. N. G., "A Shape Memory-Based Multifunctional Structural Actuator Panel", *International Journal of Solids and Structures,* Vol. 42, No. 7, 2005, pp. 1943-1955.

doi: 10.1016/j.ijsolstr.2004.05.034

[60] Lin, J. K. H., Knoll, C. F., and Willey, C. E., "Shape Memory Rigidizable Inflatable Structures for Large Space Systems Applications", *47th AIAA/ASME/ASCE/AHS/ASC Structures, Structural Dynamics, and*

Materials Conference, Newport, Rhode Island, AIAA 2006-1896, May 2006.

[61] John, R., Atxaga, G., Frerker, H. J., Newerla, A., and Eda. "Advancement of Multifunctional Support Structure Technologies", Proceedings of *13th International Workshop on Thermal Investigation of Ics and Systems*, EDA Publishing, Grenoble, France, Sep. 2007*,* pp. 98-103.

[62] Jang, T. S., Oh, D. S., Kim, J. K., Kang, K. I., Cha, W. H., and Rhee, S. W., "Development of Multi-Functional Composite Structures with Embedded Electronics for Space Application", *Acta Astronautica,* Vol. 68, No. 1-2, 2011, pp. 240-252.

doi: 10.1016/j.actaastro.2010.08.009

[63] Baturkin, V., "Micro-Satellites Thermal Control - Concepts and Components", *Acta Astronautica,* Vol. 56, No. 1-2, 2005, pp. 161-170.

doi: 10.1016/j.actaastro.2004.09.003

[64] Gottero, M., Zeminiani, E., Poidomani, G., and Sacchi, E., "Development of Multifunctional Structures at Thales Alenia Space Italia", *37th International Conference on Environmental System*, SAE International,Chicago, Jul. 2007.

[65] Sairajan, K. K., and Nair, P. S., "Design of Low Mass Dimensionally Stable Composite Base Structure for a Spacecraft", *Composites Part B-Engineering,* Vol. 42, No. 2, 2011, pp. 280-288.

doi: 10.1016/j.compositesb.2010.11.003

[66] Clark, C., Summers, J., and Armstrong, J., "Innovative Flexible Lightweight Thin-Film Power Generation and Storage for Space Applications", Proceedings of *35th Intersociety Energy Conversion Engineering Conference and Exhibit,* Vol. 1-2, AIAA, Reston, Virginia, July 2000*,* pp. 692-698.

[67] Pereira, T., Guo, Z. H., Nieh, S., Arias, J., and Hahn, H. T., "Embedding Thin-Film Lithium Energy Cells in Structural Composites", *Composites Science and Technology,* Vol. 68, No. 7-8, 2008, pp. 1935-1941.

doi: 10.1016/j.compscitech.2008.02.019

[68] Pereira, T., Guo, Z. H., Nieh, S., Arias, J., and Hahn, H. T., "Energy Storage Structural Composites: A Review", *Journal of Composite Materials,* Vol. 43, No. 5, 2009, pp. 549-560.

doi: 10.1177/0021998308097682

[69] Neudecker, B. J., Benson, M. H., and Emerson, B. K., "Power Fibres: Thin-Film Batteries on Fibre Substrates", *14th International Conference on Composite Materials*, San Diego, July 2003.

[70] Metzger, W., Westfall, R., Hermann, A., and Lyman, P., "Nickel Foam Substrate for Nickel Metal Hydride Electrodes and Lightweight Honeycomb Structures", *International Journal of Hydrogen Energy,* Vol. 23, No. 11, 1998, pp. 1025-1029.

[71] Lyman, P. C., and Feaver, T. L., "Powercore: Combining Structure and Batteries for Increased Energy to Weight Ratio", *IEEE Aerospace and Electronic Systems Magazine,* Vol. 13, No. 9, 1998, pp. 39-42.

[72] Schwingshackl, C. W., Aglietti, G. S., and Cunningham, P. R., "Parameter Optimization of the Dynamic Behavior of Inhomogeneous Multifunctional Power Structures", *AIAA Journal,* Vol. 44, No. 10, 2006, pp. 2286-2294.

doi: 10.2514/1.18599

[73] Schwingshackl, C. W., Aglietti, G. S., and Cunningham, P. R., "Experimental Determination of the Dynamic Behavior of a Multifunctional Power Structure", *AIAA Journal,* Vol. 45, No. 2, 2007, pp. 491-496.

doi: 10.2514/1.23894

[74] Roberts, S. C., and Aglietti, G. S., "Satellite Multi-Functional Power Structure: Feasibility and Mass Savings", *Proceedings of the Institution of Mechanical Engineers Part G-Journal of Aerospace Engineering,* Vol. 222, No. G1, 2008, pp. 41-51.

doi: 10.1243/09544100jaero255

[75] Schatzel, D. V., "Flip Chip Reliability on Dynamically Loaded Multi-Functional Spacecraft Structures", Proceedings of *IEEE Aerospace Conference,* Vol. 1-9, IEEE, Washington, Mar. 2008, pp. 2395-2400.

[76] Rawal, S. P., Barnett, D. M., and Martin, D. E., "Thermal Management for Multifunctional Structures", *IEEE Transactions on Advanced Packaging,* Vol. 22, No. 3, 1999, pp. 379-383.

[77] Barnett, D. M., and Rawal, S. P., "Multifunctional Structures Technology Demonstration on New Millennium Program Deep Space 1:Technology Validation Report", Astronautics Division, Lockheed Martin, 2000.

[78] Hyonny, K., Myounggu, P., and Hsieh, K., "Fatigue Fracture of Embedded Copper Conductors in Multifunctional Composite Structures", *Composites Science and Technology,* Vol. 66, No. 7-8, 2006, pp. 1010-21.

doi: 10.1016/j.compscitech.2005.08.007

[79] Chmielewski, A. B., Das, A., Cassapakis, C., Allen, D., Schafer, W. J., Sercel, J., Deligiannis, F., Piszczor, M., Jones, P. A., Barnett, D. M., Rawal, S., and Reddy, T., "The New Millennium Program Power Technology", Proceedings of *31st Intersociety Energy Conversion Engineering Conference* , IEEE, Washington, Aug. 1996*,* pp. 2193-2198.

[80] Barnett, D. M., and Rawal, S. P., "Multifunctional Structures Technology Experiment on Deep Space 1 Mission", *IEEE Aerospace and Electronic Systems Magazine,* Vol. 14, No. 1, 1999, pp. 13-18.

[81] Fosness, E., Guerrero, J., Qassim, K., and Denoyer, S. J., "Recent Advances in Multi-Functional Structures", Proceedings of *IEEE Aerospace Conference*, IEEE, Washington, Mar. 2000*,* pp. 23-28.

[82] Kim, H. S., Kang, J. S., Park, J. S., Hahn, H. T., Jung, H. C., and Joung, J. W., "Inkjet Printed Electronics for Multifunctional Composite Structure", *Composites Science and Technology,* Vol. 69, No. 7-8, 2009, pp. 1256-1264.

doi: 10.1016/j.compscitech.2009.02.034

[83] Johnson, C. D., and Kienholz, D. A., "Finite-Element Prediction of Damping in Structures with Constrained Viscoelastic Layers", *AIAA Journal,* Vol. 20, No. 9, 1982, pp. 1284-1290.

doi: 10.2514/3.51190

[84] Rao, M. D., "Recent Applications of Viscoelastic Damping for Noise Control in Automobiles and Commercial Airplanes", *Journal of Sound and Vibration,* Vol. 262, No. 3, 2003, pp. 457-474.

doi: 10.1016/s0022-460x(03)00106-8

[85] Ungar, E. E., and Kerwin, E. M., "Loss Factors of Viscoelastic Systems in Terms of Energy Concepts", *The Journal of the Acoustical Society of America,* Vol. 34, No. 7, 1962, pp. 954-957.

[86] Marcos, J., Segura, M., Antolin, J. C., Landaberea, A., Lamela, F., and Atxaga, G., "Multifunctional Equipment Design by Using High Thermal Conductivity Fibres", Proceedings of *European Conference on Spacecraft Structures, Materials and Mechanical Testing*, ESA Communications, ESA-SP-581, Noordwijk, The Netherlands, Aug. 2005.

[87] Grasmeyer, J. M., and Keennon, M. T., "Development of the Black Widow Micro Air Vehicle", *39th Aerospace Sciences Meeting and Exhibit*, Reno, Nevada, AIAA-2001-0127, Jan. 2001, pp. 1-9.

[88] Ashby, M. F., "Multi-Objective Optimization in Material Design and Selection", *Acta Materialia,* Vol. 48, No. 1, 2000, pp. 359-369.

[89] Laborde, S., and Calvi, A., "Spacecraft Base-Sine Vibration Test Data Uncertainties Investigation Based on Stochastic Scatter Approach", *Mechanical Systems and Signal Processing,* Vol. 32, 2012, pp. 69-78.

doi: 10.1016/j.ymssp.2012.04.017

[90] Craig, R. R., and Bampton, M. C., "Coupling of Substructures for Dynamic Analyses", *AIAA Journal,* Vol. 6, No. 7, 1968, pp. 1313-1319.

doi: 10.2514/3.4741

[91] Wijker, J., "Mechanical Vibrations in Spacecraft Design"*, 1st* ed., Springer, Berlin, 2004, pp. 125-148.

[92] Avitabile, P., "Model Reduction and Model Expansion and Their Applications: Part 1 - Theory", Proceedings of *23rd International Modal Analysis Conference*, Society for Experimental Mechanics, Connecticut, USA, Jan 2005*,* pp. 1-10.

[93] Penrose, R., "A Generalised Inverse for Matrices", *Mathematical Proceedings of the Cambridge Philosophical Society,* Vol. 51, No. 03, 1955, pp. 406-413.

doi: 10.1017/S0305004100030401

[94] "MSC Nastran Users Manual", MSC Software Corporation, California, 2001.

[95] Chung, Y. T., and Sernaker, M. L., "Assessment of Target Mode Selection Criteria for Payload Modal Survey", Proceedings of *12th International Modal Analysis Conference*, Society for Experimental Mechanics, Connecticut, USA, Jan. 1994*,* pp. 272-279.

[96] Kammer, D. C., "Effect of Noise on Sensor Placement for on-Orbit Modal Identification of Large Space Structures", *Journal of Dynamic Systems Measurement and Control-Transactions of the ASME,* Vol. 114, No. 3, 1992, pp. 436-443.

doi: 10.1115/1.2897366

[97] Friswell, M. I., and Mottershead, J. E., "Finite Element Modelling", *Finite Element Model Updating in Structural Dynamics*, edited by G. M. L. Gladwell, Vol. 38, Kluwer Academic Publishers, Dordrecht, The Netherlands, 1995, pp. 7-35.

[98] "Matlab", R2011a ed, MathWorks, Inc., Natick, Massachusetts, 2011.

[99] Allemang, R. J., "The Modal Assurance Criterion - Twenty Years of Use and Abuse", *Sound and Vibration,* Vol. 37, No. 8, 2003, pp. 14-23.

[100] Kammer, D. C., and Nimityongskul, S., "Energy Based Comparison of Test and Analysis Response in the Frequency Domain", *Journal of Vibration and Acoustics-Transactions of the ASME,* Vol. 131, No. 6, 2009.

doi: 10.1115/1.4000424

[101] Chen, H. P., "Mode Shape Expansion Using Perturbed Force Approach", *Journal of Sound and Vibration,* Vol. 329, No. 8, 2010, pp. 1177-1190.

doi: 10.1016/j.jsv.2009.10.027

[102] Sairajan, K. K., and Aglietti, G. S., "Validity of Model Correlation Methods in FEM Validation for Forced Vibration Analysis", Proceedings of *12th European Conference on Spacecraft Structures, Materials and Environmental Testing*, ESA Communications, ESA-SP-691, Noordwijk, The Netherlands, Jul. 2012, pp. 1-6.

[103] Sairajan, K. K., and Aglietti, G. S., "Robustness of System Equivalent Reduction Expansion Process on Spacecraft Structure Model Validation", *AIAA Journal,* Vol. 50, No. 11, 2012, pp. 2376-2388.

doi: 10.2514/1.J051476

[104] Craig, R. R., "Structural Dynamics : An Introduction to Computer Methods", John Wiley, New York, 1981.

[105] Young, J. T., "Primer on the Craig-Bampton Method", URL: http://femci.gsfc.nasa.gov/craig_bampton/Primer_on_the_Craig-Bampton_Method.pdf, [cited 23/09/2011].

[106] Sairajan, K. K., and Aglietti, G. S., "Standard FEM Validation Checks and Quality of Response Prediction", *63rd International Astronautical Congress*, Naples, Italy, International Astronautical Federation, IAC-12-C2.1.6, Oct. 2012.

[107] Moreira, R. A. S., and Rodrigues, J. D., "Multilayer Damping Treatments: Modeling and Experimental Assessment", *Journal of Sandwich Structures and Materials,* Vol. 12, No. 2, 2010, pp. 181-198.

doi: 10.1177/1099636209104530

[108] Mead, D. J., "Passive Vibration Control", John Wiley & Sons Ltd, West Sussex, England, 2000.

[109] Sun, C. T., Sankar, B. V., and Rao, V. S., "Damping and Vibration Control of Unidirectional Composite Laminates Using Add-on Viscoelastic Materials", *Journal of Sound and Vibration,* Vol. 139, No. 2, 1990, pp. 277-287.

doi: 10.1016/0022-460x(90)90888-7

[110] Bangarubabu, P., Kishore Kumar, K., and Krishna, Y., "Damping Effect of Viscoelastic Materials on Sandwich Beams", *International Conference on Trends in Industrial and Mechanical Engineering*, Planetary Scientific Research Centre, Dubai, Mar. 2012.

[111] "3M™ Ultra-Pure Viscoelastic Damping Polymer", Electronics Markets Materials Division, 3M Center, ,St. Paul, Minnesota, Mar., 2012. URL: http://solutions.3m.com/wps/portal/3M/en_US/AdhesivesForElectronics/Home/Products/CushioningSolutions/ViscoelasticDampingPolymer/, [cited 12-02-2013].

[112] Hugon, J., Laduree, G., Maheri, M. R., and Adams, R. D., "Finite Element Prediction of Vibration Damping in Honeycomb Sandwich Panels", Proceedings of *The European Conference on Spacecraft Structures, Materials and Mechanical Testing*, ESA Communications, ESA SP-581, Noordwijk, The Netherlands, Aug. 2005, pp. 1-10.

[113] Sairajan, K. K., and Aglietti, G. S., "Study of the Correlation Criteria for Base Excitation of Spacecraft Structures", Journal of Spacecraft and Rockets. URL: http://arc.aiaa.org/doi/pdf/10.2514/1.A32457

doi: 10.2514/1.A32457

[114] Caruso, G., "A Critical Analysis of Electric Shunt Circuits Employed in Piezoelectric Passive Vibration Damping", *Smart Materials and Structures,* Vol. 10, No. 5, 2001, pp. 1059-1068.

doi: 10.1088/0964-1726/10/5/322

[115] Tzou, H. S., and Ye, R., "Piezothermoelasticity and Precision Control of Piezoelectric Systems - Theory and Finite-Element Analysis", *Journal of Vibration and Acoustics-Transactions of the ASME,* Vol. 116, No. 4, 1994, pp. 489-495.

doi: 10.1115/1.2930454

[116] Wang, J. S., and Ostergaard, D. F., "A Finite Element-Electric Circuit Coupled Simulation Method for Piezoelectric Transducer", Proceedings of *IEEE Ultrasonics Symposium*, IEEE, Washington, Oct. 1999, pp. 1105-1108.

[117] Reaves, M. C., and Horta, L. G., "Piezoelectric Actuator Modeling Using Msc/Nastran and Matlab", NASA/TM-2003-212651, Langley Research Center, Oct. 2003.

[118] Al-Hazmi, M. W., "Finite Element Analysis of Cantilever Plate Structure Excited by Patches of Piezoelectric Actuaturs", Proceedings of *11th IEEE Intersociety Conference on Thermal and Thermomechanical Phenomena in Electronic Systems,* Vol. 1-3, IEEE, Washington, May 2008, pp. 809-814.

[119] Seba, B., Ni, J., and Lohmann, B., "Vibration Attenuation Using a Piezoelectric Shunt Circuit Based on Finite Element Method Analysis", *Smart Materials and Structures,* Vol. 15, No. 2, 2006, pp. 509-517.

doi: 10.1088/0964-1726/15/2/034

[120] "Ansys Multiphysics", 14.0 ed, ANSYS, Inc., Canonsburg, Pennsylvania, 2011.

[121] McCalla, W. J., "Fundamentals of Computer-Aided Circuit Simulation", Kluwer Academic Pubishers, Boston, 1988.

[122] "Ansys 14.0 Help", ANSYS, Inc., Canonsburg, Pennsylvania 2011.

[123] "Coupled-Field Analysis Guide", ANSYS, Inc., Canonsburg, Pennsylvania 2009.

[124] Sairajan, K. K., Aglietti, G. S., and Walker, S. J. I., "Correlation of Finite Element Model of a Piezoelectric System", Proceedings of *International Conference on Advances in Engineering and Technology,* Vol. 3, Kanthimathi Publications, Chennai, India, Apr. 2013, pp. 22-25.